Institute of Thermoelectricity, Academy of Sciences and Ministry of Education and Science of Ukraine

Journal of THERMOELECTRICITY

International Research

Founded in December, 1993

published 4 times a year

No. 1 *2023*

Editorial Board

International Editorial Board

Founders – National Academy of Sciences, Ukraine
Institute of Thermoelectricity of National Academy of Sciences and Ministry of Education and Science of Ukraine

Certificate of state registration № КВ 15496-4068 ПР

Address of editorial office:
Ukraine, 58002, Chernivtsi, General Post Office, P.O. Box 86.
Phone: +(380-372) 90 31 65.
Fax: +(380-3722) 4 19 17.
E-mail: jt@inst.cv.ua
http://www.jt.inst.cv.ua

Signed for publication 25.03.2023. Format 70×108/16. Offset paper №1. Offset printing.
Printer's sheet 11.5. Publisher's signature 9.2. Circulation 400 copies. Order 5.

Printed from the layout original made by "Journal of Thermoelectricity" editorial board
in the printing house of "Bukrek" publishers,
10, Radischev Str., Chernivtsi, 58000, Ukraine

CONTENTS

Theory

P.V. Gorskyi Theoretical models of lattice thermal conductivity of single-crystal bismuth telluride 5

V.G. Deibuk Phase stability of thermoelectric *ZnSb-SnTe* thin films 14

Materials research

O. M. Manyk, T. O. Manyk, V.R. Bilynskyi-Slotylo Theoretical models of ordered alloys of ternary systems of thermoelectric materials. 3 Chemical bond and state diagrams of *Cd-Zn-Sb* 24

V. A. Romaka, Yu. V. Stadnyk, L. P. Romaka, P. Yu. Demchenko, A. M. Horyn, T. I. Lukovskyi Experimental investigations of the properties of a new thermoelectric material $Tm_{1-x}V_xNiSb$ 33

M. M. Korop Machine learning in thermoelectric materials science 44

Design

L. I. Anatychuk, R. R. Kobylianskyi, V. V. Lysko Computer design of a thermoelectric pulmonary air condenser for the diagnostics of coronavirus and other diseases 55

D. E. Rybchakov Computer method of description of technologies and properties of thermoelectric Bi_2-Te_3 based material by extrusion method 66

I.A. Konstantynovych, R.V. Kuz, O.M. Makhanets, R.G. Cherkez Sectional generator thermoelements in a magnetic field 75

Thermoelectric products

L. I., Anatychuk V. G., Rifert, P. O., Barabash, R. V., Desiateryk, A. S., Solomakha, Yu. Yu., Rozver, V. G., Petrenko Performance testing of a thermoelectric heat pump for centrifugal distillation of wastewater of a space life support system 82

L. I. Anatychuk, V. V. Lysko On the design of a trench thermoelectric source of heat and electricity 93

P. V. Gorskiy

P. V. Gorskyi *dok. phys.– mat. sciences*[1,2]

[1]Institute of Thermoelectricity of the NAS
and MES of Ukraine,
1, Nauky str., Chernivtsi, 58029, Ukraine,
e-mail: gena.grim@gmail.com
e-mail: anatych@gmail.com
[2]Yu.Fedkovych Chernivtsi National University,
2, Kotsiubynskyi str., Chernivtsi, 58012, Ukraine

THEORETICAL MODELS OF LATTICE THERMAL CONDUCTIVITY OF SINGLE-CRYSTAL BISMUTH TELLURIDE

In the isotropic approximation, the effect of the real density of phonon states on the lattice thermal conductivity of single-crystal bismuth telluride is taken into account within the framework of two model approaches. First, the problem is considered in the isotropic approximation, and then the layered structure and anisotropy are roughly taken into account. It is shown that the real density of phonon states almost does not change the temperature dependence of the lattice thermal conductivity of bismuth telluride both in the plane of the layers (cleavage) and perpendicular to it compared to the Debye density of phonon states. This weakness is explained by the fact that the change in the differential heat capacity contribution to thermal conductivity caused directly by the density of phonon states is compensated by the effect of this density on scattering, which is caused by the nonlinear dependence of the wave vector on the frequency, the difference between the group velocity of sound and the phase velocity, and a significant increase in the Umklapp coefficient. The obtained results are not only in qualitative, but also in satisfactory quantitative agreement with the theoretical studies of previous authors and the experiment. This allows us to hope that the real density of phonon states will not have a significant effect on the thermomechanical deformations of thermoelectric legs in comparison with the Debye density of phonon states. Bibl. 7, Fig. 2.

Key words: cyclic stability of thermoelements, reliability of thermoelectric legs, thermomechanical stresses, thermal conductivity, real and Debye densities of phonon states, normal processes, Umklapp processes.

Introduction

The efforts of material scientists today are mainly aimed at increasing the thermoelectric figure of merit and efficiency of thermoelectric materials. At the same time, one of the main ways of such an increase is considered to be a decrease in thermal conductivity, in particular its lattice component. But such a way is in a certain contradiction with the considerations of mechanical reliability of thermoelectric materials. This contradiction can be explained on the basis of the physical model depicted in Fig. 1.

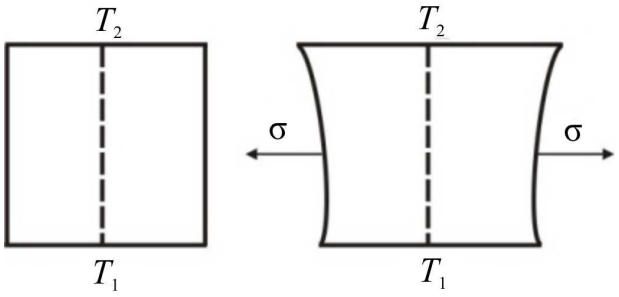

а) $T_1 = T_2$ *б) $T_1 < T_2$*

Fig.1. Physical model of temperature deformation of thermoelectric leg

If there is no temperature gradient, then thermomechanical stresses do not occur. But in the presence of a temperature gradient, stresses do not arise only when a thermoelectric leg expands freely. But in reality, it is attached by the end faces to the anti-diffusion layer, interconnect and ceramic plates. If the fastening is absolutely rigid, then in accordance with Hooke's generalized law [1], there is a bending stress equal to:

$$\sigma = \frac{E\alpha_T \Delta T}{1-\nu} \ , \tag{1}$$

where E, α_T, ν are Young's modulus, coefficient of linear expansion and Poisson's ratio of thermoelectric material, respectively, ΔT is temperature difference on the leg. This bending stress should not exceed the cracking strength of the crystal σ_f [2]. On the other hand, for the same heat flow, the temperature difference is the smaller, the higher the thermal conductivity κ. Therefore, the so-called thermal shock resistance criterion [2] is introduced, which is equal to:

$$R = \frac{E\alpha_T}{(1-\nu)\kappa\sigma_f} \ . \tag{2}$$

It is believed that it should be as small as possible. On the other hand, high figure of merit of a thermoelectric material implies a low value of κ, that is, a high value of R. This explains the contradiction mentioned at the beginning of the article, which determines the relevance and the very setting of this study, because the task of finding ways to achieve a safe "compromise" value of κ arises. From this follows the object and subject of research.

The object of research is single-crystal bismuth telluride. The subject of research is the influence of the real density of phonon states and the anisotropy of the phonon spectrum on its lattice thermal conductivity.

Results of research and their discussion

In this work, research was carried out for single-crystal bismuth telluride, and when calculating the lattice thermal conductivity, the influence of normal scattering and scattering with mutual phonon Umklapp was taken into account. The latter is important because it is what provides the finite value of thermal conductivity. In the case of purely normal scattering, the total energy and total quasi-momentum of each triplet of phonons, and, consequently, the momentum of the phonon subsystem of the crystal as a whole are preserved. Thus, a kind of "super thermal conductivity" takes place, which is to some extent analogous to superconductivity, and hence the lattice thermal

conductivity will be infinite if there are no other phonon scattering mechanisms. In the presence of Umklapp processes, the energy is preserved, and the quasi-momentum is preserved, as is customary to say, with the accuracy of the inverted lattice vector. But the very concept of an inverted lattice has meaning only when taking into account the atomic structure of matter. In a "truly" continuous medium, the phonon thermal conductivity should be infinite if there are no other phonon scattering mechanisms.

The article [3] gives general formulae for the thermal conductivity of a crystal lattice in the case when the law of dispersion of acoustic phonons is linear, and the isofrequency surface of phonons is a sphere, and therefore the density of phonon states is described by the Debye model, that is, it is a quadratic function of frequency. At the same time, they were derived for a simple cubic lattice with one atom in the unit cell. We need to modify these formulae for the case of an arbitrary structure of the crystal lattice, an arbitrary energy spectrum of phonons, and, therefore, an arbitrary frequency dependence of the density of phonon states. At the same time, having information not about the phonon spectrum as a whole, but only about the frequency dependence of the density of phonon states, we can do this in the isotropic approximation. This approximation, despite the anisotropy of the bismuth telluride crystal, is quite often used in calculating its thermoelectric characteristics. We are forced to do this also because the correspondence between the phonon spectrum of a crystal and the corresponding density of phonon states is not one-to-one. This means that, knowing the phonon spectrum of a crystal, you can always find the corresponding density of phonon states. But in the general case it is impossible to unambiguously perform the reverse operation. But it can be implemented in the isotropic case, when the is of requency surface is a sphere.

So, we will start the modification of the corresponding formulay by restoring the energy spectrum according to its density of states. In the isotropic case, the following formula for the radius of the isofrequency surface corresponding to the frequency ω follows from the requirement of conservation of the number of phonon states:

$$k_0(\omega) = \sqrt[3]{\frac{3}{4\pi}\int_0^x g_{ph}(\omega)\,d\omega}\,. \tag{3}$$

In the so-called normalized form, this ratio can be presented as follows:

$$K(x) = \sqrt[3]{3\int_0^x f(y)\,dy}\,, \tag{4}$$

where x – is the phonon frequency normalized to their maximum frequency, $f(x)$ – is the density of phonon states normalized to their maximum value according to the Debye model, $K(x)$ – is the phonon quasimomentum normalized to its value corresponding to the maximum phonon frequency according to the Debye model. In addition, let us take into account that both in the general formula for lattice thermal conductivity and in the formulae given in the article [3] for the probabilities of normal scattering of phonons and their scattering with Umklapp, not only the frequency and wave vector of phonons appear, but also the velocity of sound in the crystal, which, is obviously the group velocity. On the other hand, it is not the group but the phase velocity of sound that is directly related to the

elastic constants of the crystal. Therefore, we still need the group velocity of sound normalized to the phase velocity of sound in the Debye model for the real phonon spectrum. From relation (2), it is not difficult to obtain the following expression for the normalized group velocity of sound:

$$v_g(x) = \frac{f(x)}{K^2(x)}. \tag{5}$$

Taking into account the above and modifying accordingly the formulae known from [3] for the probabilities of normal scattering of phonons and their Umklapp scattering, we obtain the following formula for the thermal conductivity of a single crystal with a real phonon spectrum in the isotropic approximation:

$$\kappa_l = \frac{3h^2\rho s^4\omega_{\max}}{16\gamma^2k^2T^3}\int_0^1 \frac{f^2(x)x^2\exp(x/\theta)}{K^2(x)\left[\exp(x/\theta)-1\right]^2}\left(\frac{1}{Q_l(x)}+\frac{2}{Q_t(x)}\right)dx, \tag{6}$$

where ρ, s, ω_{max}, γ, T the crystal density, the phase velocity of sound, the maximum phonon frequency, the Gruneisen parameter and the temperature $\theta = T/T_D$, T_D – the Debye temperature, the rest of notations are explained above, or they are generally accepted. Moreover:

$$Q_l(x) = f(x)K^2(x) + \mu\frac{x^2}{K(x)}, \tag{7}$$

$$Q_t(x) = 3.125\theta^3\frac{f^4(x)}{K^7(x)} + \mu\frac{x^2}{K(x)}, \tag{8}$$

μ – the Umklapp coefficient, which is selected so that the theory coincides with experiment, since its theoretical estimate, made only for a simple cubic lattice with one atom in the unit cell, is not even suitable for all substances with such a lattice. This coefficient was also selected by the authors of work [4]. In this case, expressions (5) and (6) describe mutual scattering of longitudinal and transverse phonons, inherent in a single-crystal material, due to the anharmonicity of thermal vibrations of the lattice, and the terms in them that do not contain the Umklapp coefficient describe normal processes. They influence the overall thermal conductivity due to the renormalization of the time between phonon collisions.

In the Debye model, formula (4) will acquire the form:

$$\kappa_l = \frac{3h^2\rho s^4\omega_{\max}}{16\gamma^2k^2T^3}\int_0^1 \frac{x^4\exp(x/\theta)}{\left[\exp(x/\theta)-1\right]^2}\left(\frac{1}{x^4+\mu x}+\frac{2}{(3.125\theta^3+\mu)x}\right)dx. \tag{9}$$

The real [5] and Debye densities of phonon states for bismuth telluride and the corresponding dependence of the wave vector on the frequency in accordance with (2) are shown in Fig. 1.

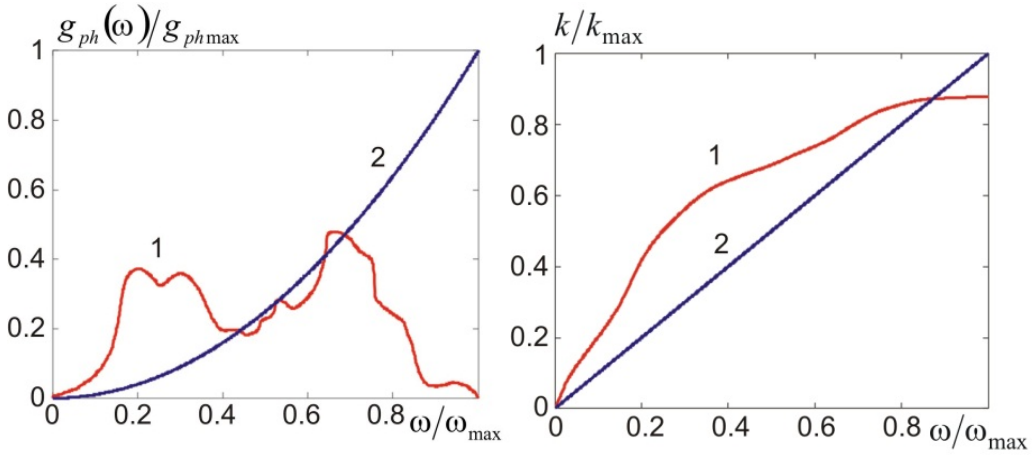

a) *b)*

Fig.1. a) real (curve 1) and Debye (curve 2) densities of phonon states in bismuth telluride; b) the corresponding dependences of the wave vector on frequency

But there is another question, which phase velocity of sound should appear in formulae (4) and (7). The answer to this question is as follows. Since the Debye temperature is experimentally determined on the basis of calorimetric measurements and is a scalar, the velocity that makes sense to be called calorimetric should appear as the phase velocity of sound. It does not necessarily have to be related by any one-to-one relationship to crystal elastic constants, but must be unambiguously related to the number of phonon states in the Debye model. Let's establish this relationship for bismuth telluride.

If the calorimetric Debye temperature is equal to T_D, then $\omega_{max} = 2\pi k T_D / h$, and, hence, the radius of the Debye sphere is equal to

$$k_D = \frac{2\pi k T_D}{hs}. \tag{10}$$

Then the volume of this sphere should be equal to the number of phonon states per unit volume of the crystal. And this number is the number of degrees of freedom per unit volume of the crystal. Given the fact that the bismuth telluride molecule consists of five atoms, it has 6 degrees of freedom. Thus, we obtain the following relation for determination of s:

$$\frac{4}{3}\left(\frac{2\pi k T_D}{hs}\right)^3 = \frac{6 N_A \rho}{M}, \tag{11}$$

where M is a molecular mass of bismuth telluride, other notations are explained above or they are generally accepted. Therefore,

$$s = \frac{2\pi k T_D}{h}\sqrt[3]{\frac{M}{4.5 N_A \rho}}. \tag{12}$$

The temperature dependences of the lattice thermal conductivity of bismuth telluride corresponding to the two considered models in cleavage planes and perpendicular to them are shown in Fig. 2.

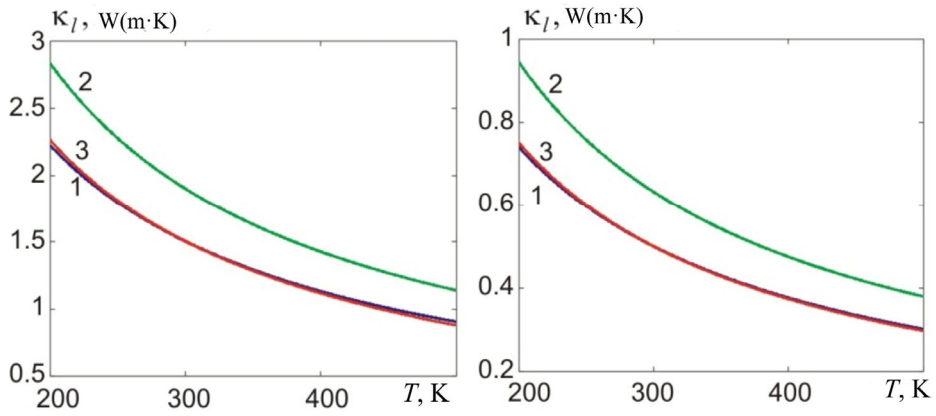

a) *b)*

Fig. 2. Temperature dependences of lattice thermal conductivity in the isotropic approximation: a) in cleavage planes, b) perpendicular to them: 1 – in the Debye model; 2 – for the real phonon spectrum, with regard to its influence only on the heat capacity differential contribution to thermal conductivity; 3 – for the real phonon spectrum, with regard to its influence both on the heat capacity differential contribution and on mutual phonon scattering due to the anharmonicity of lattice thermal vibrations

It can be seen from the figure that for both models of the density of phonon states, one of which, namely, shown by curve 1 in Fig. 1, was determined experimentally, the thermal conductivities both in the cleavage planes and perpendicular to them in the entire investigated temperature interval are weakly different from each other, although in the Debye model, at low temperatures, both components of the thermal conductivity tensor are somewhat smaller, and at high temperatures, they are somewhat larger than for the real phonon spectrum. But these differences are so insignificant that they cannot have a significant impact on thermomechanical stresses in thermoelectric legs. At first glance, such minor differences may seem incomprehensible. But it should be borne in mind that the difference in the differential heat capacity contributions to the thermal conductivity for the specified models is compensated by the difference in the manifestations of mutual phonon scattering, which is caused by: 1) the nonlinear relationship between the frequency and the wave vector for the real model of the density of phonon states; 2) the difference between the group sound velocity and the phase velocity for a real model of the density of phonon states; 3) the difference in Umklapp coefficients in the real and Debye models of the density of phonon states. This can be seen from the comparison of curves 1 and 3 with curve 2 in each of the figures. On the other hand, if the real density of phonon states affected only the heat capacity differential contribution to the thermal conductivity, then the thermal conductivity would be approximately 1.27 - 1.5 times higher than in the Debye model. And this would allow us to hope for a certain reduction of thermomechanical stresses in thermoelectric legs, albeit at the expense of some loss of thermoelectric figure of merit and the efficiency of material.

Note that when constructing the graphs, we used the following values of Bi_2Te_3 parameters: $\rho = 7850$ kg/m^3, $M = 801$, $T_D = 155$ K, $\gamma = 1.4$. The anisotropy of thermal conductivity at 300 K was assumed equal to [6] and for both models of the density of phonon states it was taken into account solely due to the anisotropy of Umklapp coefficient.

Regarding a more complete comparison of the results of our calculations with experiment, we note that the calculated value of the thermal conductivity of bismuth telluride at 200 K that we obtained differs from the experimental value, which, in accordance with the data of [6, 7] is 2.1 W/(m K), by approximately 5.7 % upward, which can be considered satisfactory. However, on this

occasion it is appropriate to make the following remark. There is no direct experimental technique for separating the lattice part of thermal conductivity from the thermal conductivity caused by free charge carriers. Therefore, this separation is performed purely by calculation on the basis of certain assumptions about the band spectrum of the material and the mechanisms of scattering of free charge carriers in it. We did not analyze the reliability of this kind of assumptions made in paper [7].

Conclusions

1. In the isotropic approximation, it is shown that the real density of phonon states, compared to the Debye density, has a weak effect on the lattice thermal conductivity of single-crystal bismuth telluride in the temperature range between 200 and 500 K both in the cleavage planes and perpendicular to them. Small differences between the Debye and real densities of phonon states from the point of view of their influence on thermal conductivity can be explained by the fact that the differences in the differential heat capacity contributions to thermal conductivity due to the considered densities of phonon states are compensated by differences in the group sound velocities and the characteristics of mutual phonon scattering, both normal and Umklapp.
2. The Umklapp parameter is anisotropic and depends on the form of the density of phonon states, but does not depend on temperature.
3. When calculating thermal conductivity, the phase velocity of sound, which is determined by the Debye temperature and the number of degrees of freedom of the phonon subsystem, should be taken into account.
4. Differences in the densities of phonon states between the real and Debye models cannot lead to significant differences in the expected values of thermomechanical stresses in thermoelectric legs.
5. The results of calculations are not only in qualitative, but also in satisfactory quantitative agreement with experimental data.

References

1. Pysarenko H.S. (2004). *Opir materialiv [Resistance of materials].* Kyiv; Vyshcha shkola. [in Ukrainian].
2. Kim H.S. (2016). Engineering thermal conductivity for balancing between reliability and performance of bulk thermoelectric generators. *Advanced Functional Materials*, 26, 3678 – 3686.
3. Klemens P.D. (1958). *Thermal conductivity and lattice vibrational modes. In: Solid state physics. Vol.7*. New York: Academic Press Inc., Publishers.
4. Da Silva L.W. (2004). Micro-thermoelectric cooler: interfacial effects on thermal and electrical transport. *International Journal of Heat and Mass Transfer.* 47, .2417 – 2435. doi:10.1016/j.ijheatmasstransfer.2003.11.024
5. Rauh H., Geick R., Kohler H. et al (1981). Generalized phonon density of states of the layer compounds Bi_2Se_3, Bi_2Te_3, Sb_2Te_3 and $Bi_2(Te_{0.5}Se_{0.5})_3$, $(Bi_{0.5}Sb_{0.5})_2Te_3$. *Sol. St. Phys*., 14., 2705 – 2712.
6. Anatychuk L.I. (2003). *Termoelektrichestvo. T. 2. Termoelektricheskiie preobrazovatelu energii [Thermoelectricity. Vol. 2. Thermoelectric energy converters].* Kyiv, Chernivtsi: Naukova Dumka.

7. Goldsmid H. J. (1958). Heat conduction of bismuth telluride. *Proc. Phys. Soc. (London),* .72, .17 - 26. http://iopscience.iop.org/0370-1328/72/1/304.

Submitted: 04.01.2023

Горський П. В., *док. фіз.-мат. наук*[1,2]

[1]Інститут термоелектрики НАН та МОН України,
вул. Науки, 1, Чернівці, 58029, Україна;
[2]Чернівецький національний університет імені Юрія Федьковича,
вул. Коцюбинського 2, Чернівці, 58012, Україна
e-mail: gena.grim@gmail.com

ТЕОРЕТИЧНІ МОДЕЛІ ГРАТКОВОЇ ТЕПЛОПРОВІДНОСТІ МОНОКРИСТАЛІЧНОГО ТЕЛУРИДУ ВІСМУТУ

В ізотропному наближенні враховано вплив реальної густини фононних станів на граткову теплопровідність монокристалічного телуриду вісмуту у рамках двох модельних підходів. Спочатку задачу розглянуто у ізотропному наближенні, а потім наближено враховано шарувату структуру та анізотропію. Показано, що реальна густина фононних станів майже не змінює температурної залежності граткової теплопровідності телуриду вісмуту як в площині шарів(спайності) так і перпендикулярно до неї порівняно з Дебаївською густиною фононних станів. Ця слабкість пояснюється тим, що зумовлена безпосередньо щільністю фононних станів зміна диференціального теплоємнісного внеску у теплопровідність компенсується впливом цієї щільності на розсіювання, який зумовлений нелінійною залежністю хвильового вектора від частоти, відмінністю групової швидкості звуку від фазової та істотним зростанням коефіцієнта перекидання. Отримані результати перебувають не лише у якісній, а й у задовільній кількісній згоді з теоретичними дослідженнями попередніх авторів та експериментом. Це дозволяє сподіватись, що реальна густина фононних станів не справлятиме істотного впливу на термомеханічні деформації термоелектричних гілок у порівнянні з Дебаївською густиною фононних станів. Бібл. 7, Мал. 2.

Ключові слова: *циклічна стійкість термоелементів, надійність термоелектричних гілок, термомеханічні напруги, теплопровідність, реальна і Дебаївська щільності фононних станів, нормальні процеси, процеси перекидання.*

References

1. Pysarenko H.S. (2004). *Opir materialiv [Resistance of materials].* Kyiv; Vyshcha shkola. [in Ukrainian].
2. Kim H.S. (2016). Engineering thermal conductivity for balancing between reliability and performance of bulk thermoelectric generators. *Advanced Functional Materials*, 26, 3678 – 3686.
3. Klemens P.D. (1958). *Thermal conductivity and lattice vibrational modes. In: Solid state physics. Vol.7*. New York: Academic Press Inc., Publishers.

4. Da Silva L.W. (2004). Micro-thermoelectric cooler: interfacial effects on thermal and electrical transport. *International Journal of Heat and Mass Transfer.* 47, .2417 – 2435. doi:10.1016/j.ijheatmasstransfer.2003.11.024
5. Rauh H., Geick R., Kohler H. et al (1981). Generalized phonon density of states of the layer compounds Bi_2Se_3, Bi_2Te_3, Sb_2Te_3 and $Bi_2(Te_{0.5}Se_{0.5})_3$, $(Bi_{0.5}Sb_{0.5})_2Te_3$. *Sol. St. Phys*., 14., 2705 – 2712.
6. Anatychuk L.I. (2003). *Termoelektrichestvo. T. 2. Termoelektricheskiie preobrazovatelu energii [Thermoelectricity. Vol. 2. Thermoelectric energy converters].* Kyiv, Chernivtsi: Naukova Dumka.
7. Goldsmid H. J. (1958). Heat conduction of bismuth telluride. *Proc. Phys. Soc. (London),* .72, .17 – 26. http://iopscience.iop.org/0370-1328/72/1/304.

Submitted: 04.01.2023

V. G. Deibuk

V. G. Deibuk, *doc. phys – math sciences, professor* [1,2]

[1]Institute of Thermoelectricity of the NAS and MES Ukraine,
Nauky str., Chernivtsi, 58029, Ukraine
[2]Yu.Fedkovich Chernivtsi National University,
Kotsyubynsky str., Chernivtsi, 58012, Ukraine
e-male: v.deibuk@chnu.edu.ua

PHASE STABILITY OF THERMOELECTRIC *ZnSb-SnTe* THIN FILMS

The article theoretically studies the phase stability of thin films of pseudobinary semiconductor alloys ZnSb–SnTe. The obtained T – x phase diagrams made it possible to predict the existence of a wide miscibility gap. Taking into account small internal stresses and the influence of the quartz substrate did not lead to significant changes in the phase diagram depending on the film thickness. It has been shown that spinodal decomposition processes caused by annealing at T = 225 °C in $(ZnSb)_{1-x}(SnTe)_x$ alloys at x = 0.27 lead to microstructural evolution with the formation of precipitates of the SnSb metal phase. This fact is in good agreement with the experimental studies of the thin films considered and is the reason for the sharp increase in the power factor to 3383 $\mu Wm^{-1}K^{-1}$ at 300 °C. The described recrystallization processes are the main mechanism for the high thermoelectric characteristics of this material. Bibl. 20, Fig. 3.
Key words: thin films, thermoelectric materials, spinodal decomposition, phase stability.

Introduction

Recently, green methods of directly converting thermal energy into electrical energy have attracted increasing interest [1, 2, 19]. These include thermoelectric conversion based on the well-known Seebeck effect. This method is characterized by the absence of harmful emissions, compactness and high reliability of devices, as well as a wide range of operating temperatures [1, 2]. Well-known bulk semiconductor thermoelectric materials, such as *Bi-Te-Sb*, *SnSe-SnTe*, *PbTe*, *Si-Ge*, *Ge-Te*, *ZnSb-CdSb* [1, 3] et al., along with high efficiency, also have a number of significant disadvantages associated with thermodynamic instability at temperatures above 600°C, which leads to limited practical use. At the same time, thin-film thermoelectric materials [4 – 6] are relatively easily synthesized on various substrates, have low cost and weight, which allows them to be widely used for high-quality miniature devices. Thermoelectric converters will be especially effective for powering Internet of Things devices, recycling thermal emissions from cars, thermal power plants, and so on.

Semiconductor alloy systems form a class of promising thermoelectric materials with high figures of merit [1]

$$ZT = S^2 \frac{\sigma T}{k}, \qquad (1)$$

where T is the absolute temperature, and three transport parameters (S, σ, k) are strongly interdependent, making the design of high ZT materials a challenging task.

Over the past ten years, the progress in achieving the maximum *ZT* value in semiconductor materials in various temperature regions is quite significant and is due to a large extent to greater attention to thin-film microelectronic devices. In particular, in the low-temperature region (that is, up to 500 K), which is especially relevant for flexible integrated electronics and various computer devices [6, 20].

It has recently been shown [7] that alloying *ZnSb* with *SnTe* can increase the figure of merit through the formation of *SnSb* nanoscale precipitates, which increase the power factor ($PF = S^2\sigma$) at 300 °C more than 7.7 times. A clear insulator-metal phase transition (IMT) was experimentally demonstrated at SnTe composition $x = 0.27$ by thermal fluctuations and microstructure evolution of $(ZnSb)_{1-x}(SnTe)_x$ thin films.

This study aimed to investigate the thermodynamics of mixing such a system. In addition, it is also necessary to evaluate the influence of the strain effects in the films due to the mismatch between the lattices of the alloy and the substrate on the miscibility gap.

Miscibility analysis for *ZnSb-SnTe* pseudo-binary system

For the thermodynamic description of pseudo-binary solid solutions we will consider the Gibbs free energy of mixing (ΔG) [8]:

$$\Delta G = \Delta H - T\Delta S\ , \tag{2}$$

where ΔH is enthalpy of mixing, T is absolute temperature, ΔS is entropy of mixing which in the approximation of a regular solid solution can be written [18]:

$$\Delta S = -R\{x\ln x + (1-x)\ln(1-x)\}. \tag{3}$$

To describe the enthalpy of mixing, two models are most commonly used – the regular solution model and the "delta lattice parameter" (DLP) model [9]. It is known that the regular solution model describes well the thermodynamic properties of a liquid phase and has restrictions for the case of a solid phase, since interaction parameters in the regular solution model depend on the alloy composition (x).

In the DLP model, the enthalpy of mixing ΔH depends only on a lattice parameter (a), so it is assumed that the difference between the dimensions of atoms having common sublattice is a decisive factor that controls the free energy of mixing. Well-developed first-principle methods are much more complicated and surprisingly do not give fundamentally better results [9]. The DLP model is a semi-empirical model for calculating the phase diagrams of semiconductors that has been tested in many semiconductor systems. It is based on the Phillips-Van Vechten model [8], which relates the band gap energies to the covalent bond length in each crystal to the -2.5th power. Similarly, Stringfellow [9] related the atomization energy, ΔH^{at}, to the lattice parameter for III-V, II-VI, IV, oxide, and other semiconductor alloys by adopting the relationship

$$\Delta H^{at} = K(a_0)^{-2.5}$$

for $(ZnSb)_{1-x}(SnTe)_x$ solid solutions ΔH can be written as [5, 8]:

$$\Delta H = E(alloy) - xE(BC) - (1-x)E(AC) = \Omega x(1-x)\ , \tag{4}$$

$$\Omega = K\frac{\Delta a^2}{a_{avg}^{4.5}}, \tag{5}$$

where K – is model parameter, a_{avg} – is averaged lattice parameter, Δa – is the difference between lattice parameters of components of solid solution compounds.

As long as the lattice parameters of the components of the *ZnSb-SnTe* solid solution under study are rather close [11 – 14], the solid solution can be considered almost perfect, and the interaction parameter Ω and enthalpy of mixing ΔH have positive values. That's why the solid solution will be subject to spinodal decomposition on the condition that the curve of the composition dependence of free energy has a bend point. The spinodal line itself is difficult to measure experimentally, and so it is often approximated by the chemical spinodal, which is given by the locus of points $\partial^2 G/\partial x^2 = 0$ [5, 8]. The products of spinodal decomposition are two solid solutions with different compositions. The stability criterion of pseudo-binary alloys can be written as $\partial^2 G/\partial x^2 > 0$. The instability area is determined as a geometrical place of points for which the condition $\partial^2 G/\partial x^2 = 0$ is met.

The temperature–composition phase diagram of *ZnSb-SnTe* (Fig. 1) contains a miscibility gap: a region where *ZnSb* and *SnTe* are not soluble in one another, and a *ZnSb*-rich phase may precipitate out of a *SnSb* nanoprecipitates during the crystallization process. The solid solution can be unstable or metastable within a miscibility gap concerning phase separation; the boundary between these two regions is called the spinodal line. Outside of the spinodal, the solid solution is metastable, and phase separation proceeds by a nucleation and growth mechanism.

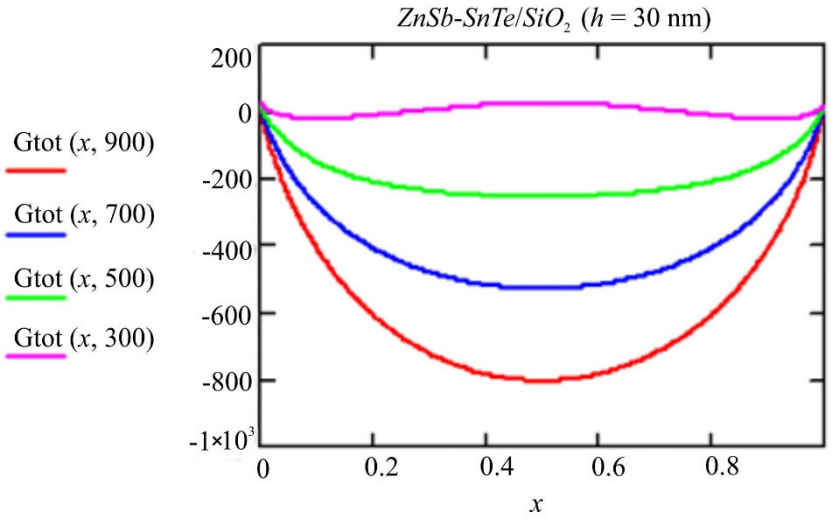

Fig. 1. Gibbs free energy of mixing ΔG of ZnSb-SnTe as a function of mole fraction x SnTe at T = 300, 500, 700, and 900K

The Gibbs free energy of formation of *ZnSb-SnTe* solid solutions differs significantly from the ideal form, changing the sign with a change in composition x. The existence of a positive region of $\Delta G(x)$ dependence can lead to the decomposition of the solid solution in a certain temperature range below critical T_c. For a bulk solid solution, in addition to the chemical part of the free energy, it is also necessary to take into account the elastic component, which follows from the requirement of coherent phase conjugation taking into account crystalline anisotropy [8, 9]. Inside the spinodal, the solid solution

is unstable, and phase separation occurs due to spinodal decomposition. A schematic representation of the miscibility gap is shown in Fig. 2. Calculated phase diagram ($T-x$) of *ZnSb-SnTe* alloy system containing MG (unstable solid solution).

The *SnSb* nanoprecipitates seen experimentally in *ZnSb-SnTe* are a consequence of the chemical thermodynamics of mixing in this system [7].

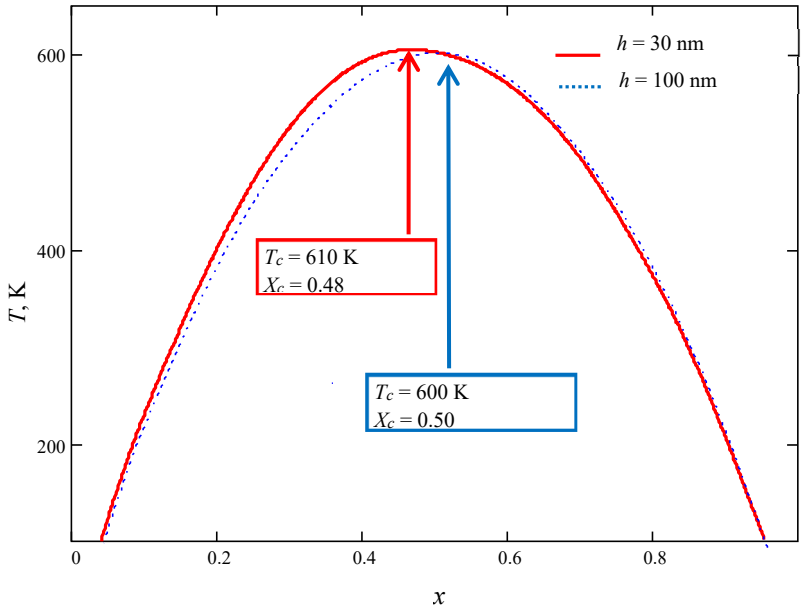

Fig.2. Calculated spinodal curves for ZnSb-SnTe/SiO_2 films with thicknesses of 30 nm (red curve) and 100 nm (blue dotted curve)

Elastic energy in the spinodal decomposition *ZnSb-SnTe/SiO_2* thin films

For a bulk solid solution, it is necessary to take into account the elastic component of the free energy in addition to the chemical component. When the alloy is in the form of a thin epitaxial film and the thermodynamic process involves the formation of misfit dislocations, biaxial tensile and compressive strains ε arise in the film as a result of a mismatch between the lattice constants of the alloy (a_{alloy}) and the substrate material (a_{sub}): $\varepsilon_{xx} = \varepsilon_{yy}$.

In the general case the energy of elastic strain of the unit volume of deformed film can be written as [10]:

$$E_s = \frac{1}{2}\left(\sigma_x\varepsilon_x + \sigma_y\varepsilon_y + \sigma_z\varepsilon_z + \tau_{xy}\gamma_{xy} + \tau_{yz}\gamma_{yz} + \tau_{xz}\gamma_{xz}\right), \tag{6}$$

where σ_x, σ_y, σ_z are normal stresses; τ_{xy}, τ_{yz}, τ_{xz} are shear stresses; ε_x, ε_y, ε_z are normal strains; γ_{xy}, γ_{yz}, γ_{xz} are shear strains. It is commonly assumed that with the epitaxial growth due to mismatch between lattice constants of substrate-film only normal strains and stresses occur along two perpendicular axes in the film plane (001).

Taking into account the relation between normal strains and stresses based on Hooke's law, we obtain:

$$\begin{aligned} \sigma_x &= c_{11}\varepsilon_x + c_{12}\varepsilon_y + c_{13}\varepsilon_z \\ \sigma_y &= c_{12}\varepsilon_x + c_{22}\varepsilon_y + c_{23}\varepsilon_z \end{aligned}, \tag{7}$$

where in the case of equal symmetry of film and substrate material, the relative strain components

$$\varepsilon_x = \frac{a_{alloy} - a_{sub}}{a_{sub}}, \qquad \varepsilon_y = \frac{b_{alloy} - b_{sub}}{b_{sub}}. \tag{8}$$

For orthorhombic crystals the array of elastic moduli comprises 9 independent components [5, 12, 13]:

$$\begin{pmatrix} c_{11} & c_{12} & c_{13} & 0 & 0 & 0 \\ c_{12} & c_{22} & c_{23} & 0 & 0 & 0 \\ c_{13} & c_{23} & c_{33} & 0 & 0 & 0 \\ 0 & 0 & 0 & c_{44} & 0 & 0 \\ 0 & 0 & 0 & 0 & c_{55} & 0 \\ 0 & 0 & 0 & 0 & 0 & c_{66} \end{pmatrix}. \tag{9}$$

Stress tensor component in perpendicular (z) direction can be written:

$$\sigma_z = c_{13}\varepsilon_x + c_{23}\varepsilon_y + c_{33}\varepsilon_z. \tag{10}$$

Taking into account for free (growth) direction of the film that $\sigma_z = 0$, from (10) we obtain:

$$\varepsilon_z = -\frac{C_{13}}{C_{33}}\varepsilon_x - \frac{C_{23}}{C_{33}}\varepsilon_y. \tag{11}$$

Hence, the elastic strain energy of the unit volume of epitaxial film (6), with regard to (10) – (11) can be written as:

$$E_s = \frac{1}{2}\left(\sigma_x\varepsilon_x + \sigma_y\varepsilon_y\right) = \frac{1}{2}\left(\left(c_{11} - \frac{c_{13}^2}{c_{33}}\right)\varepsilon_x^2 + \left(c_{22} - \frac{c_{23}^2}{c_{33}}\right)\varepsilon_y^2 + 2\left(c_{12} - \frac{c_{13}c_{23}}{c_{33}}\right)\varepsilon_x\varepsilon_y\right). \tag{12}$$

Thus, full Gibbs free energy of the system based on the unit volume is a sum of chemical energy (ΔG) and elastic strain energy (E_s):

$$G = N_v\Delta G + E_s, \tag{13}$$

where N_v is the number of moles of the unit volume of homogeneous solid solution to decomposition. Analysis of the Gibbs free energy as a function of solid solution composition and epilayer thickness together with stability criterion allows calculating solubility limits. Parameters used for calculations were taken from [18]. The dependence of lattice constants on the composition x was taken into account by the Vegard rule which is met for $(ZnSb)_{1-x}(SnTe)_x$ semiconductor solid solutions [7].

The described situation is observed only in the case when the film thickness (h) is less than the critical thickness (h_c). Under the condition $h > h_c$, plastic relaxation processes occur in the film with the formation of misfit dislocations, and the thicker the film, the less its deformation [15 – 18]. To determine the influence of these effects on the thermodynamic stability of the selected solid solutions, we note that according to the model of the balance of forces acting on dislocations, we can write:

$$\varepsilon_z = A/h \ , \tag{14}$$

that is, as the thickness of the epitaxial film increases, the value of relative strain decreases and the film gradually relaxes. Parameter A will be found from the continuity condition of function $\varepsilon(h)$ at point $h = h_c$, then we obtain

$$A = \varepsilon_{z\,max} h_c \, . \tag{15}$$

The majority of semiconductor heteroepitaxies are grown on (001) substrate surface, so exactly this orientation will be considered. A theoretical expression for critical thickness h_c can be obtained based on two different approximations, known as equilibrium theories of critical thickness [15]. The former approximation is based on the minimum energy principle and was pioneered by Frank and Van der Merwe. The latter, known as the theory of the balance of forces, belongs to Matthews and Blakeslee [16]. In our calculations, we have used the model of balance of forces in which critical epilayer thickness can be estimated according to [16]:

$$h_c = \left(\frac{b}{\varepsilon_m}\right)\frac{1}{8\pi(1+\nu)}\left[\ln\left(\alpha\frac{h_c}{b}\right)+\beta\right], \tag{15}$$

where ν is the Poisson coefficient, b – is the Burgers vector modulus (Fig. 3). As long as in semiconductor epilayers, 60° misfit dislocations are most common in (001) plane, the Burgers vector can be written as $(a_{avg}/2) < 110 >$ [8, 9]. The stresses in the region of the dislocation center are too high to be correctly described within the linear elasticity theory, so we have introduced a phenomenological parameter β as a measure of this deviation.

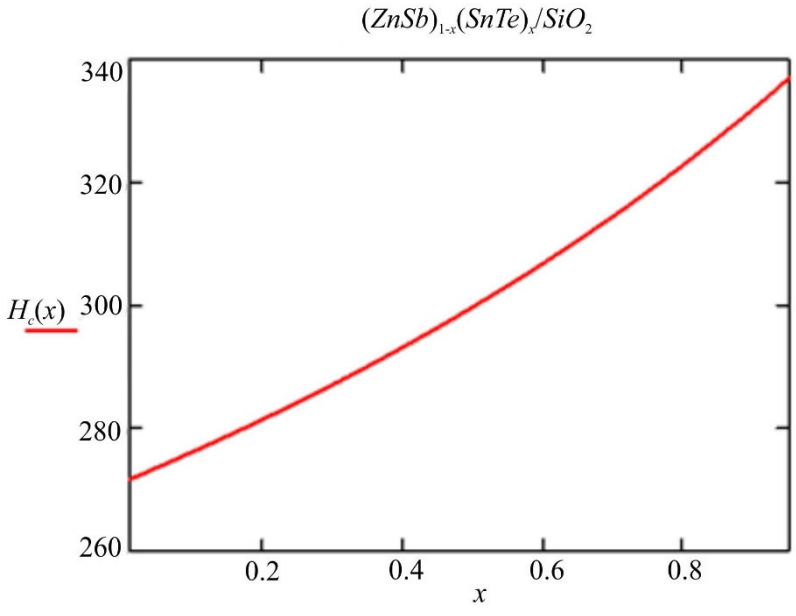

Fig. 3. Critical thickness h_C, Å as a function of composition x of ZnSb-SnTe/SiO_2 thin films

Let us return to the phase $T - x$ diagrams of the pseudo-binary *ZnSb-SnTe*/SiO_2 thin films. Fig. 2 shows the results of calculations for films with a thickness of 30 and 100 nm on a SiO_2 substrate, which corresponds to the conditions of the experiment [7].

As can be seen from our calculations, with increasing film thickness, the critical temperature of spinodal decomposition decreases, and the spinodal becomes a more symmetrical curve. In particular, at h = 30 nm T_c = 610K, x_c = 0.48; at h = 100 nm T_c = 600 K, x_c = 05. At the same time, the annealing of the films at ~ 225°C leads to the beginning of the decomposition of the alloy (x = 0.27) with the formation of a *SnSb* phase. As it follows from experimental studies [7], the formation of nanoprecipitates of the SnSb metal phase turned out to be the main driving force together with IMT in a high power factor of 3383 $\mu Wm^{-1}K^{-1}$ at 300 °C.

Conclusions

On the basis of thermodynamic analysis, we investigated the phase stability of films of the pseudobinary semiconductor alloys *ZnSb-SnTe*. Obtained T - x phase diagrams made it possible to predict the existence of the wide miscibility gap. Taking into account small internal stresses and the influence of the quartz substrate did not lead to significant changes in the phase diagram depending on the film thickness. The processes of spinodal decomposition of $(ZnSb)_{1-x}(SnTe)_x$ caused by annealing at T = 225°C in alloys at x = 0.27 lead to microstructural evolution with the formation of precipitates of the *SnSb* metallic phase, which is consistent with experimental studies. The latter is the reason for the sharp increase in the power factor to 3383 $\mu Wm^{-1}K^{-1}$ at 300 °C, and the described recrystallization processes are the main mechanism of the high thermoelectric performance of this material.

This work is supported in part by e-COST Action CA20116. The author is grateful to academician L. Anatychuk for the approval of the research subject and interest in the work.

References

1. Anatychuk L. I. and Vikhor L. N. (2012). Functionally Graded Thermoelectric Materials. Chernistvi: Institute of Thermoelectricity. *J.Thermoelectricity,* 4.
2. Marciá-Barber E. (2015). *Thermoelectric Materials. Advances and Applications*. New York Taylor & Francis Group, Pan Stanford.
3. Urban J. J., Menon A. K., Tian Z., Jain A., Hippalgaonkar K. New horizons in thermoelectric materials: Correlated electrons, organic transport, machine learning, and more. *J. Appl. Phys*. 2019. 125(5). 180902.
4. Li C., Jiang F., Liu C., Liu P., Xu J. (2019)Present and future thermoelectric materials toward wearable energy harvesting, *Applied Materials Today*. 15(6). 543 – 557 p.
5. Deibuk V. G. (2017). Thermodynamic stability of thin *CdZnSb* epitaxial films, *J. Thermoelectricity,* 1. P.44 – 52.
6. Li X, , Cai K., Gao M., Du Y., Shen S. (2021). Recent advances in flexible thermoelectric films and devices, *Nano Energy*. 89A(11). 106309.
7. Wang G., Zhang Y., Lotnyk A., Shi H., Chen C. (2021). High thermoelectric performance in *ZnSb-SnTe* pseudo-binary materials, *Scripta Materialia.* 194(3) 113670.
8. Chen A.-B., Sher A. (2011). *Semiconductor Alloys: Physics and Materials Engineering*. New York, Plenum Press,.
9. Stringfellow G. B. (2021). Epitaxial growth of metastable semiconductor alloys, *J. Cryst. Growth.* 564(6). 126065.

10. Landau L. D., and Lifshitz E.M. (2005). *Theory of Elasticity, Course of Theoretical Physics*, Vol. 7. London, Elsevier.
11. Zhang Y., Sun J., Shuai J., Tang X., Tan G. (2021). Lead-free *SnTe*-based compounds as advanced thermoelectrics, *Materials Today Physics.* 19(7). 100405.
12. Ronneberger I., Zanolli Z., Wuttig M., Mazzarello R. (2020). Changes of Structure and Bonding with Thickness in Chalcogenide Thin Films, *Adv. Mater*. 32(8). 2001033.
13. Hsu S.-C., Hong J.-Y., Chen C.-L., et al. (2021). The structures and thermoelectric properties of *Zn-Sb* alloy films fabricated by electron beam evaporation through an ion beam assisted deposition, *Applied Surface Science.* 540(2). 148264.
14. Sarkar P., Pandey J., AnsarH. S. et al., (2020.) Environment friendly SnTe thermoelectrics: Material to device, *AIP Conf. Proc.* 2265(11). 030628.
15. Beanland R. , Dunstan D. J. & Goodhew P. J. (1996). Plastic relaxation and relaxed buffer layers for semiconductor epitaxy, *Advances in Physics*. 45(1). 87 – 146 p.
16. Dunstan D. J. (2012). Critical Thickness Theory Applied to Micromechanical Testing, *Adv. Eng. Mater*., 14(3). 942 - 947 p..
17. Liu M., Ruan H., Zhang L., *et al,* (2012). Effects of misfit dislocation and film-thickness on the residual stresses in epitaxial thin film systems: Experimental analysis and modeling, *Journal of Materials Research*. 27(11). 2737 – 2745 p.
18. The Materials Project. https://next-gen.materialsproject.org/ (accessed January 11, 2024)
19. Yazawa K., Bahk J.-H., Shakouri A. (2021). *Thermoelectric Energy Conversion Devices and Systems. WSPC Series in Advanced Integration and Packing.* Singapore, World Scientific.
20. Ohkubo I., Murata M., Lima M. S. L., et al. (2022). Miniaturized in-plane π-type thermoelectric device composed of a II–IV semiconductor thin film prepared by microfabrication, *Materials Today Energy.* 28(1). 101075.

Subminitted: 10.01.2023

Дейбук В. Г., *доктор фіз.-мат. наук, професор*[1,2]

[1]Інститут термоелектрики НАН та МОН України,
вул. Науки, 1, Чернівці, 58029, Україна;
[2]Чернівецький національний університет імені Юрія Федьковича,
вул. Коцюбинського 2, Чернівці, 58012, Україна
e-mail: v.deibuk@chnu.edu.ua

ФАЗОВА СТАБІЛЬНІСТЬ ТЕРМОЕЛЕКТРИЧНИХ ТОНКИХ ПЛІВОК *ZnSb-SnTe*

У статті теоретично досліджено фазову стабільність тонких плівок псевдобінарних напівпровідникових сплавів ZnSb-SnTe. Отримані T – x фазові діаграми дозволили передбачити існування широкого інтервалу незмішуваності. Врахування малих внутрішніх напружень та впливу кварцової підкладки не призвело до істотних змін фазової діаграми залежно від товщини плівки. Показано, що процеси спінодального розпаду, спричинені відпалом при T = 225 °C у сплавах $(ZnSb)_{1-x}(SnTe)_x$ при x = 0.27, призводять до мікроструктурної еволюції з утворенням виділень металевої фази SnSb. Цей факт добре узгоджується з експериментальними дослідженнями розглянутих тонких плівок і є причиною різкого зростання коефіцієнта потужності до 3383 $\mu Wm^{-1}K^{-1}$ при 300 °C. Описані процеси рекристалізації є основним механізмом високих термоелектричних характеристик цього матеріалу. Бібл. 20, рис. 3.

Ключові слова: тонкі плівки, термоелектричні матеріали, спінодальний розпад, фазова стабільність.

References

1. Anatychuk L. I. and Vikhor L. N. (2012). Functionally Graded Thermoelectric Materials. Chernistvi: Institute of Thermoelectricity. *J.Thermoelectricity,* 4.
2. Marciá-Barber E. (2015). *Thermoelectric Materials. Advances and Applications*. New York Taylor & Francis Group, Pan Stanford.
3. Urban J. J., Menon A. K., Tian Z., Jain A., Hippalgaonkar K. New horizons in thermoelectric materials: Correlated electrons, organic transport, machine learning, and more. *J. Appl. Phys*. 2019. 125(5). 180902.
4. Li C., Jiang F., Liu C., Liu P., Xu J. (2019)Present and future thermoelectric materials toward wearable energy harvesting, *Applied Materials Today*. 15(6). 543 – 557 p.
5. Deibuk V. G. (2017). Thermodynamic stability of thin *CdZnSb* epitaxial films, *J. Thermoelectricity,* 1. P.44 – 52.
6. Li X, , Cai K., Gao M., Du Y., Shen S. (2021). Recent advances in flexible thermoelectric films and devices, *Nano Energy*. 89A(11). 106309.
7. Wang G., Zhang Y., Lotnyk A., Shi H., Chen C. (2021). High thermoelectric performance in *ZnSb-SnTe* pseudo-binary materials, *Scripta Materialia.* 194(3) 113670.
8. Chen A.-B., Sher A. (2011). *Semiconductor Alloys: Physics and Materials Engineering*. New York, Plenum Press,.
9. Stringfellow G. B. (2021). Epitaxial growth of metastable semiconductor alloys, *J. Cryst. Growth.* 564(6). 126065.
10. Landau L. D., and Lifshitz E.M. (2005). *Theory of Elasticity, Course of Theoretical Physics*, Vol. 7. London, Elsevier.
11. Zhang Y., Sun J., Shuai J., Tang X., Tan G. (2021). Lead-free *SnTe*-based compounds as advanced thermoelectrics, *Materials Today Physics.* 19(7). 100405.
12. Ronneberger I., Zanolli Z., Wuttig M., Mazzarello R. (2020). Changes of Structure and Bonding with Thickness in Chalcogenide Thin Films, *Adv. Mater*. 32(8). 2001033.
13. Hsu S.-C., Hong J.-Y., Chen C.-L., et al. (2021). The structures and thermoelectric properties of *Zn-Sb* alloy films fabricated by electron beam evaporation through an ion beam assisted deposition, *Applied Surface Science.* 540(2). 148264.

14. Sarkar P., Pandey J., AnsarH. S. et al., (2020.) Environment friendly SnTe thermoelectrics: Material to device, *AIP Conf. Proc.* 2265(11). 030628.
15. Beanland R. , Dunstan D. J. & Goodhew P. J. (1996). Plastic relaxation and relaxed buffer layers for semiconductor epitaxy, *Advances in Physics*. 45(1). 87 – 146 p.
16. Dunstan D. J. (2012). Critical Thickness Theory Applied to Micromechanical Testing, *Adv. Eng. Mater*., 14(3). 942 - 947 p..
17. Liu M., Ruan H., Zhang L., *et al,* (2012). Effects of misfit dislocation and film-thickness on the residual stresses in epitaxial thin film systems: Experimental analysis and modeling, *Journal of Materials Research*. 27(11). 2737 – 2745 p.
18. The Materials Project. https://next-gen.materialsproject.org/ (accessed January 11, 2024)
19. Yazawa K., Bahk J.-H., Shakouri A. (2021). *Thermoelectric Energy Conversion Devices and Systems. WSPC Series in Advanced Integration and Packing.* Singapore, World Scientific.
20. Ohkubo I., Murata M., Lima M. S. L., et al. (2022). Miniaturized in-plane π-type thermoelectric device composed of a II–IV semiconductor thin film prepared by microfabrication, *Materials Today Energy.* 28(1). 101075.

Subminitted: 10.01.2023

O. M. Manyk, *cand phys – math sciences*[1]
T. O. Manyk, *cand phys – math sciences*[2]
V. R. Bilynskyi-Slotylo, *cand phys – math sciences*[1]

[1]Yuriy Fedkovych Chernivtsi National University,
2 Kotsiubynskyi str., Chernivtsi, 58012, Ukraine,
e-mail: o.manyk@chnu.edu.ua,
e-mail: slotulo@gmail.com
[2] Military University of Technology Jaroslaw Dombrowski,
str. gene Sylwester Kaliskiego, 2,
Warsaw 46, 00-908, Poland,
e-mail: tetjana.manyk@wat.edu.pl

THEORETICAL MODELS OF ORDERED ALLOYS OF TERNARY SYSTEMS OF THERMOELECTRIC MATERIALS 3. CHEMICAL BOND AND STATE DIAGRAMS OF *Cd-Zn-Sb*

A diagram of the distribution of phase regions in the Cd-Zn-Sb system was constructed based on the isothermal sections of intermediate binary compounds Cd-Zn, Cd-Sb, and Zn-Sb. The results of calculations of effective radii, electron density redistribution and dissociation energy of non-equivalent chemical bonds depending on interatomic distances in the Cd-Zn-Sb ternary system are presented. Bibl. 7, Fig. 4, Tabl. 6.

Key words: theoretical models, chemical bond, state diagrams, effective radii, dissociation energies, interatomic interaction.

Introduction

This work is a continuation of studies begun in [1] on ordered alloys of cadmium antimonides using statistical and thermodynamic methods and is devoted to the construction of theoretical models of ordered alloys of ternary systems and state diagrams of *Cd-Zn-S*b from the standpoint of chemical bond.

The need to conduct such studies is due to the fact that the nature of chemical bond in such systems varies from metallic to ionic, covalent, and intermediate in layered sublattices.

In turn, a change in the chemical bond is reflected in a change in the structure of the short-range order of interatomic interaction, which, in turn, is associated with the features of state diagrams and phase transformations both in the solid state and in melts.

However, it should be noted that there is no consistent theory of phase transformations yet. That is why in this work the task was set to obtain theoretical schemes of state diagrams of ternary *Cd-Zn-Sb* systems and to calculate the parameters of chemical bonds using microscopic theory methods.

This approach allows us to generalize experimental data for binary state diagrams (*Cd-Zn*, *Cd-Sb*, *Zn-Sb*) to the case of ternary systems (*Cd-Zn-Sb*), and calculations of chemical bond parameters can be used to correct physicochemical properties of the resulting materials.

The availability of such information makes it possible to get closer to the solutions of the problems of melting and crystallization processes of ternary systems.

State diagrams

To solve the problem, it was necessary to summarize the results of experimental studies of binary state diagrams of *Cd-Zn*, *Cd-Sb*, *Zn-Sb* [2], physicochemical properties, and theoretical studies of quantum regularities of the original components [3, 4].

The results of state diagram studies were summarized by constructing isothermal sections (*Cd-Zn*, *Cd-Sb*, *Zn-Sb*) and solving the inverse problem. Its essence is that, unlike the direct problem, when the study of a complex system is carried out by breaking it down into simpler ones, according to established rules and patterns, in the case of the inverse problem, the elements *Cd*, *Zn*, *Sb* and state diagrams of binary systems *Cd-Zn*, *Cd-Sb*, *Zn-Sb* were chosen as the initial data. Next, based on the analyzed patterns, the components of the *Cd-Zn-Sb* ternary system were constructed. What was new in the study of ternary systems of cadmium and zinc antimonides was that to solve the problem, a triangulation method was used, based on the geometric properties of a triangle [5].

This mathematical approach makes it possible to solve a number of problems in physics, chemistry, and mathematics. In particular, in chemistry, when studying state diagrams of ternary systems, this approach allows for the distribution of such systems taking into account the chemical interaction between the elements *Cd*, *Zn*, *Sb*, located at the vertices of the triangle (solubility; substitution; exchange; formation of compounds; formation of solid solutions and mechanical mixtures), and the parameters of phase transformations can be found by means of theoretical calculations using the methods of quantum chemistry.

When constructing the theoretical model of *Cd-Zn-Sb*, first the analysis of binary state diagrams was given and isothermal sections were constructed at different temperatures. Further, by constructing conode triangles, the quantitative ratios of coexisting phases were determined and the limits of phase equilibrium in ternary systems in the liquid-crystal regions were established. This made it possible to predict cases of congruent and incongruent melting. The obtained results are shown in Fig. 1-4, where the following designations are entered:

α – solid phase based on *Cd*; β – solid phase based on *Zn*; γ – solid phase based on *Sb*; ε – solid phase based on *Cd-Zn* binary systems; ρ – solid phase based on *Zn-Sb* binary systems; δ – solid phase based on *Cd-Sb* binary systems; σ – solid phase based on *Cd-Zn-Sb* ternary system; *L* – liquid phase.

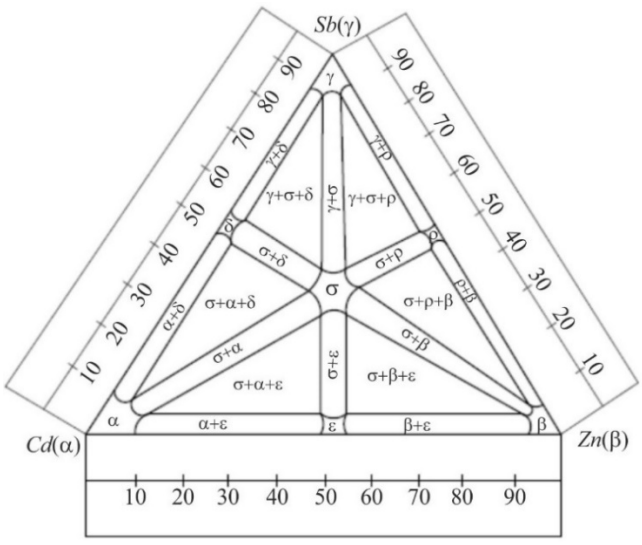

Fig. 1. A diagram of the distribution of Cd-Zn-Sb equilibrium phase regions in the solid state

Fig. 1 shows a diagram of the distribution of *Cd-Zn-Sb* phase regions in the solid state. The *Cd-Zn-Sb* ternary system was divided into six ordered ternary subsystems. This made it possible to consider interatomic interaction in a specific subsystem both from the standpoint of state diagrams and chemical bonds.

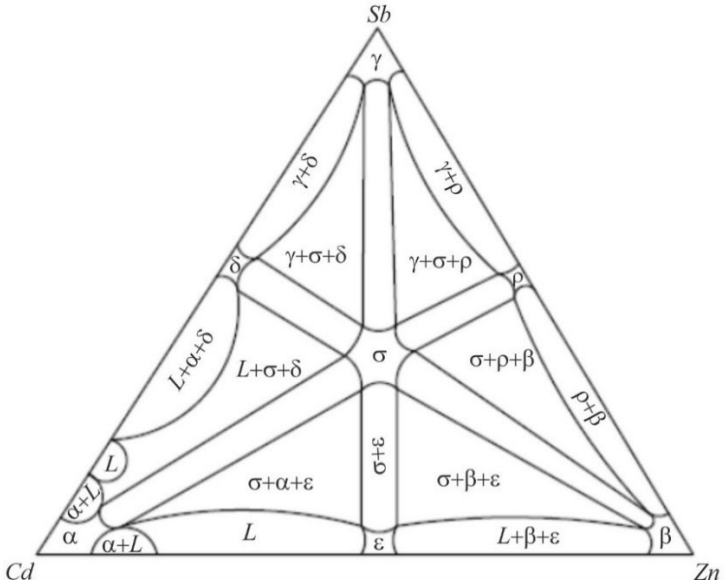

Fig. 2. Cd-Zn-Sb isothermal section at t=300°C

Fig. 2 shows an isothermal section at a temperature t = 300 °C, which is lower than the melting point of the *Cd*, *Zn*, *Sb* components and at the same time higher than the temperature of the first eutectic of the *Cd-Zn* system. Part of the cross section (35 %) of *Cd-Zn* is occupied by liquid *L*. Two-phase equilibrium (*L*+α), (*L*+ε), is carried out by primary crystals α and crystals ε (based on Cd_n Zn_m compounds) and liquid. Three-phase equilibrium (*L*+ε+β) is carried out by primary β crystals, ε crystals and liquid.

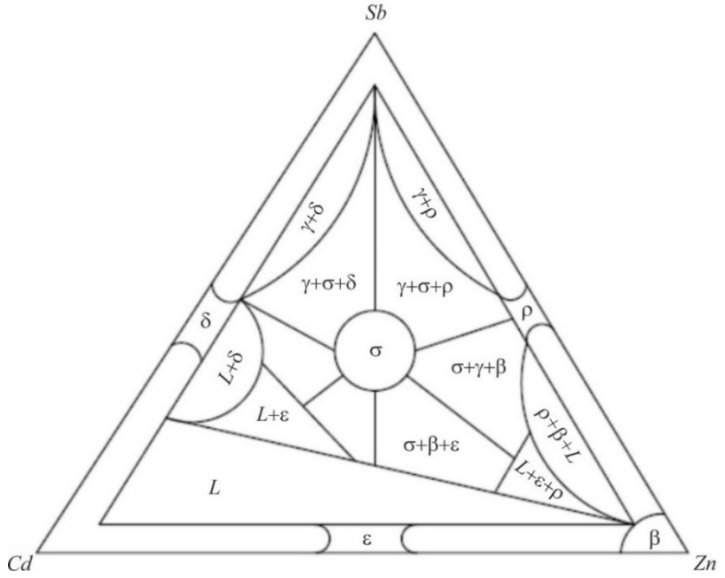

Fig. 3. Cd-Zn-Sb isothermal section at t=400°C

Fig. 3 shows an isothermal section at a temperature of 400 °C, which is lower than the melting point of *Zn* and *Sb*. But higher than the melting point of *Cd* (321°C). Most of the *Cd-Zn* cross section is occupied by liquid *L*, but unlike the previous case, the cross section contains conode triangles with equilibrium phases (*L*+ε+δ) and (*L*+ε+ρ), which are formed by crystals (ε+δ) and (ε+ρ) based on *Cd-Sb* and *Zn-Sb* compounds and liquid *L*. This division of ternary systems into separate sections of double state diagrams makes it possible to study the fine structure of cooling and heating depending on the short-range order of the chemical bond.

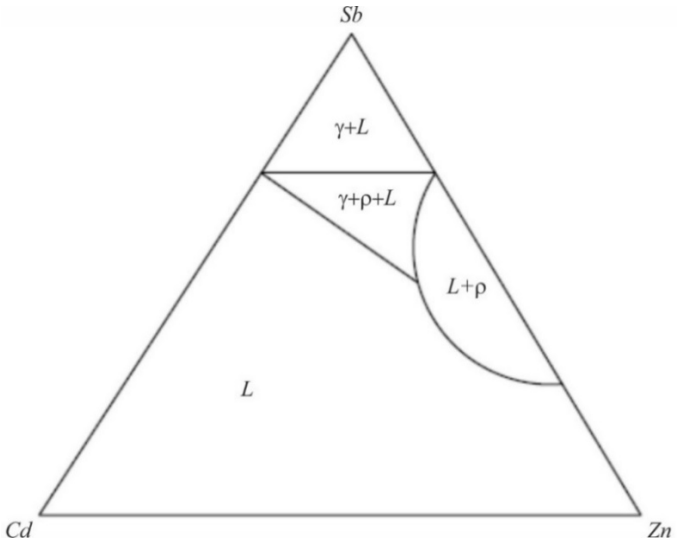

Fig. 4. Cd-Zn-Sb isothermal section at t=500°C

Fig. 4 shows the isothermal section at t = 500 °C above the melting point of *Cd* and *Zn*. The entire cross section of *Cd-Zn* is occupied by liquid, and in the *Zn-Sb* and *Cd-Sb* diagrams three-phase equilibria are represented by a conode triangle with phases (L + γ + ρ). Thus, the given isothermal sections make it possible to:

1. Find the limits of phase equilibrium in the liquid-crystal regions and between transformations in the solid state.
2. Separate phase diagrams corresponding to chemical compounds and solid solutions of different concentrations and mechanical mixtures.
3. Determine quantitative ratios of coexisting phases.
4. Determine the structure of the cooling and heating processes depending on the short-range order of the chemical bond.

However, it should be borne in mind that the results of studies of isothermal sections alone are not yet sufficient to determine the temperature intervals of phase transitions in multicomponent systems. Theoretical calculations of the interatomic interaction energy in the liquid and solid phases are required, depending on the interatomic distances from the standpoint of chemical bond.

Theoretical models of chemical bonding of ordered *Cd-Zn-Sb* alloys

A joint consideration of the methods of experimental and theoretical approaches in the quantitative method of calculating the parameters of the electronic structure of matter is associated with the emergence of qualitatively new ideas, which is not the result of the development of existing theories, but also negates some of them.

Thus, the formation of a chemical bond is accompanied by a rearrangement of the valence shells of the interacting atoms and leads to the need to use a number of concepts for their description. Despite the imperfection, from a theoretical point of view, of these concepts and other empirical criteria, their positive role in the systematization of experimental data and the development of ideas about the nature of interatomic interaction is beyond doubt.

The equations given in [6] were used in the calculations of effective charges, effective radii, dissociation energies of non-equivalent chemical bonds that are part of the *Cd-Zn-Sb* ternary system.

Analytical relationships reflecting the quantum laws of interatomic interaction given in [6] made it possible to write down the expression for the energy of chemical bonds in the form:

$$D_{A-B}^{0} = \left(\frac{C_1\left(R_{UA}^{0}+R_{UB}^{0}\right)}{(\mathrm{tg}\,\alpha_A+\mathrm{tg}\,\alpha_B)}\right)\left(\frac{C_2 d_i}{d_i^2-R_{UA}R_{UB}}-\frac{1}{d_i}\right), \quad (1)$$

where $R_{UA(B)}^{0}$ is the radius of $A(B)$ atoms in the unexcited state; $\mathrm{tg}\,\alpha$ reflects the dependence of the ionic radius R_U on the number of electrons in the orbitals of converging atoms; d_i is interatomic distance of i-chemical bond; C_1 is a coefficient that reflects the relationship between dimensional and energetic characteristics of interatomic interaction; C_2 is a coefficient depending on the type of crystal structure and chemical bond.

The results of the calculations are given in tables 1-6. The values of the coefficients C_1 and C_2 in the first approximation are chosen to be equal to unity.

Table 1

Effective charges, effective radii, dissociation energies depending on interatomic distances of Zn-Zn NHO

Zn-Zn NHO / Parameters	*Zn-Zn*					
	φ1	φ2	φ3	φ4	φ5	φ6
d_i(Å)	2.8	2.9	3.0	3.1	3.2	3.3
R_U^{Zn}(Å)	1.40	1.45	1.50	1.55	1.60	1.65
$\Delta q_i(\varphi_i)$	-0.08	-0.18	-0.3	-0.4	-0.5	-0.6
$D(\varphi_i)$ *ev*	1.268	1.166	1.128	1.091	1.057	1.025

Table 2

Effective charges, effective radii, dissociation energies depending on interatomic distances of Zn-Cd NHO

Zn-Cd NHO / Parameters	*Zn-Cd*					
	φ1	φ2	φ3	φ4	φ5	φ6
d_i(Å)	2.8	2.9	3.0	3.1	3.2	3.3
R_U^{Cd}(Å)	1.475	1.52	1.56	1.61	1.65	1.69
R_U^{Zn}(Å)	1.325	1.38	1.44	1.49	1.55	1.61

Continuation of table 2

$\Delta q_i(\varphi_i)$	0.1	-0.025	-0.15	-0.28	-0.4	-0.52
$D(\varphi_i)$ *ev*	1.471	1.422	1.376	1.332	1.291	1.253

Table 3

Effective charges, effective radii, dissociation energies depending on interatomic distances of Zn-Sb NHO

Zn-Sb NHO / Parameters	*Zn-Sb*					
	φ_1	φ_2	φ_3	φ_4	φ_5	φ_6
d_i(Å)	2.8	2.9	3.0	3.1	3.2	3.3
R_U^{Zn}(Å)	1.36	1.42	1.485	1.55	1.615	1.68
R_U^{Sb}(Å)	1.44	1.48	1.515	1.55	1.585	1.62
$\Delta q_i(\varphi_i)$	0.25	-0.12	-0.25	-0.4	-0.52	-0.65
$D(\varphi_i)$ *ev*	1.605	1.550	1.500	1.450	1.405	1.362

Table 4

Effective charges, effective radii, dissociation energies depending on interatomic distances of Cd-Cd NHO

Cd-Cd NHO / Parameters	*Cd-Cd*					
	φ_1	φ_2	φ_3	φ_4	φ_5	φ_6
d_i(Å)	2.8	2.9	3.0	3.1	3.2	3.3
R_U^{Cd}(Å)	1.4	1.45	1.5	1.55	1.6	1.65
$\Delta q_i(\varphi_i)$	0.33	0.18	0.025	-0.05	-0.27	-0.4
$D(\varphi_i)$ *ev*	1.853	1.789	1.730	1.674	1.622	1.572

Table 5

Effective charges, effective radii, dissociation energies depending on interatomic distances of Sb-Sb NHO

Sb-Sb NHO / Parameters	*Sb-Sb*					
	φ_1	φ_2	φ_3	φ_4	φ_5	φ_6
d_i(Å)	2.8	2.9	3.0	3.1	3.2	3.3
R_U^{Sb}(Å)	1.4	1.45	1.5	1.55	1.6	1.65
$\Delta q_i(\varphi_i)$	0.2	0	-0.2	-0.39	-0.6	-0.75
$D(\varphi_i)$ *ev*	2.332	2.252	2.177	2.107	2.041	1.980

Table 6

Effective charges, effective radii, dissociation energies depending on interatomic distances of Cd-Sb NHO

Cd-Sb NHO / Parameters	*Cd-Sb*					
	φ_1	φ_2	φ_3	φ_4	φ_5	φ_6
d_i(Å)	2.8	2.9	3.0	3.1	3.2	3.3
R_U^{Cd}(Å)	1.42	1.48	1.53	1.6	1.65	1.71
R_U^{Sb}(Å)	1.38	1.42	1.47	1.5	1.55	1.59
$\Delta q_i(\varphi_i)$	0.27	0.1	-0.06	-0.22	-0.4	-0.55
$D(\varphi_i)$ *ev*	2.061	1.989	1.922	1.859	1.800	1.746

Discussion of the results

As follows from the results presented in tables 1-2, with the growth of interatomic distances, the dissociation energy of the corresponding chemical bonds decreases, and the redistribution of electron density in different intervals of interatomic distances changes differently: in *Cd-Cd* structural variants, the redistribution of electron density changes sign in the interval $3 \le d_i \le 3.1$ Å; (*Zn-Zn*) for all distances $2.8 \le d_i \le 3.3$ Å; (*Cd-Zn*) changes sign in the interval $2.8 \le d_i \le 2.9$ Å; (*Zn-Sb*) changes sign in the interval $2.8 \le d_i \le 2.9$ Å; (*Cd-Sb*) changes sign in the interval $2.9 \le d_i \le 3$ Å.

In addition, the obtained results confirm the fact that the overall diagram of *Cd-Zn-Sb* consists of three partial equilibrium stability diagrams of *CdSb-ZnSb* (*Cd*, *Sb*, *Zn*), three metastable Cd_4Sb_3-Zn_4Sb_3 (*Cd*, *Zn*, *Sb*) and three metastable Cd_3Sb_2-Zn_3Sb_2 (*Cd*, *Zn*, *Sb*) [7]. In this system, different structural states of melts can form. Therefore, solving problems of technology and optimization of materials based on *Cd-Zn-Sb* must be carried out taking into consideration the characteristics of the chemical bond of both the initial components (*Cd*, *Zn*, *Sb*) and intermediate systems (*Cd-Sb*, *Zn-Sb*, *Cd-Zn*).

Conclusions

1. A methodology has been proposed and theoretical models of short-range order of melts have been constructed using triangulation methods and isothermal sections in *Cd-Zn-Sb* ternary systems.
2. Calculations of chemical bond parameters in *Cd-Zn-Sb* systems depending on interatomic distances and atomic characteristics of the initial components are given.
3. It was shown for the first time that the redistribution of electron density leads to the formation of donor and acceptor chemical bonds in melts.
4. The results obtained are consistent with the results of calculations of chemical bond parameters using microscopic theory methods and optimize the technological capabilities of the synthesis of metastable phases based on *Cd-Zn-Sb* with predicted parameters.

References

1. Manik O. M., Manik T. O., Bilynskyi-Slotylo V. R. (2017.). Crystalline structure and chemical bond of *Cd- Sb-Zn*. *J. Thermoelectricity*, 5. P. 32 – 38.
2. Hansen M., Anderko K. (1958). *Constitution of Binary Alloys*, *2nd Ed*. New York: McGraw-Hill, p. 118.

3. Manik O. M., Manik T. O., Bilynskyi-Slotylo V.R. (2018). Theoretical models of ordered alloys of cadmium antimonide. *J. Thermoelectricity,* 4, 4 – 30.
4. Ashcheulov A. A., Manik O. N., Manik T. O., Bilynskyi-Slotylo V. R. (2011). Structural-energetic representations of chemical bond between cadmium and zinc. *Metal Physics and Advanced Technologies,* 33(7), 959 – 967.
5. Barchiy I. E., Peresh E. Yu., Rizak V. M., Khudolii V. O. (2003). *Heterogenni rivnovahy. [Heterogeneous equilibria]. Uzhhorod*: Zakarrpattia Publ. [in Ukrainian].
6. Manik O. M., Manik T. O., Bilynskyi-Slotylo V. R. (2021). Theoretical models of ordered alloys of ternary systems of thermoelectric materials. 1. Chemical bond and diagrams of state of *In-Cd-Sb*. *J. Thermoelectricity*. 2, 32 – 42.
7. Dremliuzhenko S. G. (2002). *Sistemy na osnove CdSb. Diagrammy sostoianiia, polucheniie i svoistva splavov. [Systems on the basis of CdSb. Diagrams of state, fabrication and properties of alloys].* Chernivtsi: Ruta [in Russian].

Submitted: 17.02.2023

Маник О. М., *канд. фіз.-мат. наук*[1]
Маник Т. О., *канд. фіз.-мат. наук*[2]
Білинський-Слотило В. Р., *канд. фіз.-мат. наук*[1]

[1]Чернівецький національний університет імені Юрія Федьковича,
вул. Коцюбинського 2, Чернівці, 58012, Україна,
e-mail: o.manyk@chnu.edu.ua, slotulo@gmail.com
[2]Військово-технічний університет ім. Ярослава Домбровського,
вул. ген. Сільвестра Каліського, 2, Варшава 46, 00-908, Польща,
e-mail: tetjana.manyk@wat.edu.pl

ТЕОРЕТИЧНІ МОДЕЛІ ВПОРЯДКОВУВАНИХ СПЛАВІВ ПОТРІЙНИХ СИСТЕМ ТЕРМОЕЛЕКТРИЧНИХ МАТЕРІАЛІВ. 3. ХІМІЧНИЙ ЗВ'ЯЗОК ТА ДІАГРАМИ СТАНУ *Cd-Zn-Sb*

Побудовано схему розподілу фазових областей в системі Cd-Zn-Sb на основі ізотермічних перерізів проміжних бінарних сполук Cd-Zn, Cd-Sb, Zn-Sb. Представлено результати розрахунків ефективних радіусів, перерозподілу електронної густини та енергії дисоціації нееквівалентних хімічних зв'язків в залежності від міжатомних віддалей в потрійній системі Cd-Zn-Sb. Бібл. 7, рис. 4, табл. 6.

Ключові слова: теоретичні моделі, хімічний зв'язок, діаграми стану, ефективні радіуси, енергії дисоціації, міжатомна взаємодія.

References

1. Manik O. M., Manik T. O., Bilynskyi-Slotylo V. R. (2017). Crystalline structure and chemical bond of *Cd- Sb-Zn*. *J. Thermoelectricity*, 5, 32 - 38.
2. Hansen M., Anderko K. (1958). *Constitution of Binary Alloys*, *2nd Ed*. New York: McGraw-Hill, p. 118.
3. Manik O. M., Manik T. O., Bilynskyi-Slotylo V.R. (2018). Theoretical models of ordered alloys of cadmium antimonide. *J. Thermoelectricity,* 4, 4 - 30.
4. Ashcheulov A. A., Manik O. N., Manik T. O., Bilynskyi-Slotylo V. R. (2011). Structural-energetic representations of chemical bond between cadmium and zinc. *Metal Physics and Advanced Technologies,* 33(7), 959-967.
5. Barchiy I. E., Peresh E. Yu., Rizak V. M., Khudolii V. O. (2003). *Heterogenni rivnovahy. [Heterogeneous equilibria]. Uzhhorod*: Zakarrpattia Publ. [in Ukrainian].
6. Manik O. M., Manik T. O., Bilynskyi-Slotylo V. R. (2021). Theoretical models of ordered alloys of ternary systems of thermoelectric materials. 1. Chemical bond and diagrams of state of *In-Cd-Sb*. *J.Thermoelectricity*, 2, 32 - 42.
7. Dremliuzhenko S. G. (2002). *Sistemy na osnove CdSb. Diagrammy sostoianiia, polucheniie i svoistva splavov. [Systems on the basis of CdSb. Diagrams of state, fabrication and properties of alloys].* Chernivtsi: Ruta [in Russian].

Submitted: 17.02.2023

V. A. Romaka *doc. tech. science, professor*[1],
Yu. V. Stadnyk *cand. chem. science*[2],
L. P. Romaka *cand. chem. science*[2],
P. Yu. Demchenko [2],
A. M. Horyn *cand. chem. science*[2],
T. I. Lukovskyi [1]

[1]National University "Lvivska Politechnika", 12,
S. Bandera Str., Lviv, 79013, Ukraine, *e-mail: vromaka@polynet.lviv.ua*
[2]Ivan Franko National University of Lviv, 6, Kyryla and Mefodiya Str.,
Lviv, 79005, Ukraine, *e-mail: lyubov.romaka@lnu.edu.ua*

EXPERIMENTAL INVESTIGATIONS OF THE PROPERTIES OF A NEW THERMOELECTRIC MATERIAL $Tm_{1-x}V_xNiSb$

The structural, kinetic, and energy properties of the $Tm_{1-x}V_xNiSb$ thermoelectric material were studied in the ranges: T=80–400 K, x=0–0.10. It is shown that V atoms can simultaneously occupy different crystallographic positions in different ratios, generating defects of acceptor and donor nature. This gives rise to the corresponding acceptor and donor states in the bandgap ε_g $Tm_{1-x}V_xNiSb$. The mechanism of formation in $Tm_{1-x}V_xNiSb$ of two types of acceptor states with different depth of occurrence was established: shallow acceptors generated by vacancies in the structure of half-Heusler phase TmNiSb, and deep acceptors formed by defects when Ni atoms are replaced by V in the 4c position. The ratio of the concentrations of generated defects determines the position of the Fermi level ε_F and the conduction mechanisms. The investigated $Tm_{1-x}V_xNiSb$ solid solution is a promising thermoelectric material. Bibl. 12, Fig. 7.

Keywords: electronic structure, electric resistivity, Seebeck coefficient.

Introducion

Semiconductor solid solutions based on half-Heusler phases *RNiSb* (*R* – rare earth metals of the Ittrium subgroup) is a new and promising class of thermoelectric materials with a high efficiency of thermal into electric energy conversion [1]. The formation of substitutional solid solutions based on *RNiSb* is accompanied by the generation of defects of donor or acceptor nature in the crystal structure, and corresponding energy states appear in the bandgap ε_g. This makes it possible to smoothly change the values of electrical conductivity $\sigma(T)$, Seebeck coefficient $\alpha(T)$ and thermal conductivity $\kappa(T)$, and the process of optimizing the properties of thermoelectric material becomes predictable [2].

In this context, it seems interesting to study a new thermoelectric material $Tm_{1-x}V_xNiSb$, when *V* ($3d^34s^2$) atoms are introduced into the structure of the half-Heusler phase *TmNiSb* (structure type *MgAgAs*, spatial group $F\bar{4}3m$ [3]) by substituting in the crystallographic position 4*a* of atoms *Tm* ($5d^06s^2$). The introduction of *V* atoms into the structure of the *TmNiSb* compound should generate defects of donor nature (*V* has more *d*-electrons than *Tm*), and corresponding donor states will appear in the bandgap ε_g of $Tm_{1-x}V_xNiSb$. The *TmNiSb* compound was discovered during the study of phase equilibria in the *Tm-Ni-Sb* system which turned out to be a hole-type semiconductor, as indicated by the positive values of the Seebeck coefficient α (Fig. 1*a*) [4, 5].

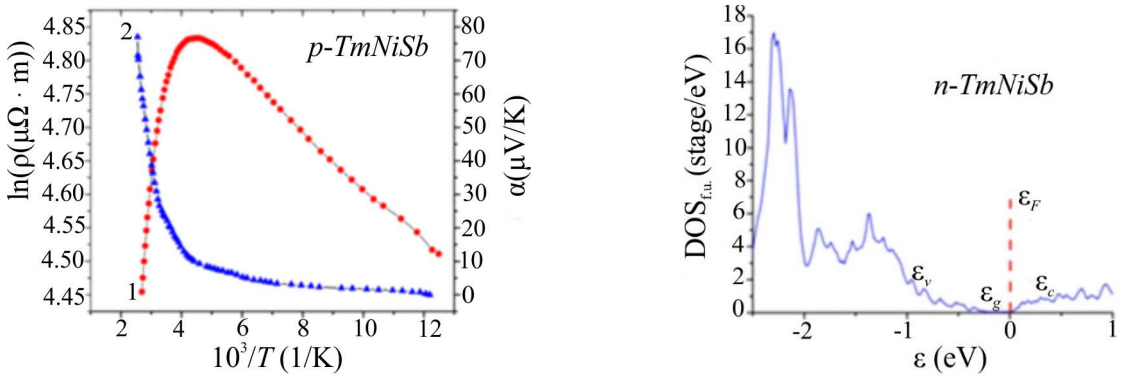

Fig. 1. Temperature dependences of electrical resistivity ρ (1) and the Seebeck coefficient α (2) (a) and distribution of the density of electronic states DOS (b) of the basic semiconductor TmNiSb [5]

At the same time, simulation of the electronic structure for the ordered version of the *TmNiSb* crystal structure showed that the Fermi level ε_F lies near the edge of the conduction band ε_C (Fig. 1 *b*), and electrons are the majority carriers. The inconsistency of the experimental and simulation results prompts us to establish the crystal and electronic structure of the *p-TmNiSb* basic semiconductor as close as possible to the real state. In addition, since the atomic radius of *V* (r_V = 0.134 nm) is smaller than *Tm* (r_{Tm} = 0.174 nm) and close to the atomic radius of *Ni* (r_{Ni} = 0.125 nm), the formation of a $Tm_{1-x}V_xNiSb$ substitutional solid solution may be accompanied by unpredictable changes in the crystal and electronic structure. This is precisely the subject of the following study. After all, knowledge of the peculiarities of the dynamics of the crystal and electronic structures of the $Tm_{1-x}V_xNiSb$ semiconductor allows the appropriate doping to generate energy states that will meet the conditions for obtaining the maximum values of the thermoelectric figure of merit *Z* [2], and the process of optimizing properties will be predictable.

Previous studies of the related semiconductor thermoelectric materials based on half-Heusler phases, in particular, $Lu_{1-x}V_xNiSb$ [6], $Lu_{1-x}Zr_xNiSb$ [7] and $Lu_{1-x}Sc_xNiSb$ [8], allowed establishing the disorder and defectiveness of the crystal structure of the basic semiconductor *p-LuNiSb*. It was shown that there are vacancies (V_{ac}) in positions 4*a* of *Lu* atoms and 4*c* of *Ni* atoms (Fig. 2), which generate structural defects of acceptor nature and corresponding acceptor states in the bandgap ε_g of the *p-LuNiSb* semiconductor. The presence of vacancies in the structure of the *LuNiSb* compound fundamentally changes the mechanism of entry of impurity atoms into its crystal structure when optimizing the properties of the thermoelectric material to obtain the maximum values of the thermoelectric figure of merit *Z* ($Z(T)=\alpha^2(T)/\sigma(T)\cdot\kappa(T)$) [2].

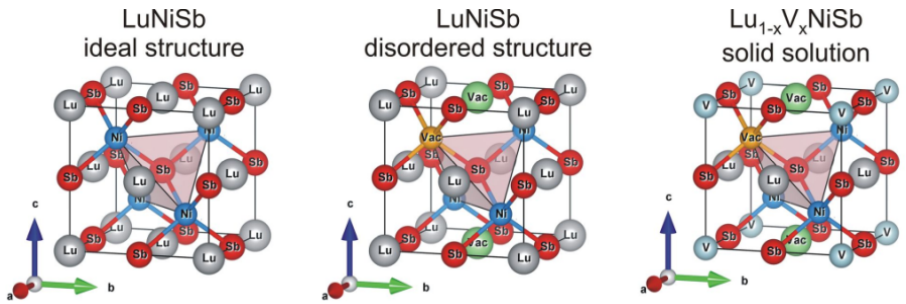

Fig. 2. Models of variants of the crystal structure LuNiSb and $Lu_{1-x}V_xNiSb$

Thus, doping *p-LuNiSb* by atoms with large atomic radii, in particular, *Zr* (r_{Zr} = 0.160 nm) and *Sc* (r_{Sc} = 0.164 nm), by substituting in position 4*a* the rare earth metal atom *Lu* (r_{Lu} = 0.173 nm) did not lead to occupation by doping atoms of other crystallographic positions. Moreover, the substitution of *Lu* ($5d^16s^2$) by *Sc* ($3d^14s^2$) generated in $Lu_{1-x}Sc_xNiSb$ defects of neutral nature (*Lu* and *Sc* are located in the same group of the periodic system of chemical elements)), and in the case of introducing *Zr* ($4d^25s^2$) atoms– defects of donor nature (*Zr* has more *d*-electrons). Simulation of the free energy $\Delta G(x)$ (Helmholtz potential) and mixing enthalpy ΔH_{mix} showed the energetic feasibility of the existence of $Lu_{1-x}Zr_xNiSb$ and $Lu_{1-x}Sc_xNiSb$ solid solutions [7, 8].

When doping *p-LuNiSb* with *V* ($3d^34s^2$) atoms, introduced into the structure by substitution in position 4*a* of *Lu* atoms, *V* atoms simultaneously occupied different crystallographic positions in different ratios [6]. The prerequisite for such changes in the crystal and electronic structures of $Lu_{1-x}V_xNiSb$ was the proximity of the atomic radii of *V* (r_V = 0.134 nm) and *Ni* (r_{Ni} = 0.125 nm), when defects of acceptor and donor nature are generated, and in the bandgap ε_g the respective energy states appear.

The results of the study of the structural, kinetic, and energy properties of the semiconductor solid solution $Tm_{1-x}V_xNiSb$, x = 0 - 0.10, presented below will allow us to understand the nature of the defects of the basic semiconductor *p-TmNiSb*, which will make the process of optimizing the characteristics of the thermoelectric material predictable.

Research methods

The crystal structure, electrokinetic and energy properties of the $Tm_{1-x}V_xNiSb$, x = 0 - 0.1 solid solution were studied. $Tm_{1-x}V_xNiSb$ samples were synthesized by fusing a batch of initial components in an electric arc furnace in an inert argon atmosphere followed by homogenizing annealing for 720 h at a temperature of 1073 K. Arrays of diffraction data were obtained using a STOE STADI P powder diffractometer ($CuK\alpha_1$ radiation). Crystallographic parameters were calculated using the Fullprof program [9]. The chemical and phase compositions of the samples were monitored by a microprobe analyzer (EPMA, energy-dispersive *X*-ray analyzer). We measured the temperature and concentration dependences of the resistivity (ρ) and the Seebeck coefficient (α) relative to the copper of $Tm_{1-x}V_xNiSb$, x = 0 - 0.10 samples, in the temperature range T = 80 - 400 KW.

Research on the structural properties of $Tm_{1-x}V_xNiSb$

X-ray phase and structural analyses of $Tm_{1-x}V_xNiSb$, x = 0 - 0.1 samples showed that the diffractograms of the samples contain no traces of other phases and are indexed in the *MgAgAs* structural type. X-ray structural studies also made it possible to establish the nature of change in the unit cell period $a(x)$ of $Tm_{1-x}V_xNiSb$. Based on the fact that the atomic radius of *Tm* (r_{Tm} = 0.174 nm) is much larger than the atomic radius of *V* (r_V = 0.134 nm), we expected to obtain a decrease in the values of the unit cell period $a(x)$ when *Tm* atoms are replaced by *V* atoms in the position 4*a*. Such substitution should have generated in the crystal structure of $Tm_{1-x}V_xNiSb$ defects of donor nature and their corresponding impurity donor states in the bandgap ε_g of the semiconductor.

However, the results of *X*-ray structural analysis of $Tm_{1-x}V_xNiSb$ solid solution samples do not show, as expected, a monotonous decrease in the values of the unit cell period $\alpha(x)$ (Fig. 3). Thus, in the area of concentrations x = 0 - 0.03, the values of the period $\alpha(x)$ increase, pass through a maximum, and begin to decrease at $x > 0.03$. The non-monotonic change in the values of the fundamental structural parameter of the $Tm_{1-x}V_xNiSb$ solid solution is experimental evidence that *V* atoms introduced into the *TmNiSb* compound not only replace *Tm* atoms in position 4*a*, but also partially occupy other

crystallographic positions. By the way, when studying the related semiconductor solid solution $Lu_{1-x}V_xNiSb$, we obtained a similar behavior of the unit cell period α(x) (Fig. 3, inset) [6]. Studies have shown that in $Lu_{1-x}V_xNiSb$, *V* atoms simultaneously occupy the crystallographic positions 4*a* of *Lu* atoms and 4*c* of *Ni* atoms in different ratios, generating structural defects of acceptor and donor nature.

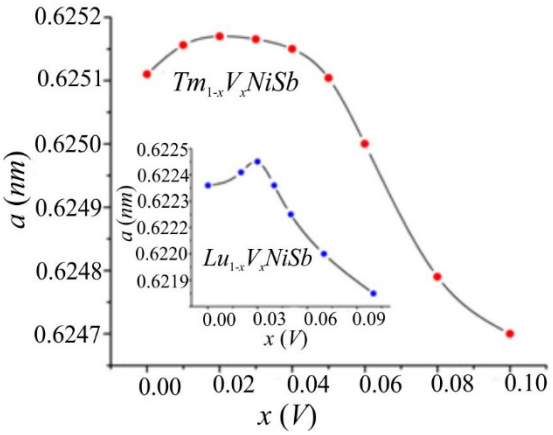

Fig. 3. Change in the values of the unit cell period a(x) of $Tm_{1-x}V_xNiSb$; inset: change in the unit cell period a(x) of $Lu_{1-x}V_xNiSb$ [6]

Based on geometric considerations, we can assume that the increase in the unit cell period $a(x)$ in the area of concentrations x = 0 - 0.03 $Tm_{1-x}V_xNiSb$ could simultaneously be caused by two processes:

a) occupation by *V* atoms of vacancies (V_{ac}) in the crystallographic position 4*a*;

b) partial occupation by *V* atoms of the 4*c* position of *Ni* atoms, since the atomic radius *V* (r_V = 0.134 nm) is greater than the atomic radius of *Ni* (r_{Ni} = 0.125 nm).

In this case, the following processes will occur in the electronic structure of the $Tm_{1-x}V_xNiSb$ solid solution at concentrations of x = 0 - 0.03:

a) occupation by *V* atoms of vacancies (V_{ac}) in position 4*a*, which acted as structural defects of the acceptor nature and generated acceptor states, will lead to the simultaneous elimination of defects of acceptor nature and now generates effects of donor nature with the appearance in the bandgap ε_g of the corresponding donor states;

b) occupation by *V* atoms of the 4*c* position of *Ni* atoms generates structural defects of acceptor nature, since *V* ($3d^34s^2$) atom has fewer *d*-electrons than *Ni* ($3d^84s^2$) atom, and corresponding acceptor states are generated in the bandgap.

A decrease in the unit cell period $a(x)$ in the semiconductor solid solution $Tm_{1-x}V_xNiSb$ at concentrations $x > 0.03$ can only cause the replacement of *Tm* atoms (r_{Tm} = 0.174 nm) by *V* atoms (r_V = 0.134 nm) in the crystallographic position 4*a*. In this case, structural defects of donor nature will be generated in the $Tm_{1-x}V_xNiSb$ semiconductor, since *V* ($3d^34s^2$) atoms have more *d*-electrons than *Tm* ($5d^06s^2$) atoms, and corresponding donor states will appear in the bandgap.

Insignificant concentrations of impurity *V* atoms and relatively low accuracy of *X*-ray structural studies did not allow establishing the fact of ordering the crystal structure of the semiconductor. Therefore, we are aware that the results of structural studies do not fully reflect possible transformations in the structure of $Tm_{1-x}V_xNiSb$. Therefore, the above considerations regarding changes in the crystal structure based on the behavior of the unit cell period $a(x)$ of $Tm_{1-x}V_xNiSb$ are of an evaluative nature. The following results of studying the kinetic and energy properties of $Tm_{1-x}V_xNiSb$ will make it possible to clarify conclusions about possible changes in the structure of the thermoelectric material. On this basis, it will be possible in the future to model crystal and electronic structures as close as possible to

the real state of matter, which will be the basis for optimizing the kinetic properties of the thermoelectric material by choosing doping conditions.

Research on the electrokinetic and energy properties of $Tm_{1-x}V_xNiSb$

The temperature and concentration dependences of the resistivity ρ and the Seebeck coefficient α for the samples $Tm_{1-x}V_xNiSb$, $x = 0.02 - 0.10$, are given in Figs. 4 - 6. The dependences $\ln(\rho(1/T))$ and $\alpha(1/T)$ for $Tm_{1-x}V_xNiSb$, $x = 0 - 0.10$ are typical for doped and compensated semiconductors with high- and low-temperature activation regions, which indicates the presence of several mechanisms of electrical conductivity. The dependences $\ln(\rho(1/T))$ for $Tm_{1-x}V_xNiSb$, $x = 0 - 0.10$ samples are described using a well-known relation (1) [10, 11]:

$$\rho^{-1}(T) = \rho_1^{-1} \exp\left(-\frac{\varepsilon_1^{\rho}}{k_B T}\right) + \rho_3^{-1} \exp\left(-\frac{\varepsilon_3^{\rho}}{k_B T}\right), \quad (1)$$

where the first term describes the activation of current carriers ε_1^{ρ} from the Fermi level ε_F into the zone of continuous energies, and the second, low-temperature, hopping conduction through the impurity states ε_3^{ρ} with energies close to the Fermi energy ε_F. Calculations showed that in the basic semiconductor *p-TmNiSb* the Fermi level ε_F is located at a distance of $\varepsilon_1^{\rho} = 53.4$ *meV* from the ceiling of the valence band ε_V. This result coincides with the one obtained earlier [5].

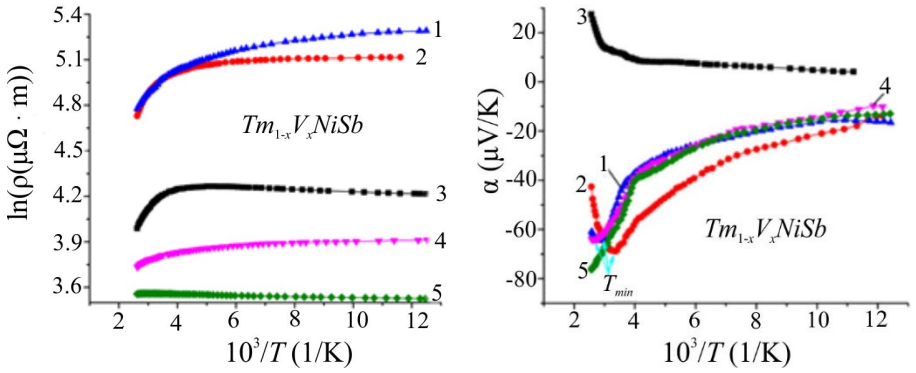

*Fig. 4. Temperature dependences of resistivity ln(ρ(1/Tx)) (**a**) and the Seebeck coefficient α(1/T,x) (b) of $Tm_{1-x}V_xNiSb$: 1 – x=0.05; 2 – x=0.03; 3 – x=0.02; 4 – x=0.08; 5 – x=0.10*

From the activation sections of the dependences of the Sebeck coefficient $\alpha(1/T)$ of $Tm_{1-x}V_xNiSb$ (Fig. 4*b*), which are described by expression (2) [12], the values of the activation energies ε_1^{α} and ε_3^{α}, were calculated, which give, respectively, the values of the modulation amplitude of continuous energy zones and small-scale fluctuations of a heavily doped and compensated semiconductor [10]:

$$\alpha = \frac{k_B}{e}\left(\frac{\varepsilon_i^{\alpha}}{k_B T} - \gamma + 1\right), \quad (2)$$

where γ is a parameter that depends on the nature of scattering mechanism.

Doping *p-TmNiSb* with the lowest in the experiment concentration of *V* atoms by substituting *Tm* atoms in the 4*a* position at concentrations $x = 0 - 0.02$ is accompanied by a decrease in the value of the electrical resistivity $\rho(x, T)$ for all investigated temperatures, for instance, at $T = 80$ K from

$\rho_{x=0}$ = 91.1 μOhm·m to $\rho_{x=0.02}$ = 67.7 μOhm·m. In doing so, the values of the Seebeck coefficient $\alpha(x, T)$ at these concentrations and the studied temperatures remain positive, pointing to the location of the Fermi level ε_F in the bandgap ε_g near the valence band ε_V (Figs. 5, 6).

A decrease in the values of the electrical resistivity $\rho(x, T)$ of $Tm_{1-x}V_xNiSb$ at concentrations x = 0 - 0.02 in the hole-type semiconductor is possible only in the case of increasing the concentration of free holes during the ionization of acceptors. Incidentally, we recall that in this area of concentrations there was an increase in the values of the unit cell period $a(x)$ (Fig. 3), and this is possible only if the V atoms occupy the 4c position of the Ni atoms. Since the V ($3d^3 4s^2$) atom has fewer d-electrons than the Ni ($3d^8 4s^2$) atom, this substitution generates structural defects of an acceptor nature, and corresponding acceptor states appear in the bandgap. It is their contribution that is decisive in reducing the values of the resistivity $\rho(x, T)$ of $Tm_{1-x}V_xNiSb$ at x = 0 - 0.02.

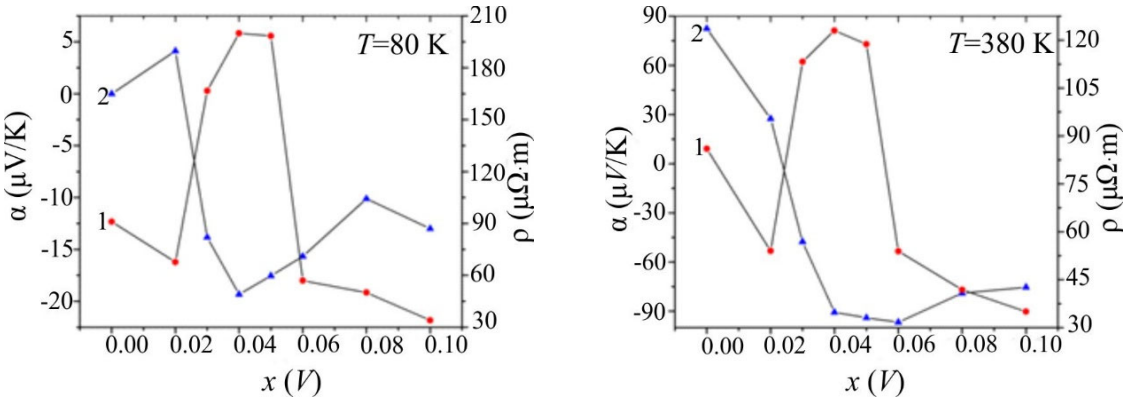

Fig. 5. Change in the values of the electrical resistivity ρ(x,T) and the Seebeck coefficient α(x,T) of $Tm_{1-x}V_xNiSb$ at different temperatures

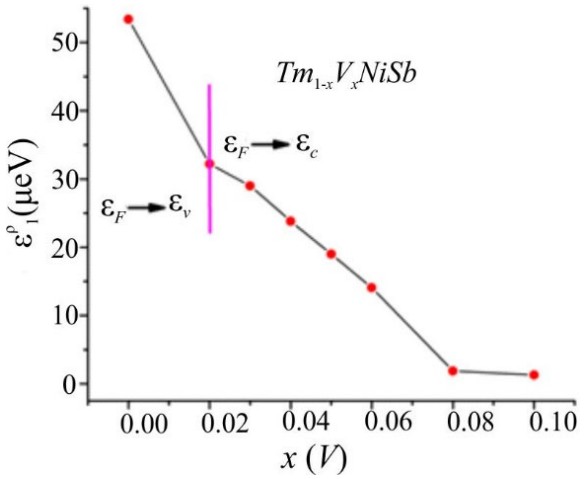

Fig. 6. Change in the values of activation energy $\varepsilon_1^{\rho}(x)$ of $Tm_{1-x}V_xNiSb$

Analysis of the behaviour of the Fermi level ε_F in the area of concentrations x = 0 - 0.02 also indicates an increase in the concentration of acceptor states in $Tm_{1-x}V_xNiSb$ (Fig. 6). If in p-$TmNiSb$ the Fermi level ε_F is located at a distance of ε_F = 53.4 meV from the ceiling of the valence band ε_V, then in $Tm_{0.98}V_{0.02}NiSb$ it has approached the valence band at a distance of ε_F = 32.2 meV. And this is possible in a p-type semiconductor only if the concentration of acceptor states increases. At higher concentrations of V atoms in the region $0.02 < x \leq 0.04$, the values of the resistivity $\rho(x, T)$ $Tm_{1-x}V_xNiSb$ increase, for

example, at T = 80 K from $\rho_{x=0.02}$ = 67.7 μΩ·m to $\rho_{x=0.04}$ = 200.3 μΩ·m. At a concentration of $x \approx 0.03$, the sign of the Seebeck coefficient α(x, T) changes from positive to negative, and electrons become the majority carriers. An increase in the values of electrical resistivity ρ(x, T) in the concentration range $0.02 < x \leq 0.04$ and a change in the sign of the Seebeck coefficient α(x, T) is evidence of the appearance in the semiconductor of a powerful source of free electrons, which are carried away by acceptors, which leads to a decrease in the concentration of holes.

In the semiconductor $Tm_{0.97}V_{0.03}NiSb$, the concentrations of ionized acceptor and donor states are close, but there are more donors. At higher concentrations, electrons become the majority carriers in $Tm_{1-x}V_xNiSb$. We associate the decrease in the values of electrical resistivity ρ(x, T) and the negative values of the Seebeck coefficient $\alpha(x, T)$ of $Tm_{1-x}V_xNiSb$ at concentrations $0.04 < x$ (Fig. 5) with an increase in the concentration of free electrons. The results of structural studies allow us to establish their origin. Thus, at concentrations of $0.03 < x$, there is a decrease in the unit cell period $\alpha(x)$ of $Tm_{1-x}V_xNiSb$ (Fig. 3). And this is possible only when Tm atoms ((r_{Tm} = 0.174 nmм) nm) are replaced by V atoms (r_V = 0.134 nm) in crystallographic position 4α. Given that V atoms $3d^34s^2$) have more d-electrons than Tm atoms ($5d^06s^2$), defects of donor nature appear in $Tm_{1-x}V_xNiSb$, and corresponding donor states appear in the bandgap.

In addition, an increase in the concentration of donor states is accompanied by a drift of the Fermi level ε_F to the conduction band ε_C almost linearly (Fig. 6). Thus, if in $Tm_{0.96}V_{0.04}NiSb$ the Fermi level ε_F lay at a distance of ε_F = 24.1 meV from the bottom of the conduction band ε_C,, then in the semiconductors $Tm_{0.94}V_{0.06}NiSb$ and $Tm_{0.90}V_{0.10}NiSb$ the depth of the Fermi level ε_F is ε_F = 14.1 meV and ε_F = 1.3 meV, respectively.

In this context, it seems logical to ask why the Fermi level ε_F at colossal concentrations of V atoms generating donors remains in the band gap ε_g of $Tm_{1-x}V_xNiSb$ and does not enter the conduction band ε_C? After all, donor states are generated in $Tm_{1-x}V_xNiSb$ at these concentrations. In other words, what structural changes of $Tm_{1-x}V_xNiSb$ could cause such a significant impact on the electronic system of the semiconductor that the dielectric-metal conduction transition, which is the Anderson transition [12], did not occur?

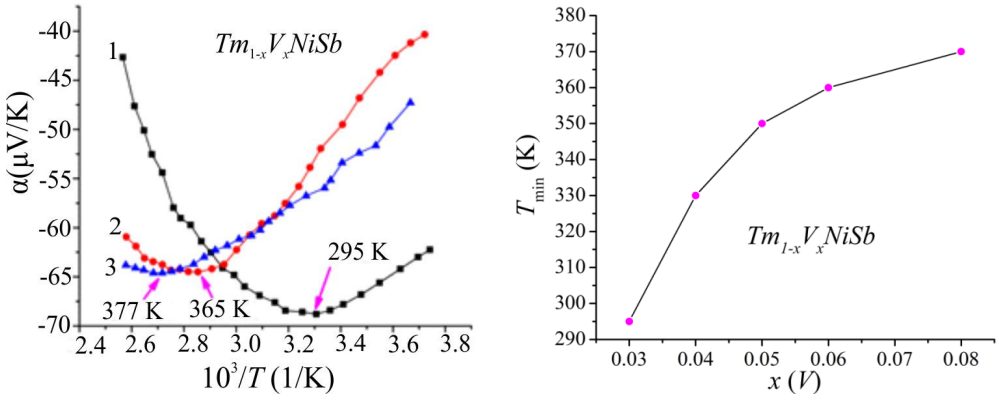

*Fig. 7. Change in the values of the Seebeck coefficient α(1/T,x): 1 – x=0.03; 2 – x=0.05; 3 – x=0.08 (**a**) and T_{min} on the dependence α((1/T,x) (b) $Tm_{1-x}V_xNiSb$*

The answer to this question is partially provided by the analysis of the behaviour of the temperature dependences of the Seebeck coefficient α(1/T, x) of $Tm_{1-x}V_xNiSb$ (Fig 4*b* and 7). Fig. 7*a* in an enlarged format shows fragments of the temperature dependences of the Seebeck coefficient α(1/T) of $Tm_{1-x}V_xNiSb$ (Fig, 4*b*) for three concentrations of V atoms: x = 0.03, x = 0.05 and x = 0.08. We recall that at all investigated temperatures the sign of the Seebeck coefficient α(1/T, x) remained positive at

concentrations of $x = 0$ - 0.02. In the semiconductor $Tm_{0.97}V_{0.03}NiSb$ the sign of the Seebeck coefficient $\alpha(1/T, x)$ is already negative but the behaviour of the dependence $\alpha(1/T, x)$ turned out to be non-monotonic (Fig. 7*a*). We can see that at a temperature of $T_{min} \approx 295$ K, the dependence passes through a minimum, and as the temperature increases, the values of the Seebeck coefficient decrease rapidly, and the dependence itself changes with a tendency to a possible change of sign at higher temperatures, which we did not reach in the experiment. This minimum on the dependence $\alpha(1/T, x)$ of $Tm_{0.97}V_{0.03}NiSb$ at the temperature $T_{min} \approx 295$ K indicates the presence of acceptor states of unknown origin in the semiconductor of the electronic conductivity type, the contribution of which to the conductivity increases with a rise in temperature. The temperature dependences of the Seebeck coefficient $\alpha(1/T, x)$ of semiconductors $Tm_{0.95}V_{0.05}NiSb$ and $Tm_{0.92}V_{0.08}NiSb$ also have minima at temperatures $T_{min} \approx 365$ K and $T_{min} \approx 377$ K, respectively. However, at the highest *V* concentration, there is no such minimum on the temperature dependence $\alpha(1/T, x)$ of the $Tm_{0.90}V_{0.10}NiSb$ semiconductor, hence the influence of acceptor states on the behaviour of the Seebeck coefficient at the studied temperatures was not revealed. Fig. 7*b* shows the experimentally determined dependence of temperature minima (T_{min}) on the dependence of the Seebeck coefficient $\alpha(1/T, x)$ on the concentration of impurity *V* atoms in $Tm_{1-x}V_xNiSb$. We can see that the higher the concentration of *V* atoms, the higher the temperature at which a minimum appears on the dependence of the Seebeck coefficient $\alpha(1/T, x)$.

Since the Seebeck coefficient by its nature is sensitive to a change in the ratio of current carriers of different signs, the change in the behavior of the Seebeck coefficient $\alpha(1/T, x)$ in the semiconductor now of the electronic conductivity type $Tm_{1-x}V_xNiSb$, $0.03 < x$, is manifestation of the influence of acceptor states of unknown nature on its electronic structure.

It turns out that the acceptor states that appear in $Tm_{1-x}V_xNiSb$ at high temperatures have a different depth and origin than the acceptor states caused by vacancies in the 4*a* position of *Tm* atoms. We can assume, as in the case of the related solid solution $Lu_{1-x}V_xNiSb$ [6], that in $Tm_{1-x}V_xNiSb$, the *V* ($3d^3 4s^2$) atoms simultaneously in different proportions occupy both position 4*a* (vacancies and replace *Tm* atoms), and replace in position 4*c* the atoms of *Ni* ($3d^8 4s^2$), generating structural defects of donor and acceptor nature and the respective energy states. At the same time, a question may arise regarding the correlation of such a conclusion with a change in the unit cell period which should increase when the *Ni* atoms ($r_{Ni} = 0.125$ nm) are replaced by *V* ($r_V = 0.134$ nm). We analyze the range of concentrations by which both the unit cell period *a* (*x*) of $Tm_{1-x}V_xNiSb$ (Fig. 3), and the value of electrical resistivity $\rho(x, T)$ decrease (Fig 5).

In this context, it is important to understand that the unit cell period $\alpha(x)$ of $Tm_{1-x}V_xNiSb$ is an integral parameter, reflecting changes in the semiconductor structure. Thus, the atomic radius of *Tm* is much larger than the atomic radius of *V*, and their ratio is $r_{Tm}/r_V = 1.30$. In turn, the atomic radius of *V* is slightly larger than the atomic radius of *Ni,* and their ratio is equal to $r_V/r_{Ni} = 1.07$. Therefore, the contribution to the change in the unit cell period $\alpha(x)$ of $Tm_{1-x}V_xNiSb$ from structural changes in position 4*a* of *Tm* atoms is decisive. Even under the hypothetical condition of the same distribution of impurity *V* atoms in positions 4*a* and 4*c* the values of the unit cell period *a* (*x*) of $Tm_{1-x}V_xNiSb$ will decrease.

The final establishment of the nature of the detected anomalies in the behavior of the Seebeck coefficient $\alpha(1/T, x)$ of $Tm_{1-x}V_xNiSb$ requires additional research, in particular, modeling the behavior of the Fermi level ε_F under different variants of the spatial arrangement of atoms in the array of the basic semiconductor *p-TmNiSb* and their comparison with experimental the results of this work. This will make it possible to establish the peculiarities of the crystal and electronic structure of *p-TmNiSb*, since they determine the way impurity atoms enter the array of the semiconductor, which determines the formation of structural defects of various nature and the appearance of the corresponding energy states in the bandgap ε_g. However, this is the task of another study.

Conclusions

According to the results of a comprehensive study of the structural, kinetic, and energy properties of the $Tm_{1-x}V_xNiSb$ semiconductor solid solution obtained by introducing *V* atoms into the *p-TmNiSb* structure by substituting *Tm* atoms in the crystallographic position 4*a*, a complex nature of structural changes was revealed. It is shown that *V* atoms can simultaneously occupy different crystallographic positions in different ratios, generating structural defects of acceptor and donor nature. This gives rise to the corresponding acceptor and donor states in the bandgap ε_g of $Tm_{1-x}V_xNiSb$. The mechanism of formation of two types of acceptor states with different depth of occurrence in $Tm_{1-x}V_xNiSb$*:* shallow acceptor states generated by vacancies in the structure of the half-Heusler phase *TmNiSb* and deep acceptor states formed by defects when *Ni* atoms are replaced by *V* in the 4*c* position. The ratio of the concentrations of generated defects determines the position of the Fermi level ε_F and the conduction mechanisms. The investigated $Tm_{1-x}V_xNiSb$ solid solution is a promising thermoelectric material.

References

1. Romaka V. A., Stadnyk Yu. V., Krayovskyy V. Ya., Romaka L. P., Guk O. P., Romaka V. V., Mykyuchuk M. M., Horyn A. M. (2020). *Novitni termochutlyvi materialy ta peretvoriuvachi temperatury* [*New thermosensitive materials and temperature converters*]. Lviv, Lvivska Polytechnika [in Ukrainian].
2. Anatychuk L. I. (1979). *Termoelementy i termoelectricheskiie ustroistva. Spravochnik.* [*Thermoelements and thermoelectric devices*. *Reference book*]. Kyiv: Naukova dumka [in Russian].
3. Hartjes K., Jeitschko W. (1995). Crystal structure and magnetic properties of the lanthanoid nickel antimonides *LnNiSb* (*Ln = La–Nd*, *Sm*, *Gd–Tm*, *Lu*). *Journal of Alloys and Compounds*, 226, 81 – 86. DOI: https://doi.org/10.1016/0925-8388(95)01573-6.
4. Karla I., Pierre J., Skolozdra R. V. (1998). Physical properties and giant magnetoresistance in *RNiSb* compounds. *Journal of Alloys and Compounds*, 265, 42 - 48. DOI: https://doi.org/10.1016/S0925-8388(97)00419-2.
5. Romaka V.V., Romaka L., Horyn A., Stadnyk Yu. (2021). Experimental and theoretical investigation of the *Y-Ni-Sb* and *Tm-Ni-Sb* systems. *Journal of Alloys and Compounds*, 855, 157334 – 12. DOI: https://doi.org/10.1016/j.jallcom.2020.157334.
6. Romaka V. V., Romaka V. A., Stadnyk Yu. V., Romaka L. P., Plevachuk Y. O., Pashkevich V. Z., Haraniuk P. I. Horyn A. (2023). Features of the generation of the energy states in the semiconductor $Lu_{1-x}V_xNiSb$. *Ukr. J. Phys*., 68 (№ 4), 274 – 283. DOI: https://doi.org/10.15407/ujpe68.4.274.
7. Romaka V. A., Stadnyk Yu., Romaka L., Horyn A., Pashkevich V., Nychyporuk H., Garanyuk P. (2022). Investigation of Thermoelectric Material Based on $Lu_{1-x}Zr_xNiSb$ Solid Solution. I. Experimental Results. *J. Phys. and Chem. Sol. State*, 23, 235–241. DOI: 10.15330/pcss.23.2.235-241.
8. Romaka V. V., Romaka V. A., Stadnyk Yu. V., Romaka L. P., Demchenko P. Yu., Pashkevich V. Z., Horyn A. M. (2022). Features of mechanisms of electrical conductivity in semiconductive solid solution $Lu_{1-x}Sc_xNiSb$. *Ukr. J. Phys*., 67 (№ 5), 370–379. DOI: https://doi.org/10.15407/ujpe67.5.370.
9. Roisnel T., Rodriguez-Carvajal J. (2001). WinPLOTR: a windows tool for powder diffraction patterns analysis. *Mater. Sci. Forum*, Proc. EPDIC7 378 – 381, 118 – 123. DOI: https://doi.org/10.4028/www.scientific.net/MSF.378-381.118.

10. Shklovskii B. I. and Efros A. L. (1984). *Electronic properties of doped semiconductors* NY: Springer; (1979) Moscow: Nauka. DOI: https://doi.org/10.1002/crat.19720070420.
11. Babak V. P., Babak S. V., Myslovych M. V., Zaporozhets A. O., Zvaritch V. M. (2020). Technical provision of diagnostic systems. *Studies in Systems, Decision and Control*, 281, 91 – 133. DOI: https://doi.org/10.1007/978-3-030-44443-3_4.
12. Mott N. F., Davis E. A. (1979). *Electron processes in non-crystalline materials.* Oxford: Clarendon Press. DOI: 10.1007/978-3-662-02403-4.

Submitted: 26.01.2023

Ромака В. А., *док. тех. наук, канд. фіз.-мат. наук, професор*[1]
Стадник Ю. В, *канд. хім. наук*[2]
Ромака Л. П., *канд. хім. наук*[2]
Демченко П. Ю.[2]**,**
Горинь А. М., *канд. хім. наук*[2]
Луковський Т. І.[1]

[1]Національний університет "Львівська політехніка", вул. С. Бандери, 12, Львів, 79013, Україна; *e-mail: vromaka@polynet.lviv.ua*
[2]Львівський національний університет ім. І. Франка, вул. Кирила і Мефодія, 6, Львів, 79005, Україна; *e-mail: lyubov.romaka@lnu.edu.ua*

ЕКСПЕРИМЕНТАЛЬНІ ДОСЛІДЖЕННЯ ВЛАСТИВОСТЕЙ НОВОГО ТЕРМОЕЛЕКТРИЧНОГО МАТЕРІАЛУ $Tm_{1-x}V_xNiSb$

Досліджено структурні, кінетичні та енергетичні властивості термоелектричного матеріалу $Tm_{1-x}V_xNiSb$ у діапазонах: T = 80 – 400 K, x = 0 – 0.10. Показано, що атоми V можуть одночасно у різних співвідношеннях займати різні кристалографічні позиції, генеруючи дефекти акцепторної та донорної природи. Це породжує у забороненій зоні ε_g $Tm_{1-x}V_xNiSb$ відповідні акцепторні та донорні стани. Встановлено механізм формування у $Tm_{1-x}V_xNiSb$ двох сортів акцепторних станів з різною глибиною залягання: дрібні акцептори, породжена вакансіями у структурі фази пів-Гейслера TmNiSb, та глибокі акцептори, утворені дефектами при заміщенні у позиції 4c атомів Ni на V. Співвідношення концентрацій генерованих дефектів визначає положення рівня Фермі ε_F та механізми провідності. Досліджений твердий розчин $Tm_{1-x}V_xNiSb$ є перспективним термоелектричним матеріалом. Бібл. 12, рис. 7.

Ключові слова: *електронна структура, електроопір, коефіцієнт термоЕРС.*

References

1. Romaka V. A., Stadnyk Yu. V., Krayovskyy V. Ya., Romaka L. P., Guk O. P., Romaka V. V., Mykyuchuk M. M., Horyn A. M. (2020). *Novitni termochutlyvi materialy ta peretvoriuvachi*

temperatury [*New thermosensitive materials and temperature converters*]. Lviv, Lvivska Polytechnika [in Ukrainian].

2. Anatychuk L. I. (1979). *Termoelementy i termoelectricheskiie ustroistva. Spravochnik.* [*Thermoelements and thermoelectric devices*. *Reference book*]. Kyiv: Naukova dumka [in Russian].
3. Hartjes K., Jeitschko W. (1995). Crystal structure and magnetic properties of the lanthanoid nickel antimonides *LnNiSb* (*Ln = La–Nd*, *Sm*, *Gd–Tm*, *Lu*). *Journal of Alloys and Compounds*, 226, 81 - 86. DOI: https://doi.org/10.1016/0925-8388(95)01573-6.
4. Karla I., Pierre J., Skolozdra R. V. (1998). Physical properties and giant magnetoresistance in *RNiSb* compounds. *Journal of Alloys and Compounds*, 265, 42 - 48. DOI: https://doi.org/10.1016/S0925-8388(97)00419-2.
5. Romaka V.V., Romaka L., Horyn A., Stadnyk Yu. (2021). Experimental and theoretical investigation of the *Y-Ni-Sb* and *Tm-Ni-Sb* systems. *Journal of Alloys and Compounds*, 855, 157334 – 12. DOI: https://doi.org/10.1016/j.jallcom.2020.157334.
6. Romaka V. V., Romaka V. A., Stadnyk Yu. V., Romaka L. P., Plevachuk Y. O., Pashkevich V. Z., Haraniuk P. I. Horyn A. (2023). Features of the generation of the energy states in the semiconductor $Lu_{1-x}V_xNiSb$. *Ukr. J. Phys*., 68 (№ 4), 274 – 283. DOI: https://doi.org/10.15407/ujpe68.4.274.
7. Romaka V. A., Stadnyk Yu., Romaka L., Horyn A., Pashkevich V., Nychyporuk H., Garanyuk P. (2022). Investigation of Thermoelectric Material Based on $Lu_{1-x}Zr_xNiSb$ Solid Solution. I. Experimental Results. *J. Phys. and Chem. Sol. State*, 23, 235–241. DOI: 10.15330/pcss.23.2.235-241.
8. Romaka V. V., Romaka V. A., Stadnyk Yu. V., Romaka L. P., Demchenko P. Yu., Pashkevich V. Z., Horyn A. M. (2022). Features of mechanisms of electrical conductivity in semiconductive solid solution $Lu_{1-x}Sc_xNiSb$. *Ukr. J. Phys*., 67 (№ 5), 370 – 379. DOI: https://doi.org/10.15407/ujpe67.5.370.
9. Roisnel T., Rodriguez-Carvajal J. (2001). WinPLOTR: a windows tool for powder diffraction patterns analysis. *Mater. Sci. Forum*, Proc. EPDIC7 378 - 381, 118 – 123. DOI: https://doi.org/10.4028/www.scientific.net/MSF.378-381.118.
10. Shklovskii B. I. and Efros A. L. (1984). *Electronic properties of doped semiconductors* NY: Springer; (1979) Moscow: Nauka. DOI: https://doi.org/10.1002/crat.19720070420.
11. Babak V. P., Babak S. V., Myslovych M. V., Zaporozhets A. O., Zvaritch V. M. (2020). Technical provision of diagnostic systems. *Studies in Systems, Decision and Control*, 281, 91 – 133. DOI: https://doi.org/10.1007/978-3-030-44443-3_4.
12. Mott N. F., Davis E. A. (1979). *Electron processes in non-crystalline materials.* Oxford: Clarendon Press. DOI: 10.1007/978-3-662-02403-4.

Submitted: 26.01.2023

M.M. Korop

M. M. Korop

Institute of Thermoelectricity of the NAS and MES of Ukraine,
1, Nauky str., Chernivtsi, 58029, Ukraine,
e-mail: mykola.korop@chnu.edu.ua

MACHINE LEARNING IN THERMOELECTRIC MATERIALS SCIENCE

The paper presents machine learning methods and their application in thermoelectric materials science. The results of their application, strong points and application areas are shown. The difficulties that arise in the process of predicting the properties of thermoelectric materials and ways to overcome them were taken into account. Bibl. 30, Fig. 1, Tabl. 2.
Key words: machine learning methods, thermoelectric materials science.

Introduction

General characterization of the problem. Machine learning plays an increasingly important role in the intensification of scientific research and discoveries. New approaches and methods open up the possibility of speeding up the discovery of new promising materials [1 – 3], optimization of device manufacturing technologies [4, 5], calculation of the most economically advantageous solutions under given conditions [6].

As noted in article [7], the property of thermoelectricity is its use in areas that shape scientific and technological progress, therefore it is developing primarily in the leading countries of the world. Thermoelectric materials have great potential; today they serve as the basis for generating, cooling and sensor devices and sensors, which have found application in all spheres of life from medicine to space. However, the selection of the optimal thermoelectric material for given conditions, its search or optimization is not a trivial task, requiring significant time and material costs.

There are a number of studies on the use of machine learning in thermoelectric materials science; they show high efficiency and low cost of use compared to traditional approaches.

The purpose of the work is to consider machine learning methods and highlight the results of their application in thermoelectric materials science.

Supervised machine learning methods in thermoelectric materials science

Machine learning is a field of scientific research that studies the ability of a computer to learn without being pre-programmed [7]. Machine learning algorithms can be divided into two groups: supervised and unsupervised. Each of these groups has its own scope and the algorithm that can give the most accurate result under the given conditions is chosen.

Supervised machine learning is the construction of algorithms capable of finding general patterns and hypotheses using externally obtained training and test data sets. Such an algorithm studies certain patterns in the training data set for further verification on test data sets [8].

Unsupervised machine learning – recognition of patterns and sets of similarities without the involvement of target attributes, all variables that are present in the training data set participate in the analysis, owing to which such algorithms become useful for clustering and associative segmentation [9].

Machine learning models rely on three key components: training data, descriptors, and an algorithm. Training data are sets of examples from which the algorithm tries to obtain chemical trends, descriptors are low-level characteristics of materials (crystal structure, chemical formula, average atomic number, etc.), which allows to "vectorize" a chemical material and make it suitable for further machine learning. learning algorithm – polls training vector data in combination with a certain template [10].

Kamal Choudhary et al. [11] in their work on the search for highly efficient 3D and 2D dimensional thermoelectric materials use supervised learning algorithms, namely: decision trees, random forest of decision trees, k nearest neighbors, multilayer perceptron and gradient amplification techniques.

A decision tree is a popular machine learning algorithm when the task is to classify a data set or perform regression, this solution effectively copes with missing values and possible errors in the data set [12]. A graphical representation can be represented as a tree, where the nodes represent the validation of conditions for the data and the branches represent the possible outcomes of those conditions. Data for use in this method are partitioned into subsets based on entropy, Gini coefficient, etc. In the article by Alrebdi et al. [13], this method is used to predict the thermal conductivity of thermoelectric materials based on Bi_2Te_3. Decision trees are often used as the basis for ensemble methods, such as a random forest of decision trees.

The main idea of the random forest ensemble method is to create subsets of training data and train individual decision trees for further averaging of predictions (regression task) or combination (classification task). This approach makes it possible to obtain much higher accuracy of forecasts. The advantages of this algorithm include the evaluation of data structure and dependencies for data analysis, and the disadvantages include a relatively slow learning speed due to the need to create and train a large number of individual trees. In the work of Chen et al. [14] the random forest method is used to discover new M2X3 thermoelectric materials with only composition information.

Gradient amplification is used for the composition of weak models (decision trees), gradient descent is used, which allows minimizing the loss functional. Increasing the accuracy of predictions is achieved by adding new models that correct the errors of previous models. This method is widely used and is included in well-known libraries such as XGBoost, LightGBM, CAT Boost. Sheng et al. [15] used this algorithm to predict the power factor in diamond-like thermoelectric materials.

K-nearest neighbors is one of the simplest supervised machine learning algorithms, which is based on the classification of a new object given the classes of *K* nearest neighbors. For example, the Euclidean distance can be used to determine the nearest neighbor. This can lead to slow learning of the algorithm on large data sets due to the need to calculate the distance between all pairs of objects. Gyoung et al. [16] use *K*-nearest-neighbor regression to predict the target value for the input data by interpolating the *K*-nearest-neighbor target values in the training data.

The multilayer perceptron belongs to more advanced machine learning algorithms. It is a neural network consisting of three or more layers, each of which contains several neurons. The algorithm uses backpropagation of error for training, which allows to optimize the weights of the neural network using gradient descent. Thus, each neuron, receiving input data, calculates their internal sum and applies some activation function: sigmoid, hyperbolic tangent, etc., adding nonlinearity to the value of the neuron. Uysal et al. [17] use a multilayer perceptron algorithm to estimate the Seebeck coefficient for a p-type

high-temperature thermoelectric material. This algorithm can serve as a basis for more complex neural networks of the convolutional neural network type.

Unsupervised machine learning methods in thermoelectric materials science

Unsupervised machine learning algorithms are effective when working with datasets that do not contain labels, allowing for hidden structures to be found. Thus, there is an opportunity to carry out clustering to group materials based on their chemical, mechanical or physical properties, identifying their new classes or properties that are common to a certain group. They are also used in the search for anomalies and defects due to the search for deviations from standard values. One of the main applications is the automatic search for combinations of elements or parameters to obtain optimal materials under given conditions or to carry out their optimization. Jia et al. [18] use *K*-means, Gaussian mixture, DBSCAN, AGNES, Birch to search for promising semi-Heusler thermoelectric materials, and Iwasaki et al. [19] use the LASSO algorithm (Method of Minimization of Absolute Compression and Operator Selection) to identify modern materials based on spin-thermoelectric material.

K-means works by dividing the data set into clusters (groups) and aims to minimize variability within clusters and maximize between them. *K* determines the number of clusters specified by the user. The algorithm uses K arbitrary centroids and places the data record in the closest one. After completing the placement of objects, the centroids calculate their average value in the cluster, this process happens iteratively until the centroids stabilize and equilibrium occurs. Sheng et al. [20] use this method to accelerate the discovery of *Cu-Sn-S* thermoelectric compounds using high-throughput synthesis.

The combination of Gaussian divisions is a statistical model and represents a Gaussian sum, where the skin component contains the mean, dispersion and value. This algorithm is often used to generate elliptic shapes in data clusters. To set the parameters, the method of maximizing likelihood through the EM algorithm (Expectation-Maximization) is used. Shimizu et al. [21] use this method for gate analysis of several target parameters in materials design.

DBSCAN, AGNES and Birch are clustering algorithms used to measure the distance or similarity between data points, their main goal is to detect natural groups in data without the need to explicitly specify the number of clusters.

DBSCAN (Density-Based Spatial Clustering of Applications) works by identifying clusters based on large density variance.

AGNES (Agglomerative Nesting) – gradual unification of objects into hierarchical clusters and visualization using a dendrogram.

Birch – the algorithm is optimized for clustering large data sets, allowing them to be processed quickly.

These methods are often employed to discover new groups of promising materials and are used in a number of works [18, 22].

The LASSO regression method works by L_1 regularization, reducing the coefficients of some variables to zero, which facilitates feature selection and helps to highlight the most important features from a large set of features. One drawback follows from this - with signs that are strongly correlated, only one can be taken into account.

When searching for and optimizing a thermoelectric material, the efficiency of the material can be affected by electrical conductivity, thermal conductivity, the Seebeck coefficient, and other parameters. Using this method, you can determine the set that will give the most accurate result. Also,

it provides an opportunity to understand how changing conditions (temperature, pressure, etc.) will affect their properties and to understand the mechanisms of this influence. Wudil et al. [23] use this method to evaluate the performance of materials based on Bi_2Te_3.

Results of the application of machine learning in thermoelectric materials science

In the paper by Gaultois et al. [10] published in 2015, the authors were among the first to develop an electronic system for evaluating the parameters of thermoelectric alloys in real time based on machine learning. In the illustration presented by them it is clear that the best studied thermoelectric materials lie in a certain region of the periodic table (black and blue dots), chalcogenides and p-elements, while orange dots highlight new material alloys proposed by the system based on machine learning and these materials are placed outside the known materials (pure intermetallics).

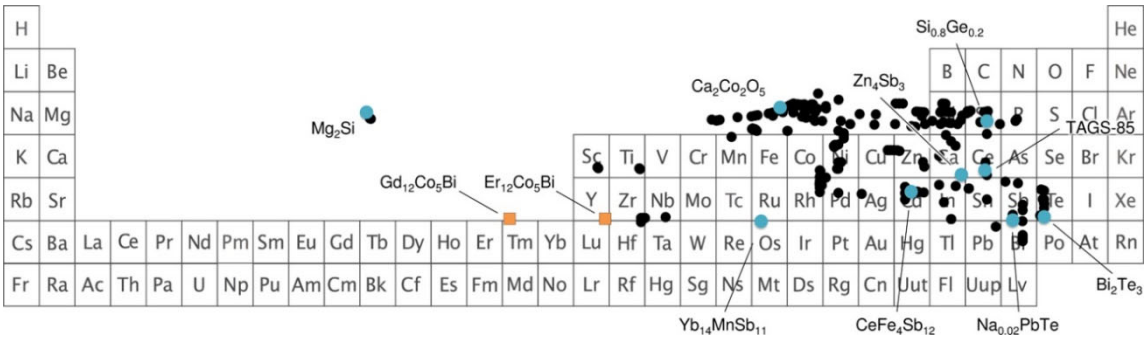

Fig. 1. The periodic table of elements based on the composition-weighted average of the positions of the elements in the material [10]

The authors of this paper have developed a machine model that provides recommendations on the suitability of new thermoelectric alloys for further research, but such a model does not return quantitative predictions of thermoelectric properties or accurate identification of thermoelectric alloys. Such a machine learning-based recommendation system looks for empirical, chemical patterns in experimental data on known thermoelectric materials in order to make statistical predictions about the performance of new materials. When checking the obtained results, the system provided results with high accuracy, where the error distribution for various material properties approaches 0. As a result, several interesting thermoelectric alloys were found selected from the list proposed by the algorithm and experimental confirmation of thermoelectric properties [23 – 25] (Table 1).

Table 1

Several promising new thermoelectric compounds selected from the calculated list. P values refer to the model´s level of confidence that a given material will exhibit room temperature values of a certain property (for instance, S or ρ) within target values [10]

Material	P_S	P_ρ	P_κ	P_{gap}	Comments
$TaPO_5$ and $TaVO_5$	0.894	0.793	0.958	0.987	High polyhedral connectivity and structural superlattices

Continuation of table 1

Tl_9SbTe_6	0.845	0.871	0.999	0.876	Recently reported to be a good thermoelectric material ($zT \approx 1$ at 600 K)
$TaAlO_4$	0.893	0.703	1	0.977	High mass contrast, high polyhedral connectivity (TaO_6 octahedra dividing edges and vertices)
$SrCrO_3$	0.772	0.767	0.996	0.95	High polyhedral connectivity (3-*D* angular connection of CrO_6 octahedra), metallic, when created under high pressure.
$TaSbO_4$	0.892	0.919	1	0.997	High polyhedral connectivity: layered, edge-sharing MO_6 octahedra
TiCoSb	0.981	0.714	0.958	0.833	*TiCoSb* is not a new compound, but has been studied as a high *zT* material. However, it was not included in the training data.

Thanks to machine learning, the authors managed to be the first to propose an experimentally viable new compound from a real white chemical space, where no previous characteristics indicated promising chemical processes [10].

Another area where machine learning can find promising application is finding the dependences and parameters of the spin-controlled thermoelectric effect (STE) [19, 26]. Such devices could provide a universal thermoelectric technology with scalable production, but this is hindered by a lack of understanding of the fundamental physics and properties of the materials responsible for the effect. The article by Iwasaki et al. [19, 26] claims the synthesis of a material that helped in the identification of a new STE material with a thermal EMF that is an order of magnitude higher than that of the current generation of devices.

Recent works describe the emergence of new, more accurate models, which, in addition to predicting probably new interesting thermoelectric materials for research, also learn to predict the properties of materials with high accuracy, the coefficient of determination R_2 = 0.91-0.959 for well-studied materials [27 – 29].

One of the challenges facing improving the accuracy of such machine learning models is the creation of complete and high-quality databases of material properties, as well as access to them [30]. Despite the constant growth of interest in the application of machine learning algorithms for the search and discovery of new materials, today we have very modest tools compared to other areas of its application, namely image processing and industrial production. The degree of freedom (*DoF*) is the number of model variable parameters that are statistically significant. The degree of freedom directly affects the desired size of the required training data sets, so it is common to use models with a limited number of variable parameters and an approximate estimate of properties in the search space.

In the article by Gyoung S. Na et al. [31] a publicly open database of educational data was formed, obtained through a literature search containing the chemical structure and experimentally measured thermoelectric properties of materials. These data are presented in table form (Table 2) and total 5205 experimental values.

Table 2

Description of the collected characteristics in the ESTM data set [31]. The first value is the chemical composition of the collected thermoelectric materials, which must be translated into a digital representation when applied in machine learning models, the second value is the temperature. Other parameters were obtained either experimentally or theoretically calculated

Property name	Units of measurement	Range	Average value
Chemical composition	-	-	-
Temperature	K	[10, 1275]	539.28 ± 192.42
Seebeck coefficient	μV/K	[−1174, 1052.4]	73.18 ± 208.92
Electrical conductivity	S/m	(0.9.47E + 07)	1.10E + 05 ± 1.47E + 06
Thermal conductivity	W / m * K)	[0.07, 77.16]	2.25 ± 3.29
Power factor	W / (m * K^2)	(0. 7.61E − 03)	9.92E − 04 ± 1.12E − 03
ZT	-	(0. 2.28)	0.35 ± 0.35

As a result, based on the collected database, the authors of [31] developed a machine model that achieved an accuracy of R_2 above 0.9 in predicting 5 thermoelectric properties of materials and showed an average absolute error of less than 0.06 when predicting *ZT*. In addition to the publicly available dataset, the authors have developed a method for representing alloys and alloyed materials called System Identifiable Material Description (SIMD). Based on transfer learning using SIMD, it was possible to improve the R_2 from 0.13 to 0.71 when extrapolating to predict the *ZT* of materials from unexplored groups to find new high-performance materials.

Conclusions

1. The study of supervised and unsupervised machine learning methods used in thermoelectric materials science to optimize existing and search for new promising thermoelectric materials is considered.
2. Thanks to new opportunities, it becomes possible to further develop those areas of science that do not contain a perfect fundamental understanding, for example, the spin-driven thermoelectric effect, a deep understanding and determination of the interdependence between parameters that affect the efficiency of a thermoelectric material.
3. The accuracy of the latest models is high. However, their further improvement is limited by the space of well-studied materials and existing databases of experimentally collected thermoelectric properties of materials or theoretically calculated using alternative methods.

The author expresses his sincere gratitude to his supervisor, Lukyan Ivanovich Anatychuk, for the proposed topic of the work and useful remarks.

References

1. Liu Y., Zhao T., Ju W., & Shi S. (2017). Materials discovery and design using machine learning. *Journal of Materiomics*, 3 (3), 159 - 177. Elsevier BV. https://doi.org/10.1016/j.jmat.2017.08.002

2. Juan Y., Dai Y., Yang Y., & Zhang J. (2021). Accelerating materials discovery using machine learning. *Journal of Materials Science & Technology*, 79, 178 - 190. Elsevier BV. https://doi.org/10.1016/j.jmst.2020.12.010
3. von Lilienfeld O. A. & Burke K. (2020). Retrospective on a decade of machine learning for chemical discovery. *Nature Communications*, 11 (1). Springer Science and Business Media LLC. https://doi.org/10.1038/s41467-020-18556-9
4. Kim E., Huang K., Saunders A., McCallum A., Ceder G. & Olivett, E. (2017). Materials synthesis insights from scientific literature via text extraction and machine learning. *Chemistry of Materials*, 29(21), 9436 - 9444). American Chemical Society (ACS). https://doi.org/10.1021/acs.chemmater.7b03500
5. Cao B., Adutwum L. A., Oliynyk A. O., Luber E. J., Olsen B. C., Mar A. & Buriak J. M. (2018). How to optimize materials and devices via design of experiments and machine learning: demonstration using organic photovoltaics. *ACS Nano*, 12 (8), 7434 - 7444. American Chemical Society (ACS). https://doi.org/10.1021/acsnano.8b04726
6. Queen H. J., J. J., D. T. J., K. V. S. Moses Babu and Thota S.P. (1021), Machine learning-based predictive techno-economic analysis of power system, *IEEE Access*, 9, 123504-123516, 2021, doi: 10.1109/ACCESS.2021.3110774.
7. Mahesh B. (2020). Machine learning algorithms-a review. *International Journal of Science and Research* (*IJSR*)*,* 9(1), 381 - 386.
8. Singh A., Thakur N. and Sharma A. A review of supervised machine learning algorithms (2016). *3rd International Conference on Computing for Sustainable Global Development* (INDIACom), New Delhi, India, 2016, pp. 1310-1315.
9. Alloghani M., Al-Jumeily D., Mustafina J., Hussain A. & Aljaaf A. J. (2019). A systematic review on supervised and unsupervised machine learning algorithms for data science. *Unsupervised and Semi-Supervised Learning* (pp. 3 – 21). Springer International Publishing. https://doi.org/10.1007/978-3-030-22475-2_1
10. Gaultois M. W., Oliynyk A. O., Mar A., Sparks T. D., Mulholland G. J. & Meredig, B. (2016). Perspective: Web-based machine learning models for real-time screening of thermoelectric materials properties. *APL Materials*, 4(5). AIP Publishing. https://doi.org/10.1063/1.4952607
11. Choudhary K., Garrity K. F., & Tavazza F. (2020). Data-driven discovery of 3D and 2D thermoelectric materials. *Journal of Physics: Condensed Matter*, 32 (47), 475501). IOP Publishing. https://doi.org/10.1088/1361-648x/aba06b
12. Somvanshi M., Chavan P., Tambade S. & Shinde S. V. (2016). A review of machine learning techniques using decision tree and support vector machine. *2016 International Conference on Computing, Communication, Control and Automation* (*ICCUBEA*). IEEE. https://doi.org/10.1109/iccubea.2016.7860040
13. Alrebdi T. A., Wudil Y. S., Ahmad U. F., Yakasai F. A., Mohammed J. & Kallas F. H. (2022). Predicting the thermal conductivity of Bi2Te3-based thermoelectric energy materials: A machine learning approach. *International Journal of Thermal Sciences,* 181, 107784. Elsevier BV. https://doi.org/10.1016/j.ijthermalsci.2022.107784
14. Chen D., Jiang F., Fang L., Zhu Y.-B., Ye C.-C. & Liu W.-S. (2022). Machine learning assisted discovering of new M2X3-type thermoelectric materials. *Rare Metals*, 41(5), 1543 – 1553. Springer Science and Business Media LLC. https://doi.org/10.1007/s12598-021-01911-0.

15. Sheng Y., Wu Y., Yang J., Lu W., Villars P. & Zhang W. (2020). Active learning for the power factor prediction in diamond-like thermoelectric materials. *Computational Materials*, 6(1). Springer Science and Business Media LLC. https://doi.org/10.1038/s41524-020-00439-8.
16. Na G. S. & Chang H. (2022). A public database of thermoelectric materials and system-identified material representation for data-driven discovery. *Computational Materials,* 8 (1). Springer Science and Business Media LLC. https://doi.org/10.1038/s41524-022-00897-2.
17. Uysal F., Kilinc E., Kurt H., Celik E., Dugenci M. & Sagiroglu S. (2017). Estimating Seebeck coefficient of a p-type high temperature thermoelectric material using bee algorithm multi-layer perception. *Journal of Electronic Materials,* 46(8), 4931 – 4938). Springer Science and Business Media LLC. https://doi.org/10.1007/s11664-017-5497-6
18. Jia X., Deng Y., Bao, X, Yao H., Li S., Li Z., Chen C., Wang X., Mao J., Cao F., Sui J., Wu J., Wang C., Zhang Q. & Liu X. (2022). Unsupervised machine learning for discovery of promising half-Heusler thermoelectric materials. *Computational Materials*, 8 (1). Springer Science and Business Media LLC. https://doi.org/10.1038/s41524-022-00723-9
19. Iwasaki Y., Sawada R., Stanev V., Ishida M., Kirihara A., Omori Y., Someya H., Takeuchi I., Saitoh E., & Yorozu S. (2019). Identification of advanced spin-driven thermoelectric materials via interpretable machine learning. *Computational Materials*, 5 (1). Springer Science and Business Media LLC. https://doi.org/10.1038/s41524-019-0241-9
20. Sheng Y., Deng T., Qiu P., Shi X., Xi J., Han Y. & Yang J. (2021). Accelerating the discovery of *Cu–Sn–S* thermoelectric compounds via high-throughput synthesis, characterization, and machine learning-assisted image analysis. *Chemistry of Materials*, 33(17), 6918 - 6924). American Chemical Society (ACS). https://doi.org/10.1021/acs.chemmater.1c01856
21. Shimizu N. & Kaneko H. (2020). Direct inverse analysis based on Gaussian mixture regression for multiple objective variables in material design. *Materials & Design*, 196, 109168. Elsevier BV. https://doi.org/10.1016/j.matdes.2020.109168
22. Antunes L. M., Vikram Plata J. J., Powell A. V., Butler K. T. & Grau-Crespo R. (2022). Machine learning approaches for accelerating the discovery of thermoelectric materials. *ACS Symposium Series* (pp. 1 – 32). American Chemical Society. https://doi.org/10.1021/bk-2022-1416.ch001
23. Guo Q., Chan M., Kuropatwa B. A., & Kleinke H. (2013). Enhanced thermoelectric properties of variants of Tl_9SbTe_6 and Tl_9BiTe_6. *Chemistry of Materials,* 25(20), 4097 - 4104). American Chemical Society (ACS). https://doi.org/10.1021/cm402593f
24. Parker D., & Singh D. J. (2013). Alkaline earth lead and tin compounds Ae_2Pb, Ae_2Sn, $Ae = Ca$, Sr, Ba, as thermoelectric materials. *Science and Technology of Advanced Materials,* 14(5), 055003. Informa UK Limited. https://doi.org/10.1088/1468-6996/14/5/055003
25. Sun P., Oeschler N., Johnsen S., Iversen B. B. and Steglich F. (2009). Huge thermoelectric power factor: $FeSb_2$ versus $FeAs_2$ and $RuSb_2$, *Appl. Phys. Express* 2, 091102.
26. Iwasaki Y., Takeuchi I., Stanev V., Kusne A. G., Ishida M., Kirihara A., Ihara K., Sawada R., Terashima K., Someya H., Uchida K., Saitoh E, & Yorozu S. (2019). Machine-learning guided discovery of a new thermoelectric material. *Scientific Reports*, 9(1). Springer Science and Business Media LLC. https://doi.org/10.1038/s41598-019-39278-z
27. Jaafreh R., Yoo Seong, K., Kim J.-G. & Hamad K. (2022). A deep learning perspective into the figure-of-merit of thermoelectric materials. *Materials Letters,* 319, 132299. Elsevier BV. https://doi.org/10.1016/j.matlet.2022.132299
28. Li Y., Zhang J., Zhang K., Zhao M., Hu K. & Lin, X. (2022). Large data set-driven machine learning models for accurate prediction of the thermoelectric figure of merit. *ACS Applied*

Materials & Interfaces, 14(50), 55517 - 55527). American Chemical Society (ACS). https://doi.org/10.1021/acsami.2c15396
29. Wang T., Zhang C., Snoussi H. & Zhang G. (2019). Machine learning approaches for thermoelectric materials research. Advanced Functional Materials, 1906041. https://doi.org/10.1002/adfm.201906041
30. Na G.S., Chang H. (2022). A public database of thermoelectric materials and system-identified material representation for data-driven discovery. *Comput Mater* 8 (1), 214. Springer Science and Business Media LLC https://doi.org/10.1038/s41524-022-00897-2.

Submitted: 10.01.2023

Короп М. М.

Інститут термоелектрики НАН та МОН України,
вул. Науки, 1, Чернівці, 58029, Україна,
e-mail: mykola.korop@chnu.edu.ua

МАШИННЕ НАВЧАННЯ В ТЕРМОЕЛЕКТРИЧНОМУ МАТЕРІАЛОЗНАВСТВІ

У роботі наводяться методи машинного навчання та їхнє застосування в термоелектричному матеріалознавстві. Показано результати їхнього застосування, сильні сторони та області застосування. Було взято до уваги складнощі, які виникають у процесі прогнозування властивостей термоелектричних матеріалів та способи їх подолання. Бібл. 30, рис. 1, табл. 2.
Ключові слова: методи машинного навчання, термоелектричне матеріалознавство.

References

1. Liu Y., Zhao T., Ju W., & Shi S. (2017). Materials discovery and design using machine learning. *Journal of Materiomics*, 3 (3), 159 - 177. Elsevier BV. https://doi.org/10.1016/j.jmat.2017.08.002
2. Juan Y., Dai Y., Yang Y., & Zhang J. (2021). Accelerating materials discovery using machine learning. *Journal of Materials Science & Technology*, 79, 178 - 190. Elsevier BV. https://doi.org/10.1016/j.jmst.2020.12.010
3. von Lilienfeld O. A. & Burke K. (2020). Retrospective on a decade of machine learning for chemical discovery. *Nature Communications*, 11 (1). Springer Science and Business Media LLC. https://doi.org/10.1038/s41467-020-18556-9
4. Kim E., Huang K., Saunders A., McCallum A., Ceder G. & Olivett, E. (2017). Materials synthesis insights from scientific literature via text extraction and machine learning. *Chemistry of Materials*, 29(21), 9436 - 9444). American Chemical Society (ACS). https://doi.org/10.1021/acs.chemmater.7b03500

5. Cao B., Adutwum L. A., Oliynyk A. O., Luber E. J., Olsen B. C., Mar A. & Buriak J. M. (2018). How to optimize materials and devices via design of experiments and machine learning: demonstration using organic photovoltaics. *ACS Nano*, 12 (8), 7434 - 7444. American Chemical Society (ACS). https://doi.org/10.1021/acsnano.8b04726
6. Queen H. J., J. J., D. T. J., K. V. S. Moses Babu and Thota S.P. (1021), Machine learning-based predictive techno-economic analysis of power system, *IEEE Access*, 9, 123504-123516, 2021, doi: 10.1109/ACCESS.2021.3110774.
7. Mahesh B. (2020). Machine learning algorithms-a review. *International Journal of Science and Research* (*IJSR*)*,* 9(1), 381 - 386.
8. Singh A., Thakur N. and Sharma A. A review of supervised machine learning algorithms (2016). *3rd International Conference on Computing for Sustainable Global Development* (INDIACom), New Delhi, India, 2016, pp. 1310-1315.
9. Alloghani M., Al-Jumeily D., Mustafina J., Hussain A. & Aljaaf A. J. (2019). A systematic review on supervised and unsupervised machine learning algorithms for data science. *Unsupervised and Semi-Supervised Learning* (pp. 3 – 21). Springer International Publishing. https://doi.org/10.1007/978-3-030-22475-2_1
10. Gaultois M. W., Oliynyk A. O., Mar A., Sparks T. D., Mulholland G. J. & Meredig, B. (2016). Perspective: Web-based machine learning models for real-time screening of thermoelectric materials properties. *APL Materials*, 4(5). AIP Publishing. https://doi.org/10.1063/1.4952607
11. Choudhary K., Garrity K. F., & Tavazza F. (2020). Data-driven discovery of 3D and 2D thermoelectric materials. *Journal of Physics: Condensed Matter*, 32 (47), 475501). IOP Publishing. https://doi.org/10.1088/1361-648x/aba06b
12. Somvanshi M., Chavan P., Tambade S. & Shinde S. V. (2016). A review of machine learning techniques using decision tree and support vector machine. *2016 International Conference on Computing, Communication, Control and Automation* (*ICCUBEA*). IEEE. https://doi.org/10.1109/iccubea.2016.7860040
13. Alrebdi T. A., Wudil Y. S., Ahmad U. F., Yakasai F. A., Mohammed J. & Kallas F. H. (2022). Predicting the thermal conductivity of Bi2Te3-based thermoelectric energy materials: A machine learning approach. *International Journal of Thermal Sciences,* 181, 107784. Elsevier BV. https://doi.org/10.1016/j.ijthermalsci.2022.107784
14. Chen D., Jiang F., Fang L., Zhu Y.-B., Ye C.-C. & Liu W.-S. (2022). Machine learning assisted discovering of new M2X3-type thermoelectric materials. *Rare Metals*, 41(5), 1543 – 1553. Springer Science and Business Media LLC. https://doi.org/10.1007/s12598-021-01911-0.
15. Sheng Y., Wu Y., Yang J., Lu W., Villars P. & Zhang W. (2020). Active learning for the power factor prediction in diamond-like thermoelectric materials. *Computational Materials*, 6(1). Springer Science and Business Media LLC. https://doi.org/10.1038/s41524-020-00439-8.
16. Na G. S. & Chang H. (2022). A public database of thermoelectric materials and system-identified material representation for data-driven discovery. *Computational Materials,* 8 (1). Springer Science and Business Media LLC. https://doi.org/10.1038/s41524-022-00897-2.
17. Uysal F., Kilinc E., Kurt H., Celik E., Dugenci M. & Sagiroglu S. (2017). Estimating Seebeck coefficient of a p-type high temperature thermoelectric material using bee algorithm multi-layer perception. *Journal of Electronic Materials,* 46(8), 4931 – 4938). Springer Science and Business Media LLC. https://doi.org/10.1007/s11664-017-5497-6

18. Jia X., Deng Y., Bao, X, Yao H., Li S., Li Z., Chen C., Wang X., Mao J., Cao F., Sui J., Wu J., Wang C., Zhang Q. & Liu X. (2022). Unsupervised machine learning for discovery of promising half-Heusler thermoelectric materials. *Computational Materials*, 8 (1). Springer Science and Business Media LLC. https://doi.org/10.1038/s41524-022-00723-9
19. Iwasaki Y., Sawada R., Stanev V., Ishida M., Kirihara A., Omori Y., Someya H., Takeuchi I., Saitoh E., & Yorozu S. (2019). Identification of advanced spin-driven thermoelectric materials via interpretable machine learning. *Computational Materials*, 5 (1). Springer Science and Business Media LLC. https://doi.org/10.1038/s41524-019-0241-9
20. Sheng Y., Deng T., Qiu P., Shi X., Xi J., Han Y. & Yang J. (2021). Accelerating the discovery of *Cu–Sn–S* thermoelectric compounds via high-throughput synthesis, characterization, and machine learning-assisted image analysis. *Chemistry of Materials*, 33(17), 6918 - 6924). American Chemical Society (ACS). https://doi.org/10.1021/acs.chemmater.1c01856
21. Shimizu N. & Kaneko H. (2020). Direct inverse analysis based on Gaussian mixture regression for multiple objective variables in material design. *Materials & Design*, 196, 109168. Elsevier BV. https://doi.org/10.1016/j.matdes.2020.109168
22. Antunes L. M., Vikram Plata J. J., Powell A. V., Butler K. T. & Grau-Crespo R. (2022). Machine learning approaches for accelerating the discovery of thermoelectric materials. *ACS Symposium Series* (pp. 1 – 32). American Chemical Society. https://doi.org/10.1021/bk-2022-1416.ch001
23. Guo Q., Chan M., Kuropatwa B. A., & Kleinke H. (2013). Enhanced thermoelectric properties of variants of Tl_9SbTe_6 and Tl_9BiTe_6. *Chemistry of Materials,* 25(20), 4097 - 4104). American Chemical Society (ACS). https://doi.org/10.1021/cm402593f
24. Parker D., & Singh D. J. (2013). Alkaline earth lead and tin compounds Ae_2Pb, Ae_2Sn, *Ae* = *Ca*, *Sr*, *Ba*, as thermoelectric materials. *Science and Technology of Advanced Materials,* 14(5), 055003. Informa UK Limited. https://doi.org/10.1088/1468-6996/14/5/055003
25. Sun P., Oeschler N., Johnsen S., Iversen B. B. and Steglich F. (2009). Huge thermoelectric power factor: $FeSb_2$ versus $FeAs_2$ and $RuSb_2$, *Appl. Phys. Express* 2, 091102.
26. Iwasaki Y., Takeuchi I., Stanev V., Kusne A. G., Ishida M., Kirihara A., Ihara K., Sawada R., Terashima K., Someya H., Uchida K., Saitoh E, & Yorozu S. (2019). Machine-learning guided discovery of a new thermoelectric material. *Scientific Reports*, 9(1). Springer Science and Business Media LLC. https://doi.org/10.1038/s41598-019-39278-z
27. Jaafreh R., Yoo Seong, K., Kim J.-G. & Hamad K. (2022). A deep learning perspective into the figure-of-merit of thermoelectric materials. *Materials Letters,* 319, 132299. Elsevier BV. https://doi.org/10.1016/j.matlet.2022.132299
28. Li Y., Zhang J., Zhang K., Zhao M., Hu K. & Lin, X. (2022). Large data set-driven machine learning models for accurate prediction of the thermoelectric figure of merit. *ACS Applied Materials & Interfaces*, 14(50), 55517 - 55527). American Chemical Society (ACS). https://doi.org/10.1021/acsami.2c15396
29. Wang T., Zhang C., Snoussi H. & Zhang G. (2019). Machine learning approaches for thermoelectric materials research. Advanced Functional Materials, 1906041. https://doi.org/10.1002/adfm.201906041
30. Na G.S., Chang H. (2022). A public database of thermoelectric materials and system-identified material representation for data-driven discovery. *Comput Mater* 8 (1), 214. Springer Science and Business Media LLC https://doi.org/10.1038/s41524-022-00897-2.

Submitted: 10.01.2023

L. I. Anatychuk, *acad. National Academy of Sciences of Ukraine*[1,2]
R. R. Kobylianskyi, *cand. phys. - math. sciences*[1,2]
V. V. Lysko, *cand. phys. - math. sciences*[1,2]

Institute of Thermoelectricity of the NAS and MES of Ukraine,
1 Nauky str., Chernivtsi, 58029, Ukraine,
e-mail: anatych@gmail.com
[2]Yu.Fedkovych Chernivtsi National University,
2, Kotsiubynskyi str., Chernivtsi, 58012, Ukraine

COMPUTER DESIGN OF A THERMOELECTRIC PULMONARY AIR CONDENSER FOR THE DIAGNOSTICS OF CORONAVIRUS AND OTHER DISEASES

The physical model of a thermoelectric device for collecting exhaled air condensate is considered. By means of computer simulation, the distribution of temperature and velocity of air movement in the working chamber of the device was determined depending on the temperature of the working chamber, as well as humidity, temperature and volume of exhaled air. The results of calculations of the cooling efficiency of thermoelectric modules, necessary to ensure the specified modes of operation of the device, are given. Bibl. 6, Fig. 9.
Key words: diagnostics, coronavirus, condensate, exhaled air, thermoelectric cooling.

Introduction

The coronavirus disease COVID-19, caused by the severe acute respiratory syndrome coronavirus SARS-CoV-2, is attracting the attention of doctors, researchers, politicians and communities around the world. COVID-19 is the third major outbreak of a coronavirus in the last two decades, with a greater global impact than the previous outbreaks of coronaviruses in 2003 (SARS-CoV) and 2012 - 2015 and 2020 (MERS-CoV). Transmission of SARS-CoV-2 could be enhanced by spread from individuals with asymptomatic and mildly symptomatic disease. Diagnostic testing plays a crucial role in overcoming the pandemic of the coronavirus disease COVID-19. Rapid and accurate diagnostic tests are essential for identification and treatment of infected individuals, contact tracing, epidemiologic characterization, and healthcare decision-making.

Modern diagnostic testing for the coronavirus disease COVID-19 is based on the detection of the SARS-CoV-2 coronavirus in swab samples from the nasopharynx by the reverse transcription polymerase chain reaction (RT-PCR) method. However, this test is associated with an increased risk of viral spread and environmental contamination and shows a relatively low sensitivity due to technical shortcomings of the sampling method. Given that COVID-19 is transmitted through aerosols and droplets exhaled by humans, the detection of SARS-CoV-2 in lung condensate may serve as a promising non-invasive diagnostic method. This method is proposed in the works of scientists from Japan, the USA, Ireland and other countries as a more sensitive and reliable method of detecting COVID-19 [1 – 4]. Usually, special

devices are used to collect condensate - condensers, in which vapors from the air exhaled by a person condense at a temperature from 0 to -70 °C and are collected in a container for further research by the RT-PCR method [5].

It is important to ensure a controlled low temperature of the condenser, convenience, low cost and safety of using such a device. Lowering the condensation temperature makes it possible to speed up obtaining the amount of biological material required for research. At the same time, the operating temperatures of condensers that use ice at 0°C or compressor cooling down to -20 °C are not efficient enough and do not provide a high condensation rate. In addition, compressor condensers are complex, expensive, with insufficient control and maintenance of operating temperature, as well as the presence of dangerous refrigerants. There are attempts to make thermoelectric condensers of exhaled air, but their thermoelectric capabilities are not used to the maximum (the operating temperature level up to -20 °C). The temperature of -70 °C, which is achieved using dry ice (solid CO_2), is excessive and extremely inconvenient for operation, which radically reduces the possibilities of using this method. Therefore, it is important to create a thermoelectric condenser with precisely controlled temperatures below -20 °C and close to -70 °C without using dry ice.

The purpose of this work is the computer design and development of the design of the thermoelectric pulmonary air condenser for the diagnostics of coronavirus and other diseases.

Physical and computer models of thermoelectric pulmonary air condenser

The thermoelectric device for collecting condensate from the air exhaled by a person contains a cooling unit, a power supply unit and a respiratory circuit. The physical model of its main element, the cooling unit, is shown in Fig. 1.

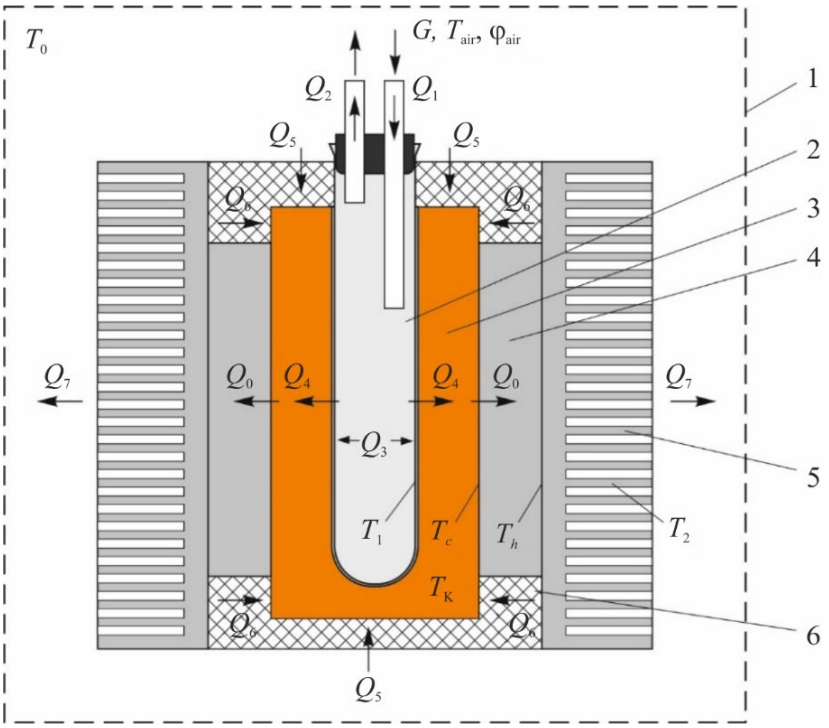

Fig. 1 – Physical model of the cooling unit of a thermoelectric device for collecting condensate from the air exhaled by a person: 1 – thermostat (device body); 2 – tube for collecting condensate; 3 – working chamber; 4 – thermoelectric modules; 5 – air heat exchangers; 6 –thermal insulation

In Fig. 1:

G, T_{air}, φ_{air} – flow rate, temperature and relative humidity of air exhaled by the patient;

Q_0 – cooling capacity of thermoelectric modules;

Q_1 – heat flow entering the tube for collecting condensate together with the air exhaled by the patient;

Q_2 – heat flow removed from the test tube to the environment;

Q_3 – the heat released in the test tube during the condensation of exhaled air vapours;

Q_4 – heat flow transferred from the walls of the test tube to the cooling chamber;

Q_5 – inflow of heat to the test tube from the environment through thermal insulation;

Q_6 – inflow of heat to the test tube from the air heat exchangers through thermal insulation;

Q_7 – heat flow removed from the air heat exchangers to the environment;

T_1 – the temperature of the test tube walls;

T_c – the cold side temperature of thermoelectric module;

T_h – the hot side temperature of thermoelectric module;

T_2 – the temperature of air heat exchangers;

T_0 – the temperature of environment (device body).

A computer model of the device was built using the Comsol Multiphysics software package. In doing so, the following program modules were used.

1. *Turbulent Flow*. Allows simulating turbulent flow using a wide range of turbulence models, as well as Large Eddy Simulation (LES) and Detached Eddy Simulation (DES). The eight turbulence models differ in how they model flow near walls, the number of additional variables that are calculated, and what these variables represent. All these models supplement the Navier-Stokes equation with an additional eddy viscosity term of turbulence, but they differ in the way it is calculated.

2. *Heat Transfer in Solids*. Allows solving equation

$$\rho C_p\left(\frac{\partial T}{\partial t} + \mathbf{u}_{\mathrm{trans}} \cdot \nabla T\right) + \nabla \cdot (\mathbf{q} + \mathbf{q}_r) = -\alpha T : \frac{dS}{dt} + Q$$

where:

- ρ – density (SI unit: kg/m^3);
- Cp – specific heat capacity at constant pressure (SI unit: J/(kg·K));
- T – absolute temperature (SI unit: K);
- $\mathbf{u}_{\mathrm{trans}}$ – vector of translational speed (SI unit: m/s);
- $\mathbf{q}$ – heat flow due to thermal conductivity (SI unit: W/m^2);
- $\mathbf{q}_r$ – heat flow due to radiation (SI unit: W/m^2);
- α – coefficient of thermal expansion (SI unit: 1/K);
- S – the second Piol-Kirchhoff stress tensor (SI unit: Pa);
- Q comprises additional sources of heat (SI unit: W/m^3).

For a stationary problem, the temperature does not change with time and conditions and derivatives disappear with time.

3. *Moisture Transfer in Air*. Interface of moisture transfer in air solves the equation

$$M_v \frac{\partial c_v}{\partial t} + M_v \mathbf{u} \cdot \nabla c_v + \nabla \cdot \mathbf{g} = G$$

in which the change in moisture content is expressed through the transfer of vapour concentration, which itself can be expressed as the product of the molar mass of water, the relative humidity, and the vapour saturation concentration:

$$\mathbf{g} = -M_v D \nabla c_v$$

$$c_v = \phi c_{sat}$$

with the following material properties, fields and source:

- M_v (SI unit: kg/mole – molar mass of water vapour;
- φ (dimensionless) – relative humidity;
- c_{sat} (SI unit: mole/m^3) – vapour saturation concentration;
- D (SI unit: m^2/s) – coefficient of vapour diffusion in air;
- u (SI unit: m/s) – air velocity field;
- G (SI unit: kg/(m^3·s)) – moisture source (or absorber).

Transfer of vapour concentration occurs by convection and diffusion in moist air. It is assumed that moisture consists only of vapour. In other words, the concentration of the liquid is zero.

4. *Heat Transfer in Moist Air*. It is used to model heat transfer in moist air by convection and diffusion using thermodynamic properties defined as a function of the amount of vapour in moist air.

5. *Multiphysics. Nonisotermal Flow*. Non-isothermal flow refers to fluid flows with non-constant temperatures. When a liquid undergoes a change in temperature, its material properties, such as density and viscosity, change accordingly. In some situations, these changes are large enough to have a significant effect on the flow field. And since the liquid transfers heat, the temperature field, in turn, is affected by changes in the flow field.

6. *Multiphysics. Moisture Flow.*. The Moisture Flow multiphysics coupling is used to model fluid flows where fluid properties (density, viscosity) depend on moisture content. The Moisture Flow interface allows one to maintain vapour concentration, mass and momentum in the air. It synchronizes the functions of the moisture transport and fluid flow interfaces when a turbulent flow regime is defined.

7. *Multiphysics. Heat and Moisture*. This Multiphysics relationship is used to model coupled heat and moisture exchange processes in various environments, including moist air by modeling moisture transport by vapour diffusion and convection and heat transfer by conduction and convection. The thermodynamic properties of moist air depend on the moisture content, while the temperature is used to define the saturation conditions for vapor concentration. This module synchronizes the functions of heat transfer and moisture transport interfaces:

- determines the relative humidity ϕw (with appropriate temperature and pressure) to adjust the appropriate input to the Wet Air function of the heat transfer interface;
- defines the temperature to set the model input data in the functions of the moisture transport interface;
- calculates the latent heat source due to evaporation and condensation fluxes on surfaces and adds it to the heat transfer equation.

The geometry of the working chamber with a tube for collecting condensate, as well as the mesh of the finite element method used for calculations in Comsol Multiphysics are shown in Fig. 2.

The created computer model allows one to calculate temperature distributions in the working chamber and tube for collecting condensate from air exhaled by a person, the velocity of air movement in the tube, and determine the amount of condensate received.

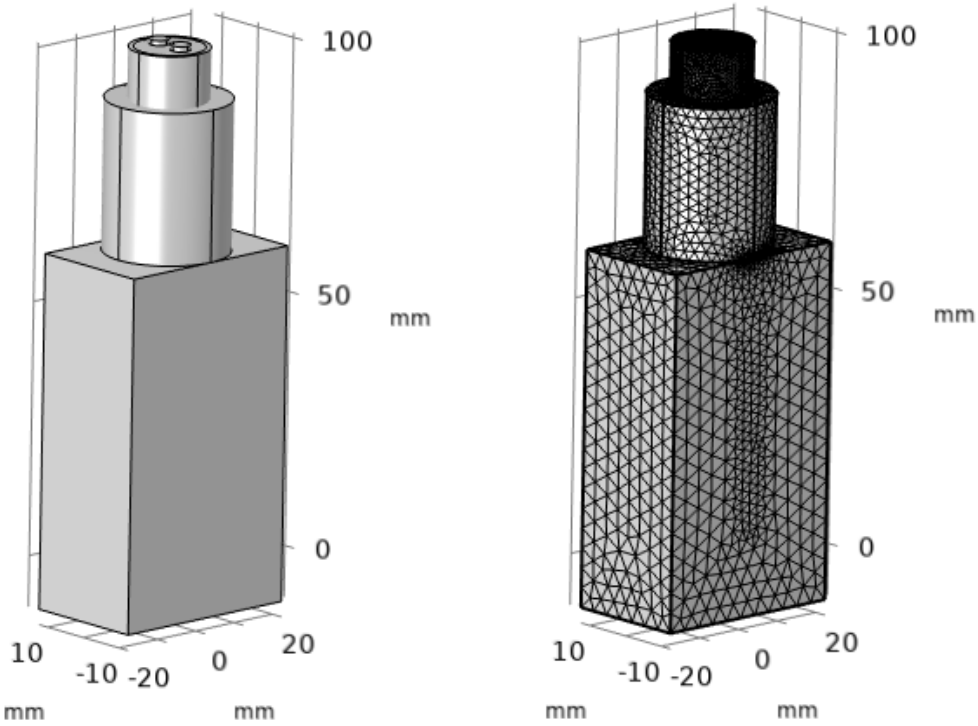

Fig. 2. A computer model of a thermoelectric device for collecting exhaled air condensate

Computer simulation results

The used boundary conditions of the computer model correspond to the physical model shown in Fig. 1. In this case, the average consumption of incoming air is determined by the number of exhalations per minute and the volume of exhaled air. It is known from the literature that the typical number of exhalations per minute is between 12 and 21. In doing so, the volume of exhaled air is equal to 0.3 - 0.7 l. The work [7] shows the results of experimental studies of the temperature and relative humidity of the exhaled air: the temperature range of exhaled air is 31.4 - 35.4 °C for participants from Haifa and 31.4 - 34.8 °C for participants from Paris, and the exhaled air relative humidity range is 65.0 - 88.6 % and 41.9 - 91.0 % for Haifa and Paris. participants respectively. That is, the temperature of air exhaled by people is in the range of 34 - 35 °C, and the relative humidity of the air is high, 90 % and above, regardless of geographical location.

The above ranges of input parameters were used for calculations. Fig. 3 shows typical temperature and air velocity distributions in the working chamber and condensate collection tube. The following input parameters were used for this case: temperature of the working chamber – 263.15 K; temperature of the air exhaled by a person is 306.65 K; humidity of exhaled air – 70 %; the average air velocity at the entrance to the test tube is equivalent to 12 exhalations per minute with an air volume of 0.31 l.

The computer model makes it possible to obtain similar distributions for other values of the input parameters, to build the dependence of the amount of collected condensate and its temperature on these parameters, to determine the requirements for thermoelectric modules and to optimize the design and operating modes of the device.

Figs. 4, 5 give an example of the results of computer calculations of the condensate collection velocity V_K (in ml per minute) and the thermal power Q_0 that must be removed from the working

chamber at different values of the temperature of the working chamber T_K,, relative humidity of the exhaled air φ_{air},, temperature and exhaled air consumption.

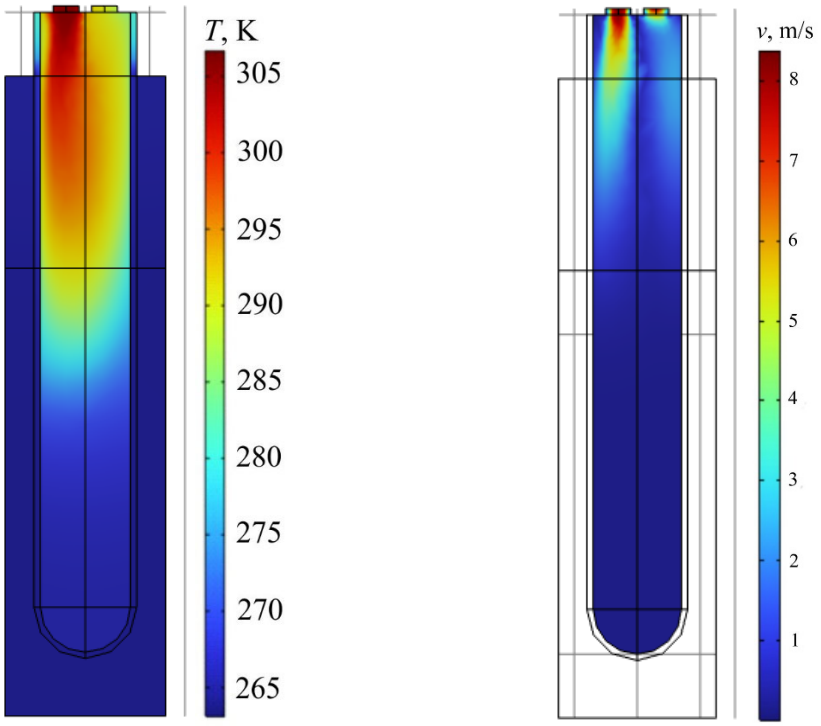

Fig. 3. Typical distributions of temperature (a) and air velocity (b) in the working chamber of the device for collecting exhaled air condensate

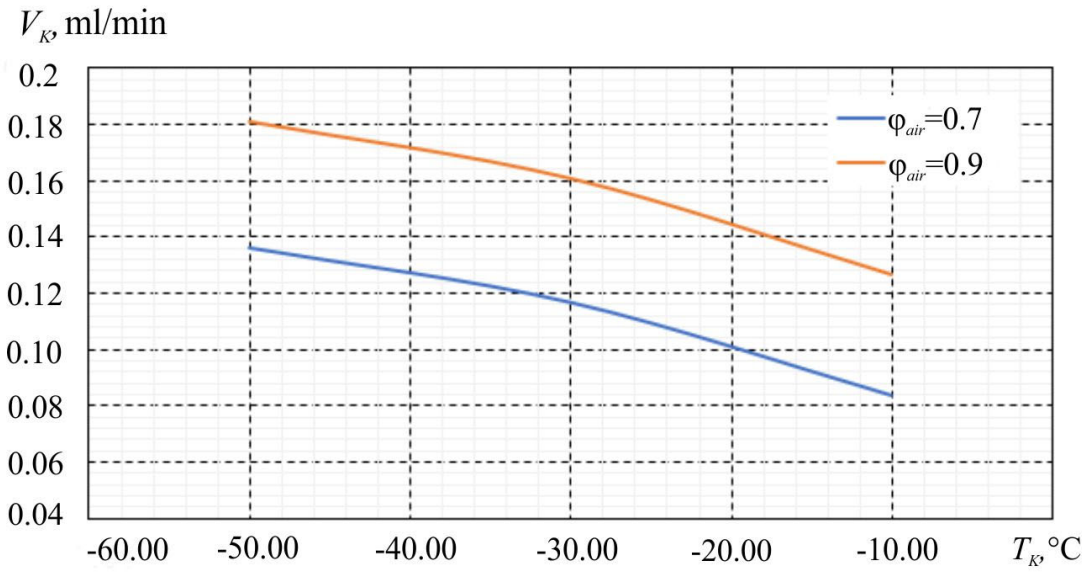

Fig. 4. Dependences of the condensate collection velocity V_K on the temperature in the working chamber T_K for different values of the relative humidity of the exhaled air (the temperature of the exhaled air is 33.5 °C; the air consumption is equivalent to 18 exhalations per minute with an exhalation volume of 0.5 l)

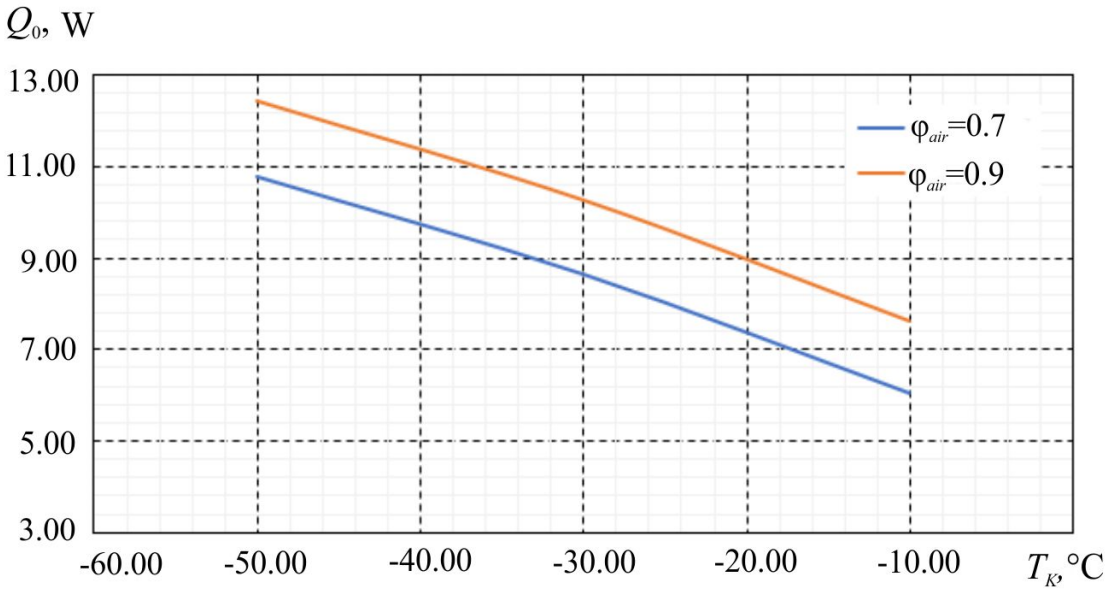

Fig. 5. Dependences of the thermal power Q_0 which must be removed from the working chamber, on the temperature in the working chamber T_K for different values of the relative humidity of the exhaled air (the temperature of the exhaled air is 33.5 °C; the air consumption is equivalent to 18 exhalations per minute with an exhalation volume of 0.5 l)

Fig. 6 shows the dependence of the condensate collection velocity V_K on the exhaled air consumption G for different temperature values of the working chamber T_K (at the exhaled air temperature of 33.5 °C and its relative humidity of 90 %). It can be seen that lowering the temperature of the working chamber from -10 °C to -50 °C allows you to increase the velocity of condensate collection by 1.5 times. Fig. 7 shows the dependence of the thermal power Q_0,, which must be removed from the working chamber to ensure such operating modes.

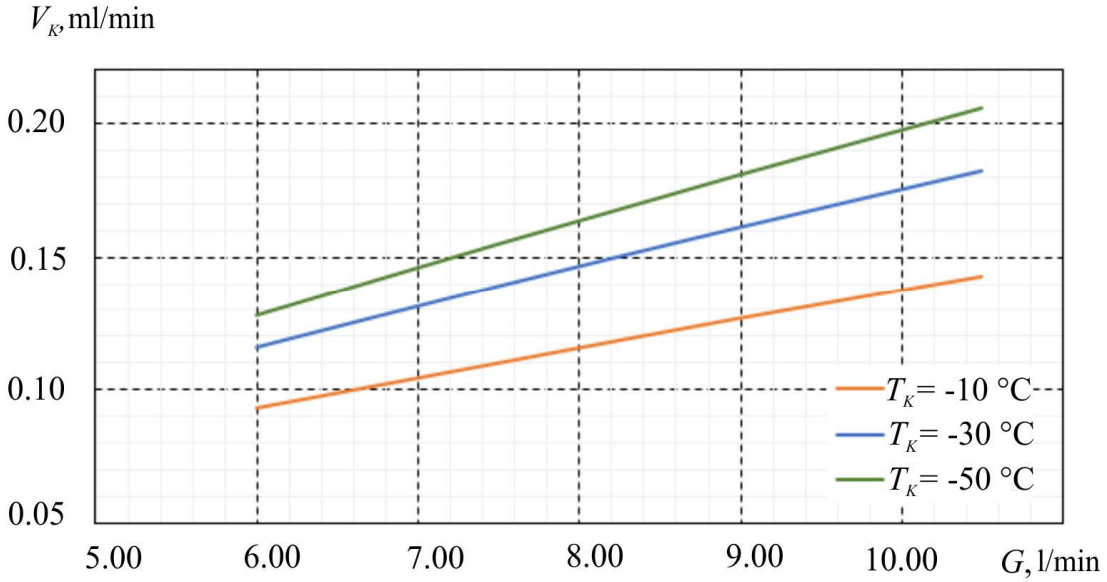

Fig. 6. Dependences of the condensate collection velocity V_K on the exhaled air consumption G for different values of the temperature of the working chamber T_K (at the temperature of the exhaled air 33.5 °C and its relative humidity 90 %)

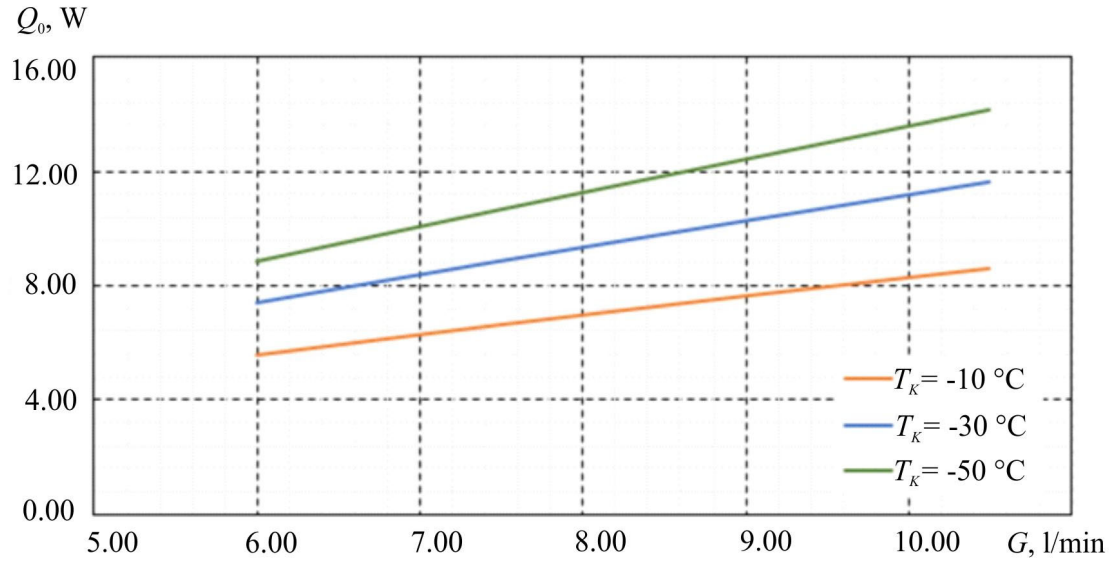

Fig. 7. Dependences of the thermal power Q_0, which must be removed from the working chamber, on the exhaled air consumption G for different temperature values of the working chamber T_K (at the temperature of the exhaled air 33.5 °C and its relative humidity 90 %)

Based on the results of computer simulation, to ensure the necessary operating modes of a thermoelectric device for collecting condensate from the air exhaled by a person, one module, for example, Altec-2 type produced by the Institute of Thermoelectricity, is sufficient to maintain the temperature of the working chamber at the specified cooling capacity of the module.

Using computer simulation in Comsol Multiphysics for the physical model shown above in Fig. 1, the values of heat inflow from the environment Q_{inflow} are calculated, consisting of heat Q_5 – heat inflow into the test tube from the environment through thermal insulation) and Q_6 – heat inflow into the test tube from air heat exchangers through thermal insulation. The calculation results are shown in Fig. 8.

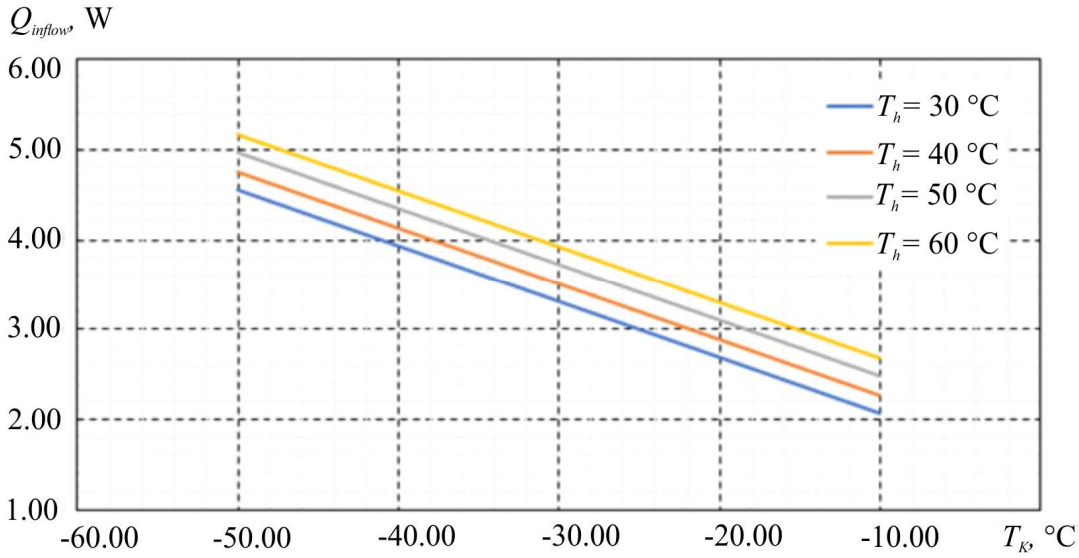

Fig. 8. Dependences of heat inflow from the environment Q_{inflow}. on the temperature of the working chamber T_K for different hot side temperatures of the thermoelectric module

Taking into account the maximum values of the thermal power Q_0,, which must be removed from the working chamber for different values of its temperature T_K, the dependence of the total cooling capacity of the thermoelectric module Q_{0total} on the temperature of the working chamber for different hot side temperature values of the module was obtained (Fig. 9).

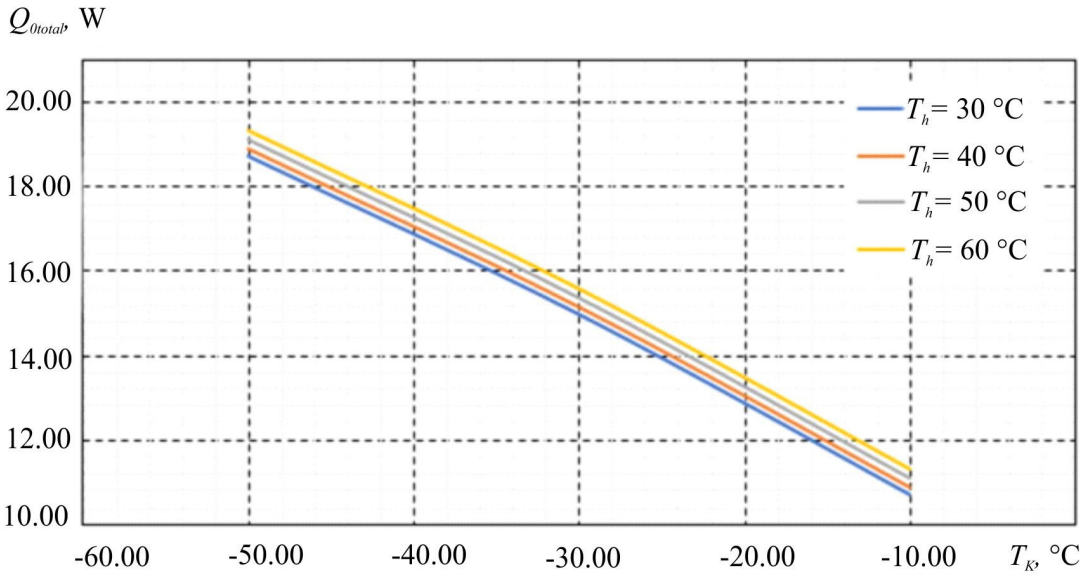

Fig. 9. Dependences of the cooling capacity of the thermoelectric module Q_{0total}. on the temperature of the working chamber T_K for different hot side temperature values of the thermoelectric module

Thus, in order to ensure the necessary modes of the working chamber of the device (temperature below -20 ℃) with a power consumption of the Altec-2 thermoelectric module of about 145 W and a cooling capacity of up to 20 W, a heat exchange system is required, which will remove about 165 W of heat with a temperature difference relative to the environment above 15 ℃.

The presented results are the basis for the further development of the design of a thermoelectric device for collecting exhaled air condensate.

Conclusions

1. A physical and computer model of a thermoelectric device was built for collecting condensate of exhaled pulmonary air to determine the distributions of temperature and air velocity in the working chamber of the device, to establish the patterns of heat transfer in such a device and to determine the conditions that ensure the achievement of the required level of operating temperatures and improvement of the efficiency of condensate collection.
2. The dependences of the distributions of temperature and air velocity in the working chamber of the device on the temperature of the working chamber, humidity, temperature and volume of exhaled air, and the amount of heat inflow from the environment are calculated. It has been established that lowering the temperature of the working chamber from -10 ℃ to -50 ℃ makes it possible to increase the velocity of condensate collection by a factor of 1.5.
3. It was established that to ensure the necessary operating modes of the device, namely, the temperature of the working chamber below -20 ℃, the cooling capacity of thermoelectric modules should be 15 - 20 W.

References

1. John Hunt. (2007). Exhaled breath condensate – an overview. *Immunol Allergy Clin North Am*., 27 (4). 587 - 596.
2. Hunt J. (2002). Exhaled breath condensate: An evolving tool for noninvasive evaluation of lung disease. *J Allergy Clin Immunol*, 110(1):28 – 34.
3. Horvath I., Hunt J. and Barnes P.J. (2005). Exhaled breath condensate: methodological recommendations and unresolved questions. *Eur Respir J*, 26: 523 – 548.
4. Reinhold P, Langenberg A, Becher G, Rothe M. (1999). Breath condensate – a medium obtained by a noninvasive method for the detection of inflammation mediators of the lung. *Berl Munch Tierarztl Wochenschr*, 254 – 259.
5. Efstathia M. Konstantinidi, Andreas S. Lappas, Anna S. Tzortzi, and Panagiotis K. Behrakis. Exhaled breath condensate: technical and diagnostic aspects (2015). *Scientific World Journal*. V 2015, Article ID 435160, 25 pages.
6. Mansour, Elias & Vishinkin, Rotem & Rihet, Stéphane & Saliba, Walaa & Fish, Falk & Sarfati, Patrice & Haick, Hossam. (2019). Measurement of temperature and relative humidity in exhaled breath. *Sensors and Actuators B Chemical*. 127371. 10.1016/j.snb.2019.127371.

Submitted: 15.02.2023

Анатичук Л. І., *акад. НАН України* [1,2]
Кобилянський Р. Р., *канд. фіз.-мат. наук* [1,2]
Лисько В. В., *канд. фіз.-мат. наук* [1,2]

[1]Інститут термоелектрики НАН та МОН України,
вул. Науки, 1, Чернівці, 58029, Україна;
[2]Чернівецький національний університет імені Юрія Федьковича,
вул. Коцюбинського 2, Чернівці, 58012, Україна
e-mail: *anatych@gmail.com*

КОМП'ЮТЕРНЕ ПРОЄКТУВАННЯ ТЕРМОЕЛЕКТРИЧНОГО КОНДЕНСАТОРА ЛЕГЕНЕВОГО ПОВІТРЯ ДЛЯ ДІАГНОСТИКИ КОРОНАВІРУСНИХ ТА ІНШИХ ЗАХВОРЮВАНЬ

Розглянуто фізичну модель термоелектричного приладу для збирання конденсату з повітря, що видихається людиною. Шляхом комп'ютерного моделювання визначено розподіли температури та швидкості руху повітря у робочій камері приладу в залежності від температури робочої камери, а також вологості, температури та об'єму видихуваного повітря. Наведено результати розрахунків холодопродуктивності термоелектричних модулів, необхідної для забезпечення заданих режимів роботи приладу. Бібл. 6, рис. 9.

Ключові слова: діагностика, коронавірус, конденсат, видихуване повітря, термоелектричне охолодження.

References

1. John Hunt. (2007). Exhaled breath condensate – an overview. *Immunol Allergy Clin North Am*., 27 (4). 587 – 596.
2. Hunt J. (2002). Exhaled breath condensate: An evolving tool for noninvasive evaluation of lung disease. *J Allergy Clin Immunol*, 110(1):28 – 34.
3. Horvath I., Hunt J. and Barnes P.J. (2005). Exhaled breath condensate: methodological recommendations and unresolved questions. *Eur Respir J*, 26: 523 – 548.
4. Reinhold P, Langenberg A, Becher G, Rothe M. (1999). Breath condensate – a medium obtained by a noninvasive method for the detection of inflammation mediators of the lung. *Berl Munch Tierarztl Wochenschr*, 254 – 259.
5. Efstathia M. Konstantinidi, Andreas S. Lappas, Anna S. Tzortzi, and Panagiotis K. Behrakis. Exhaled breath condensate: technical and diagnostic aspects (2015). *Scientific World Journal*. V 2015, Article ID 435160, 25 pages.
6. Mansour, Elias & Vishinkin, Rotem & Rihet, Stéphane & Saliba, Walaa & Fish, Falk & Sarfati, Patrice & Haick, Hossam. (2019). Measurement of temperature and relative humidity in exhaled breath. *Sensors and Actuators B Chemical*. 127371. 10.1016/j.snb.2019.127371.

Submitted: 15.02.2023

D. E. Rybchakov


D. E. Rybchakov

Institute of Thermoelectricity of the NAS and MES of Ukraine,
1, Nauky str., Chernivtsi, 58029, Ukraine,
e-mail: anatych@gmail.com

COMPUTER METHOD OF DESCRIPTION OF TECHNOLOGIES AND PROPERTIES OF THERMOELECTRIC Bi_2-Te_3 BASED MATERIAL BY EXTRUSION METHOD

This paper presents the results of a study of literature sources which describe the technology and properties of thermoelectric materials obtained by extrusion method. The result of one of the stages of creating a software product to describe the technologies for obtaining of a thermoelectric materials based on Bi-Te compounds and their properties are presented. Bibl. 7, Fig.4, Tabl.1.
Key words: extrusion method, extrapolation, bismuth telluride.

Introduction

Thermoelectric materials science is the most promising trend in thermoelectricity, covering such aspects as the development of methods for optimizing the parameters of thermoelectric materials (TEMs), the study of the properties of semiconductors traditionally used in thermoelectric conversion, and the improvement of technology for manufacturing TEMs for thermoelectric generators, refrigerators and measuring instruments, development of high-precision methods for measuring and monitoring material parameters.

The optimization of TEM properties is one of the most important issues in materials science. It is a well- known fact that thermoelectric materials must satisfy a number of requirements, often contradicting each other: have high values of figure of merit in a wide temperature range, have a high thermoEMF coefficient at low values of the resistivity and thermal conductivity coefficients, and be characterized by high mechanical strength. The mechanical and thermoelectric properties of materials described above depend, in their turn, on the structure, composition of the initial components, impurities, and manufacturing method.

Traditional methods for producing bismuth telluride compounds include Bridgman, Czochralski and zone melting methods, alongside with the powder metallurgy methods such as hot pressing and hot extrusion [1].

The purpose of this work is to study the thermoelectric characteristics of bismuth telluride based solid solutions obtained by extrusion. Using a modified computer programme to study the extrusion method and characteristics of thermoelectric materials based on *Bi-Te* compounds.

Dependence of thermoelectric characteristics of Bi_2-Te_3 based materials obtained by extrusion

When obtaining Bi_2Te_3 samples by extrusion, pre-formed pellets of thermoelectric material are pressed through a mold (die), during which the said pellet is heated to a temperature below the melting point [2]. Table 1 shows the thermoelectric characteristics of Bi_2-Te_3 based materials obtained by extrusion.

Table

Thermoelectric characteristics of Bi_2-Te_3 based materials obtained by extrusion

Operating temperature, K	Z, 10^{-3},K^{-1}	α, mV/K	σ, $Ohm^{-1}cm^{-1}$	κ, W/m·K	Material type:	Material composition:	Extrusion temperature, K
280	2.39	225	567	1.2	*P*	$Bi_{0.4}Sb_{1.6}Te_3$	753
328	2.44	239	512	1.2	*P*	$Bi_{0.4}Sb_{1.6}Te_3$	753
400	1.75	230	406	1.23	*P*	$Bi_{0.4}Sb_{1.6}Te_3$	753
475	0.90	200	332	1.47	*P*	$Bi_{0.4}Sb_{1.6}Te_3$	753
280	2.50	230	525	1.11	*P*	$Bi_{0.4}Sb_{1.6}Te_3$	753
328	2.50	241	469	1.09	*P*	$Bi_{0.4}Sb_{1.6}Te_3$	753
400	1.75	236	377	1.2	*P*	$Bi_{0.4}Sb_{1.6}Te_3$	753
475	0.93	205	295	1.34	*P*	$Bi_{0.4}Sb_{1.6}Te_3$	753
280	2.96	240	669	1.3	*P*	$Bi_{0.4}Sb_{1.6}Te_3$	753
328	2.74	247	809	1.8	*P*	$Bi_{0.4}Sb_{1.6}Te_3$	753
400	2	245	439	1.32	*P*	$Bi_{0.4}Sb_{1.6}Te_3$	753
475	1.16	206	422	1.55	*P*	$Bi_{0.4}Sb_{1.6}Te_3$	753
280	2.96	243	627	1.25	*P*	$Bi_{0.4}Sb_{1.6}Te_3$	753
328	2.89	252	556	1.22	*P*	$Bi_{0.4}Sb_{1.6}Te_3$	753
400	2.05	250	419	1.28	*P*	$Bi_{0.4}Sb_{1.6}Te_3$	753
475	1.22	207	421	1.48	*P*	$Bi_{0.4}Sb_{1.6}Te_3$	753
294	1.06	191	369	1.27	*P*	$Bi_{0.5}Sb_{1.5}Te_3$	613
294	2.17	229	438	1.06	*P*	$Bi_{0.5}Sb_{1.5}Te_3$	653
294	2.78	237	529	1.07	*P*	$Bi_{0.5}Sb_{1.5}Te_3$	693
294	2.72	241	568	1.21	*P*	$Bi_{0.5}Sb_{1.5}Te_3$	733
294	1.11	176	444	1.24	*P*	$Bi_{0.5}Sb_{1.5}Te_3$	593
294	1.94	177	879	1.42	*P*	$Bi_{0.5}Sb_{1.5}Te_3$	623
294	1.56	194	497	1.41	*P*	$Bi_{0.5}Sb_{1.5}Te_3$	613
294	1.71	197	564	1.29	*P*	$Bi_{0.5}Sb_{1.5}Te_3$	653
294	2.44	215	621	1.18	*P*	$Bi_{0.5}Sb_{1.5}Te_3$	693
294	2.70	225	675	1.27	*P*	$Bi_{0.5}Sb_{1.5}Te_3$	733
294	0.67	145	144	0.46	*P*	$Bi_{0.5}Sb_{1.5}Te_3$	573
294	1.63	207	263	0.69	*P*	$Bi_{0.5}Sb_{1.5}Te_3$	643
294	2.94	231	540	0.98	*P*	$Bi_{0.5}Sb_{1.5}Te_3$	713
300	2.7	150	1844	1.5	*P*	$(Bi_{0.3}Sb_{0.6})Te_3$	673
350	2.5	170	1423	1.6	*P*	$(Bi_{0.3}Sb_{0.6})Te_3$	673
400	2.1	180	1114	1.7	*P*	$(Bi_{0.3}Sb_{0.6})Te_3$	673
450	1.7	185	934	1.8	*P*	$(Bi_{0.3}Sb_{0.6})Te_3$	673
300	3.3	200	1083	1.3	*P*	$(Bi_{0.4}Sb_{0.8})Te_3$	673
350	2.85	215	834	1.35	*P*	$(Bi_{0.4}Sb_{0.8})Te_3$	673
400	2.4	210	761	1.4	*P*	$(Bi_{0.4}Sb_{0.8})Te_3$	673
450	1.7	212	573	1.45	*P*	$(Bi_{0.4}Sb_{0.8})Te_3$	673
300	3.16	250	658	1.3	*P*	$(Bi_{0.5}Sb_1)Te_3$	673
350	2.28	245	495	1.3	*P*	$(Bi_{0.5}Sb_1)Te_3$	673

Continuation of table

400	1.62	240	366	1.3	*P*	$(Bi_{0.5}Sb_1)Te_3$	673
450	1	215	281	1.3	*P*	$(Bi_{0.5}Sb_1)Te_3$	673
240	3.2	193	1350	1.57	*P*	$Bi_{0.4}Sb_{1.6}Te_3$	673-723
260	3.28	202	1180	1.47	*P*	$Bi_{0.4}Sb_{1.6}Te_3$	673-723
280	3.3	210	1010	1.35	*P*	$Bi_{0.4}Sb_{1.6}Te_3$	673-723
300	3.25	220	900	1.34	*P*	$Bi_{0.4}Sb_{1.6}Te_3$	673-723
320	3.19	225	800	1.27	*P*	$Bi_{0.4}Sb_{1.6}Te_3$	673-723
340	3.05	230	700	1.21	*P*	$Bi_{0.4}Sb_{1.6}Te_3$	673-723
360	2.78	235	675	1.34	*P*	$Bi_{0.4}Sb_{1.6}Te_3$	673-723
240	2.79	205	1195	1.80	*N*	$Bi_2Te_{2.82}Se_{0.18}$	673-723
260	2.83	215	1090	1.78	*N*	$Bi_2Te_{2.82}Se_{0.18}$	723-773
280	2.84	220	990	1.69	*N*	$Bi_2Te_{2.82}Se_{0.18}$	723-773
300	2.82	222	900	1.57	*N*	$Bi_2Te_{2.82}Se_{0.18}$	723-773
320	2.7	230	800	1.57	*N*	$Bi_2Te_{2.82}Se_{0.18}$	723-773
340	2.6	231	750	1.54	*N*	$Bi_2Te_{2.82}Se_{0.18}$	723-773
360	2.4	230	700	1.54	*N*	$Bi_2Te_{2.82}Se_{0.18}$	723-773
240	3.18	193	1300	1.52	*P*	$Bi_{0.4}Sb_{1.6}Te_3$	673-723
260	3.26	201	1130	1.40	*P*	$Bi_{0.4}Sb_{1.6}Te_3$	673-723
280	3.29	205	960	1.23	*P*	$Bi_{0.4}Sb_{1.6}Te_3$	673-723
300	3.25	209	850	1.14	*P*	$Bi_{0.4}Sb_{1.6}Te_3$	673-723
320	3.18	218	750	1.12	*P*	$Bi_{0.4}Sb_{1.6}Te_3$	673-723
340	3.04	220	670	1.07	*P*	$Bi_{0.4}Sb_{1.6}Te_3$	673-723
360	2.76	230	650	1.25	*P*	$Bi_{0.4}Sb_{1.6}Te_3$	673-723
240	2.74	193	1250	1.70	*N*	$Bi_2Te_{2.82}Se_{0.18}$	673-723
260	2.78	200	1145	1.65	*N*	$Bi_2Te_{2.82}Se_{0.18}$	723-773
280	2.80	205	1045	1.57	*N*	$Bi_2Te_{2.82}Se_{0.18}$	723-773
300	2.82	207	955	1.45	*N*	$Bi_2Te_{2.82}Se_{0.18}$	723-773
320	2.71	208	855	1.36	*N*	$Bi_2Te_{2.82}Se_{0.18}$	723-773
340	2.62	209	805	1.34	*N*	$Bi_2Te_{2.82}Se_{0.18}$	723-773
360	2.43	210	755	1.37	*N*	$Bi_2Te_{2.82}Se_{0.18}$	723-773
240	3.1	182	1600	1.71	*P*	$Bi_{0.4}Sb_{1.6}Te_3$	673-723
260	3.2	193	1400	1.63	*P*	$Bi_{0.4}Sb_{1.6}Te_3$	673-723
280	3.23	195	1200	1.41	*P*	$Bi_{0.4}Sb_{1.6}Te_3$	673-723
300	3.25	200	1100	1.35	*P*	$Bi_{0.4}Sb_{1.6}Te_3$	673-723
320	3.19	203	1000	1.29	*P*	$Bi_{0.4}Sb_{1.6}Te_3$	673-723
340	3.05	205	900	1.24	*P*	$Bi_{0.4}Sb_{1.6}Te_3$	673-723
360	2.83	207	800	1.21	*P*	$Bi_{0.4}Sb_{1.6}Te_3$	673-723
240	2.7	170	1450	1.55	*N*	$Bi_2Te_{2.82}Se_{0.18}$	673-723
260	2.73	180	1350	1.60	*N*	$Bi_2Te_{2.82}Se_{0.18}$	723-773
280	2.78	185	1250	1.54	*N*	$Bi_2Te_{2.82}Se_{0.18}$	723-773
300	2.8	195	1150	1.56	*N*	$Bi_2Te_{2.82}Se_{0.18}$	723-773
320	2.78	200	1050	1.51	*N*	$Bi_2Te_{2.82}Se_{0.18}$	723-773
340	2.7	203	1000	1.53	*N*	$Bi_2Te_{2.82}Se_{0.18}$	723-773
360	2.6	204	950	1.52	*N*	$Bi_2Te_{2.82}Se_{0.18}$	723-773
294	2.92	166	1600	1.51	*P*	$Bi_{0.3}Te_{1.7}Se_3$	-
294	3.25	208	960	1.28	*P*	$Bi_{0.6}Te_{1.4}Se_3$	-

Continuation of table

294	3.2	205	1020	1.34	*P*	$Bi_{0.6}Te_{1.4}Se_3$	-
294	1.62	296	168	0.91	*P*	$Bi_{0.6}Te_{1.4}Se_3$	-
294	3	215	1030	1.59	*N*	$Bi_2Te_{2.82}Se_{0.18}$	-
294	2	295	225	0.98	*N*	$Bi_2Te_{2.82}Se_{0.18}$	-
294	1.9	245	325	1.03	*N*	$Bi_2Te_{2.1}Se_{0.9}$	-
294	1.7	240	323	1.09	*N*	$Bi_2Te_{1.8}Se_{1.2}$	-
300	3.2	208	960	1.30	*P*	$Bi_{0,6}Te_{1.4}Se_3$	-
300	2.2	260	310	0.95	*P*	$Bi_{0.6}Te_{1.4}Se_3$	-
300	1.6	295	170	0.92	*P*	$Bi_{0.6}Te_{1.4}Se_3$	-
300	3.2	205	776	1.02	*P*	$Bi_{0.6}Te_{1.4}Se_{0.12}Te_{2.88}$	-
300	3.1	213	1055	1.54	*N*	$Bi_2Te_{2.82}Se_{0.18}$	-
300	2.9	240	655	1.30	*N*	$Bi_2Te_{2.82}Se_{0.18}$	-
300	2	295	260	1.13	*N*	$Bi_2Te_{2.82}Se_{0.18}$	-
300	3.2	208	960	1.30	*P*	$Bi_{0.5}Te_{1.5}Se_3$	-
300	2.92	163	1166	1.06	*N*	$Bi_2Te_{2.7}Se_{0.3}$	660
300	2.62	171	1059	1.18	*N*	$Bi_2Te_{2.7}Se_{0.3}$	660
300	2.55	157	1407	1.36	*N*	$Bi_2Te_{2.7}Se_{0.3}$	660
300	1.40	165	1308	2.53	*N*	$Bi_2Te_{2.7}Se_{0.3}$	660
300	1.73	175	1197	2.12	*N*	$Bi_2Te_{2.7}Se_{0.3}$	660
300	1.80	196	1975	2.34	*N*	$Bi_2Te_{2.7}Se_{0.3}$	660
300	2.03	214	846	1.91	*N*	$Bi_2Te_{2.7}Se_{0.3}$	660
300	2.10	202	940	1.83	*N*	$Bi_2Te_{2.7}Se_{0.3}$	660
300	2.50	207	978	1.69	*N*	$Bi_2Te_{2.7}Se_{0.3}$	660
300	2.33	222	741	1.57	*N*	$Bi_2Te_{2.7}Se_{0.3}$	660

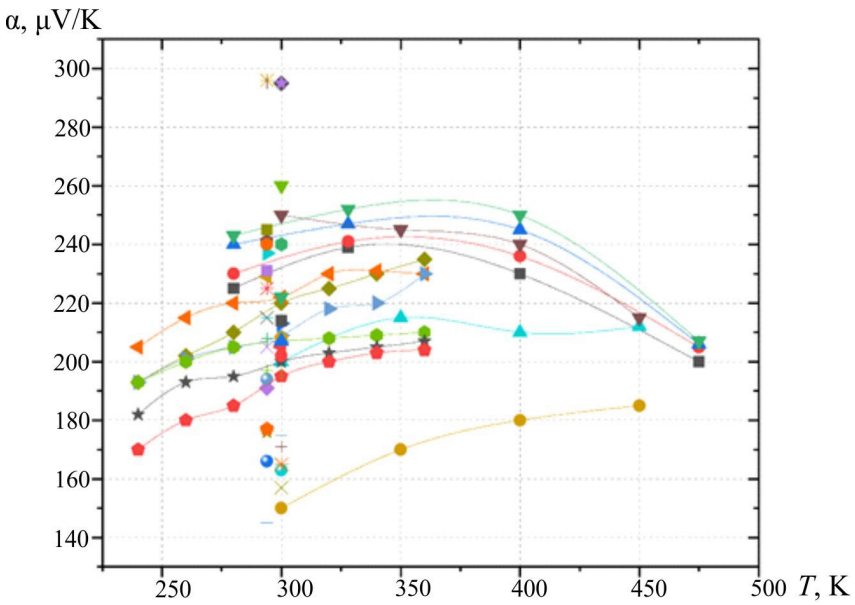

Fig. 1. Graph of dependence of thermoEMF on temperature

All data in the table were entered into a software product to describe the technologies and properties of *Bi-Te* based thermoelectric material. Updating the software product database will be described in the next articles. Based on the collected data, we will plot graphs of the dependence of electrical conductivity and thermoEMF on temperature fig. 1-3.

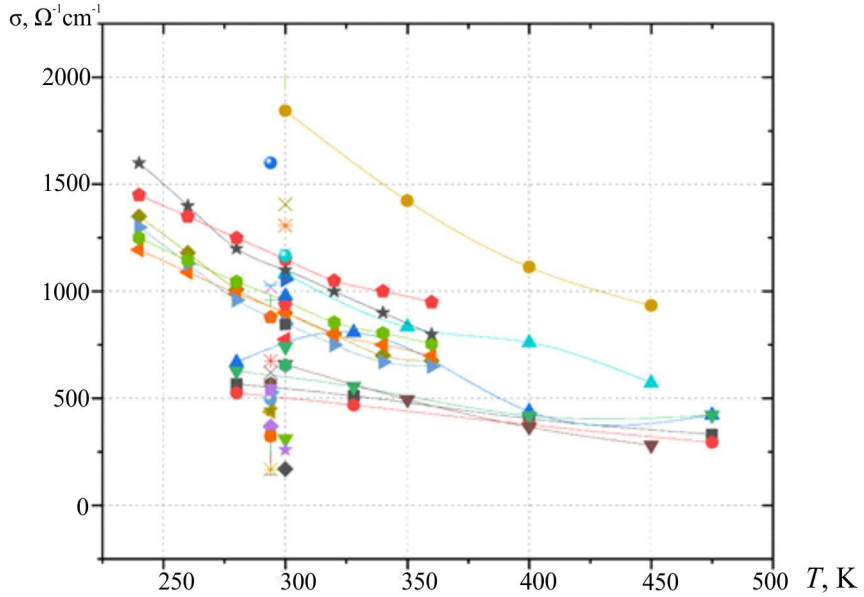

Fig. 2. Graph of dependence of electrical conductivity on temperature

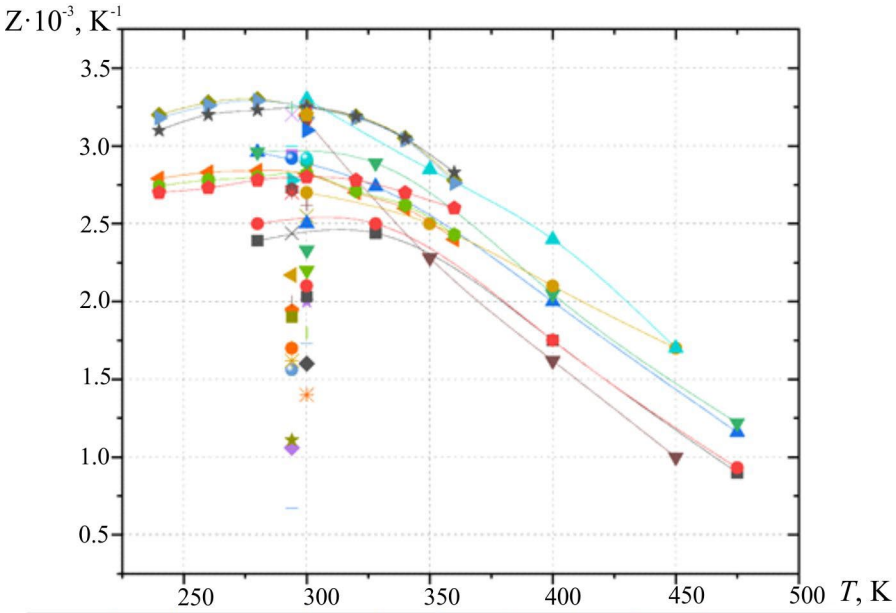

Fig. 3. Graph of dependence of the figure of merit on temperature

The given graphs not only clearly demonstrate the dependence of electrical conductivity, thermoEMF and figure of merit on temperature, but also allow introducing certain restrictions into the operation of the programme in order to bring the extrapolated values closer to the real ones.

Theory of linear extrapolation

Extrapolation in the general sense is a method of calculating certain values beyond the known range of any studied value based on a set of known values.

Linear extrapolation means creating a tangent line at the end of known data and extending it beyond those. Linear extrapolation will only provide good results when used to extend the graph of an approximately linear function or not too far beyond the known data.

If the two data points are closest to the point to be extrapolated and, the linear extrapolation is calculated according to formula 1:

$$Y = Y_0 + \big((Y_1 - Y_0) \div (X_1 - X_0)\big) \times (X - X_0) \quad (1)$$

where X_0 is the abscissa of the first point, X_1 is the abscissa of the second point, and X is the abscissa of the sought point, then Y_0 is the ordinate of the first point, Y_1 is the ordinate of the second point, and Y is the ordinate of the sought point.

(which is identical to linear interpolation if $X_{k-1} < X_* < X_k$). It is possible to include more than two points, and by averaging the slope of the linear interpolant, in regression-like techniques, on the data selected for inclusion. This is similar to linear prediction.[14].

The use of linear extrapolation in this work will allow predicting the behavior of materials, thus reducing the cost of resources and time to search for the optimal material for specific tasks.

Further development of the software product for describing the technologies and properties of *Bi-Te* based thermoelectric material

Currently, a function for theoretical prediction of unknown values of α and σ using extrapolation has been introduced into the software product for describing the technologies for obtaining of thermoelectric material based on *Bi-Te* compounds and their characteristics. The general algorithm for this function is as follows.

• User call of extrapolation function.

• Creation of a dynamic form and all its components for extrapolation.

• After the user enters the required operating temperature, the program searches the database for a material with the closest operating temperature range.

• After selecting the optimal material, the program calculates the coefficient value using the linear extrapolation formula.

- Based on the obtained result, the programme builds a graph of temperature dependence.
- Having received the α results, the programme calculates the σ value using the linear extrapolation formula.
- Based on the obtained result, the programme builds a graph of temperature dependence.
- The results obtained are displayed in Label.
- When the user exits, the programme deletes all form components and the form.
- The general view of the value extrapolation window is shown in Fig. 4.

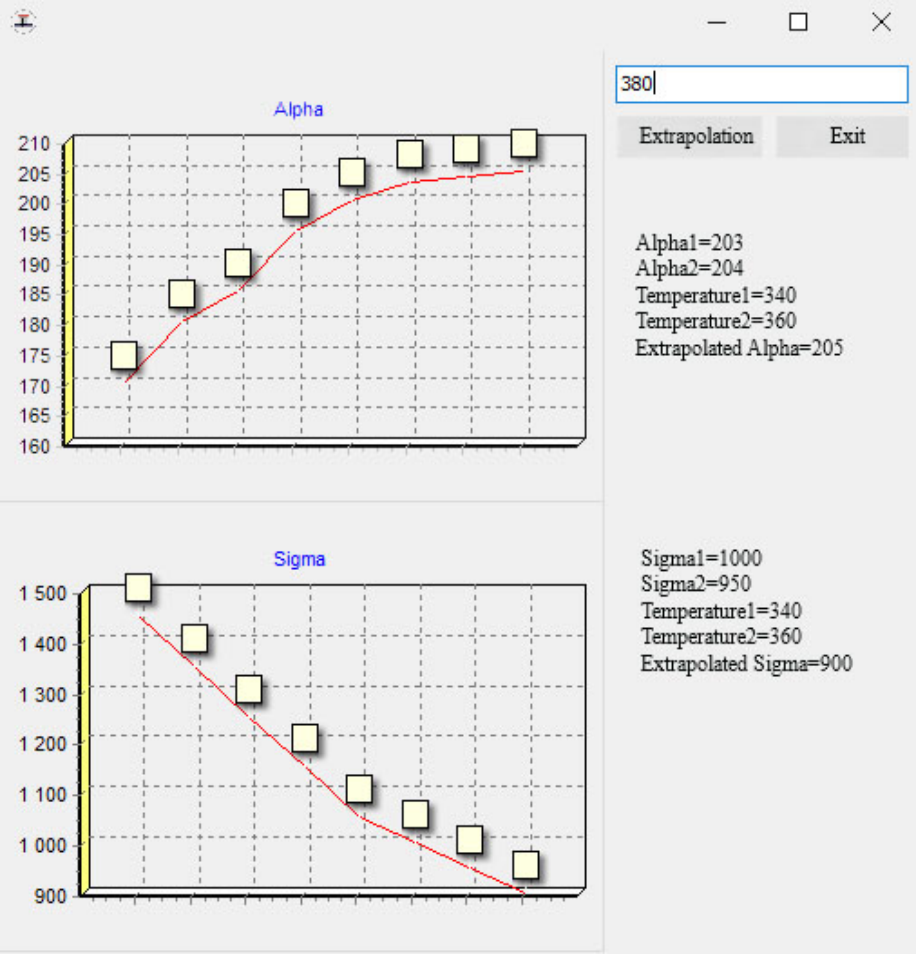

Fig. 4. General view of the value extrapolation window

Further development of the software product will be described in the articles in the future.

Conclusions

1. A study of literary sources that describe *Bi-Te* based thermoelectric materials, obtained by extrusion, was carried out.
2. These studies were added to the software product database to describe the technologies and properties of obtaining *Bi-Te* based thermoelectric materials.
3. The function of extrapolation was introduced into a software product to describe the technologies and properties of obtaining *Bi-Te* based thermoelectric materials.
4. Further versions of the software will be described in the articles in the future.

The author expresses gratitude to Academician of NASU Anatichuk Lukyan Ivanovich for the proposed topic of the article.

References

1. Enrique Maciá “Thermoelectric Materials: Advances and Applications”, CRC Press 05/2015, ISBN 9789814463522.
2. Sabo E.P. Technology of chalcogenide thermoelements. Physical fundamentals / E.P. Sabo //

Thermoelectricity. – 2006. – No. 1. – P. 45 – 66.
3. Fan X.A., Yang J.Y., Zhu W. et al (2008). Preferential orientation and thermoelectric properties of *p*-type $Bi_{0.4}Sb_{1.6}Te_3$ system alloys by mechanical alloying and equal channel angular extrusion. *Journal of Alloys and Compounds,* 461, 9 – 13.
4. K. Park. Thermoelectric properties of *p*-type Te doped $Bi_{0.5}Sb_{1.5}Te_3$ fabricated by powder extrusion / K. Park, J.H. Seo, D.C. Cho. // Materials Science and Engineering. – 2002. – P. 103 – 106.
5. J. Seo. Fabrication and thermoelectric properties of *p*-type $Bi_{0.5}Sb_{1.5}Te_3$ compounds by ingot extrusion / J. Seo, D. Cho, K. Park. // Materials Research Bulletin. – 2000. – №35. – P. 2157 – 2163.
6. J. Seo. Effect of extrusion temperature and dopant on thermoelectric properties for hot-extruded *p*-type *Te*-doped $Bi_{0.5}Sb_{1.5}Te_3$ and *n*-type SbI_3-doped $Bi_2Te_{2.85}Se_{0.15}$ / J. Seo, C. Lee, K. Park. // Materials Science and Engineering. – 1998. – P. 135 – 140.
7. Bongki Min. Texture-induced reduction in electrical resistivity of *p*-type $(Bi, Sb)_2Te_3$ by a hot extrusion / Bongki Min, Sang-Soon Lim, Sung-Jin Jung. // Journal of Alloys and Compounds. – 2018. – №764. – P. 261 – 266.

Submitted: 22.02.2023

Рибчаков Д. Є.

Інститут термоелектрики НАН і МОН України,
вул. Науки, 1, Чернівці, 58029, Україна,
e-mail: anatych@gmail.com

КОМП'ЮТЕРНИЙ МЕТОД ОПИСУ ТЕХНОЛОГІЙ ТА ВЛАСТИВОСТЕЙ ТЕРМОЕЛЕКТРИЧНИХ МАТЕРІАЛІВ НА ОСНОВІ Bi_2-Te_3, ОТРИМАНИХ МЕТОДОМ ЕКСТРУЗІЇ

У даній роботі наводяться результати дослідження літературних джерел в яких описуються технології та властивості термоелектричних матеріалів отриманих методом екструзії. Наводяться результати одного з етапів створення програмного продукту для опису технологій отримання та властивостей термоелектричного матеріалу на основі сполук Bi-Te. Бібл. 7. рис. 4. табл. 1.

Ключові слова: метод екструзії, екстраполяція, телурид вісмуту.

References

1. Enrique Maciá "Thermoelectric Materials: Advances and Applications", CRC Press 05/2015, ISBN 9789814463522.
2. Sabo E.P. Technology of chalcogenide thermoelements. Physical fundamentals / E.P. Sabo // Thermoelectricity. – 2006. – No. 1. – P. 45 – 66.
3. Fan X. A., Yang J. Y., Zhu W. et al (2008). Preferential orientation and thermoelectric properties of *p*-type $Bi_{0.4}Sb_{1.6}Te_3$ system alloys by mechanical alloying and equal channel angular extrusion.

Journal of Alloys and Compounds, 461, 9 – 13.

4. K. Park. Thermoelectric properties of *p*-type Te doped $Bi_{0.5}Sb_{1.5}Te_3$ fabricated by powder extrusion / K. Park, J. H. Seo, D. C. Cho. // Materials Science and Engineering. – 2002. – P. 103 – 106.
5. J. Seo. Fabrication and thermoelectric properties of *p*-type $Bi_{0.5}Sb_{1.5}Te_3$ compounds by ingot extrusion / J. Seo, D. Cho, K. Park. // Materials Research Bulletin. – 2000. – №35. – P. 2157 – 2163.
6. J. Seo. Effect of extrusion temperature and dopant on thermoelectric properties for hot-extruded *p*-type *Te*-doped $Bi_{0.5}Sb_{1.5}Te_3$ and *n*-type SbI_3-doped $Bi_2Te_{2.85}Se_{0.15}$ / J. Seo, C. Lee, K. Park. // Materials Science and Engineering. – 1998. – P. 135 – 140.
7. Bongki Min. Texture-induced reduction in electrical resistivity of *p*-type $(Bi, Sb)_2Te_3$ by a hot extrusion / Bongki Min, Sang-Soon Lim, Sung-Jin Jung. // Journal of Alloys and Compounds. – 2018. – №764. – P. 261 – 266.

Submitted: 22.02.2023

I.A. Konstantynovych, *Ph.D PhD (Phys and Math),*
R.V. Kuz, *Ph.D PhD (Phys and Math),*
O.M. Makhanets *D.Sc (Phys and Math),*
R.G. Cherkez *D.Sc (Phys and Math).*

Yuriy Fedkovych Chernivtsi National University,
2 Kotsiubynskyi str., Chernivtsi, 58012, Ukraine,
e-mail: i.konstantynovych@chnu.edu.ua

SECTIONAL GENERATOR THERMOELEMENTS IN A MAGNETIC FIELD

Using computer simulation, temperature distributions in the working body of sectional thermoelements in a magnetic field were determined. Temperature dependences of the efficiency of sectional gyrotropic thermoelements were found. It was established that the efficiency of generator gyrotropic sectional thermoelements depends on the number of sections. Bibl. 14, Figs. 4.
Key words: thermomagnetic figure of merit, Nernst-Ettingshausen coefficient, sectional gyrotropic thermoelement, gyrotropic material, thermomagnetic figure of merit, efficiency.

Introduction

Today, thermoelectric devices and systems are used in many industries, including medical, space, military, energy, refrigeration and instrumentation. For further development, it is important to study known and create new types of thermoelectric materials and thermoelements based on them, in particular for generating electricity in magnetic fields in the presence of a perpendicular temperature gradient [1 – 14].

Gyrotropic generator thermoelements are known to have a number of advantages over classic ones, such as the solderless connection and thereby the possibility of adjusting the required voltage, which guarantees the reliability and manufacturability of gyrotropic thermoelements and converters in general. Gyrotropic thermoelements as sensors can also increase their sensitivity and response time due to constructive solutions and can be effectively used in measuring technology.

Therefore, the study of the efficiency of gyrotropic materials and thermoelements based on them is important and relevant for their further use in general measuring and instrument-making equipment. The purpose of this work is to calculate the main parameters of sectional gyrotropic thermoelements and assess the efficiency of their use.

Computer simulation results

To study the parameters of gyrotropic thermoelements, it is necessary to solve the following heat conduction equation with the corresponding boundary conditions:

$$\kappa\Delta T + \rho_0 j^2 + 2\alpha_a \left(j_y \frac{\partial T}{\partial x} - j_x \frac{\partial T}{\partial y} \right) = 0, \qquad (1)$$

where T is temperature; κ is thermal conductivity of the gyrotropic medium; ρ_0 is electric resistivity; x, y are coordinates; j, j_x, j_y are module and projections of the electric current density vector; $\alpha_\perp = Q_\perp B$ is the asymmetric part of the thermoEMF tensor; $Q_\perp$ is transverse Nernst-Ettingshausen coefficient; B is magnetic field induction.

$$\alpha = \begin{pmatrix} \alpha_0 & \alpha_a & 0 \\ -\alpha_a & \alpha_0 & 0 \\ 0 & 0 & \alpha_\perp \end{pmatrix}, \tag{2}$$

where $\alpha_0, \alpha_\perp$ are diagonal components of the thermoEMF tensor.

$$Z_Q = \frac{Q_\perp^2 B^2(r)}{\kappa\rho}. \tag{3}$$

To conduct further simulation, a number of gyrotropic materials were considered, and the most promising of them were determined. Further, using the experimental data, the temperature dependence of the thermomagnetic figure of merit was constructed for *InSb* and *InAs*, and polynomials were also obtained, which are subsequently used to construct temperature distributions and calculate the efficiency of gyrotropic thermoelements. Fig. 1 shows the temperature dependences of the thermomagnetic figure of merit of *InSb* and *InAs* materials. It is evident that the best material for the production of gyrotropic generator thermoelements is *InSb*, which is consistent with the experimental results presented in [1, 11, 12]

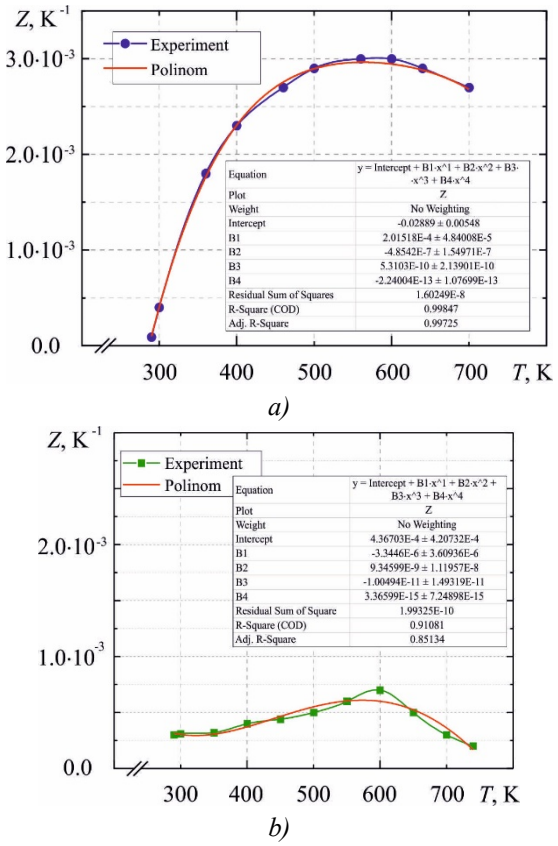

Fig. 1. Temperature dependence of thermomagnetic figure of merit for InSb (a) and InAs (b) materials

Hereinafter, the Comsol Multiphysics 6.2 application program package was used to build computer models of sectional gyrotropic thermoelements. Calculation of temperature distributions in gyrotropic thermoelements was carried out using the finite element method. Using computer simulation, temperature distributions were determined for the *InSb* material in the temperature range of 300–700 K and a magnetic field with induction B = 1.4 T (Fig. 2).

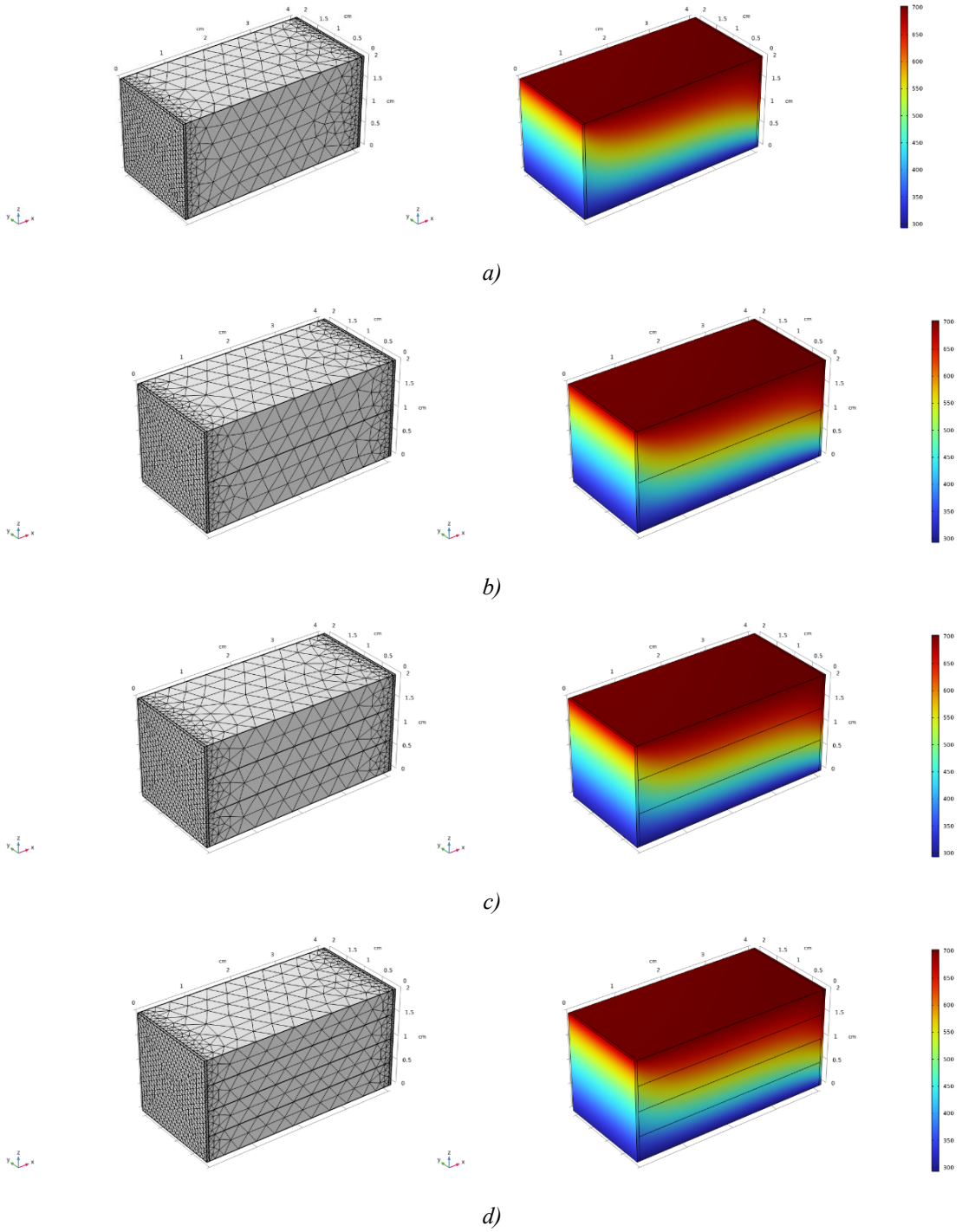

Fig.2. Three-dimensional models of the finite element method mesh (left) and temperature distribution (right) in single- and multi-section rectangular gyrotropic thermoelements with regard to thermoelectric contacts (where a – 1 section, b – 2 sections, c – 3 sections, d – 4 sections)

It is worth noting that contact electrical resistances are taken into account on the edges, which usually reduce the expected positive effect from the use of sectional legs.

Further, Fig. 3 shows the dependences of the efficiency of single- and multi-section thermoelements on the hot side temperature of *InSb* and *InAs* material.

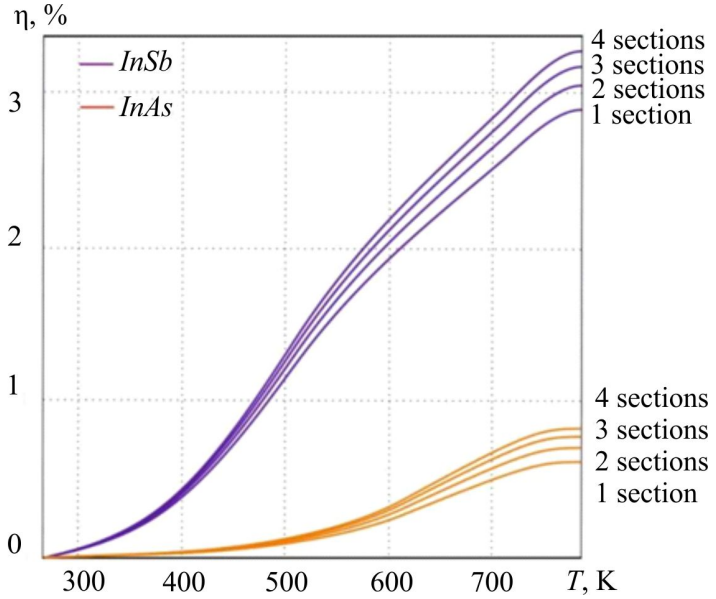

Fig. 3. Dependence of the efficiency on the temperature of sectional gyrotropic generator elements

From Fig. 3 it is evident that for the *InSb* material the efficiency of the sectional thermoelement is approximately 3.35 %, for the temperature range of 280 – 780 K and magnetic field induction of 1.4 *T*, which is almost 1.2 times greater than for a conventional rectangular thermoelement. Fig. 4 shows the dependence of the maximum efficiency on the number of sections *N* for *InSb* and *InAs*).

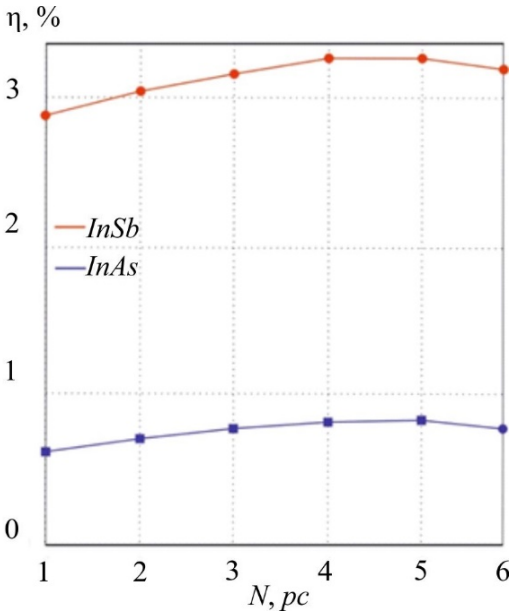

Fig. 4. Dependence of the maximum efficiency η *on the number of sections N (upper row of curves – InSb, lower row of curves – InAs)*

From Fig. 4 it can be seen that with an increase in the number of sections, the efficiency of the thermoelement decreases due to the influence of contact phenomena, which become more significant in this case.

Conclusions

1. Computer simulation methods were used to study temperature distributions in rectangular generator thermoelements, single- and multi-section, made of *InSb* and *InAs* thermoelectric materials.
2. The temperature dependences of the efficiency of sectional gyrotropic generator thermoelements were compared for different numbers of sections. It was found that for a 4-section thermoelement, the efficiency is approximately 3.35 %, for a temperature range of 280 – 780 K and a magnetic field induction of 1.4 *T*, which is almost 1.2 times more than for a conventional rectangular thermoelement for *InSb* material.

References

1. Anatychuk. L.I. (2003). *Termoelektrichestvo. T.2. Termoelektricheskiie preobrazovatelu energii [Thermoelectricity. Vol.2. Thermoelectric energy converters]*. Kyiv, Chernivtsi: Naukova Dumka.
2. Harman T.G., Honig J.M. (1967). *Thermoelectric and thermomagnetic effects and applications*. New York, Mc. Graw - Hill.
3. Samoilovich A.G. (2006). *Termoelektricheskiie i termomagnitnyie metody preobrazovaniia energii [Thermoelectric and thermomagnetic methods of energy conversion]*. Chernivtsi: Ruta.
4. Anatychuk L.I., Vikhor L.N. (1997). Low-temperature thermoelectric cooling under optimal legs inhomogeneity in the optimal nonuniform magnetic field. In: *Proc.of the 16 International Conference on Thermoelectrics* (Dresden, August 26 – 29, 1997).
5. Anatychuk L.I., Luste O.J., Fedoruk Ya.G., Shinkaruk S.M. (2004). Eddy thermoelectric currents in a gyrotropic medium with radial temperature distribution. *J. Thermoelectricity*, 1, 19 - 24.
6. Luste O.Ya., Fedoruk Ya.G. Gyrotropic thermocouple in an non-uniform magnetic field // Thermoelectricity. – 2006. – №1. – P. 16 – 22.
7. Konstantinovich I.A., Rendigevich O.V. (2016). On the efficiency of gyrotropic thermoelements in generation mode. *J.Thermoelectricity*, 1, 69 – 74.
8. Konstantinovich I.A. (2016). On the efficiency of gyrotropic thermoelements in cooling mode. *J.Thermoelectricity*, 3, 46 – 50.
9. Zakharchuk T.V, Konstantinovich I.A., Konstantinovich A.V, Forbatyuk A.V. (2019). On the efficiency of spiral gyrotropic thermoelements in cooling mode. *J. Thermoelectricity*, 1, 55 – 61.
10. Godovanets N.A, Konstantinovich I.A., Konstantinovich A.V., S.D. Shugani (2020). Gyrotropic thermoelement in uniform and non-uniform magnetic fields *J. Thermoelectricity*, 2, 25 – 32.
11. Nakamura H., Ikeda K. and Yamaguchi S. (1998). Transport coefficients of *InSb* in a strong magnetic field. Research report. *NIFS series (Nagoya, Japan).*
12. Hiroaki Nakamura, Kazuaki Ikeda, Satarou Yamaguchi. Transport coefficients of *InSb* in a strong magnetic field. (1997). *Proc. of XVI International conference on Thermoelectrics*. (Dresden, Germany, August 26 – 29, 1997).
13. Luste O.J., Fedoruk Ya.G. (2008). Optimization of materials for gyrotropic thermoelements. *J. Thermoelectricity*, 4, 21 –26.
14. Baransky P.I., Gaidar G.P. (2014). Anisotropy of thermoelectric properties of multi-valley

semiconductors of cubic symmetry under the influence of external directional effects. *J.Thermoelectricity*, 1, 13.

Submitted: 24.02.2023

Константинович І.А. *канд. фіз-мат. наук, доцент*
Кузь Р.В. *канд. фіз-мат. наук*
Маханець О.М. *доктор фіз-мат. наук, професор*
Черкез Р.Г. *доктор фіз-мат. наук, професор*

Чернівецький національний університет ім. Ю. Федьковича,
вул. Коцюбинського 2, Чернівці, 58012, Україна,
e-mail: i.konstantynovych@chnu.edu.ua

СЕКЦІЙНІ ГЕНЕРАТОРНІ ТЕРМОЕЛЕМЕНТИ В МАГНІТНОМУ ПОЛІ

За допомогою комп'ютерного моделювання визначено розподіли температур у робочому тілі секційних термоелементів у магнітному полі. Визначено температурні залежності ККД секційних гіротропних термоелементів. Встановлено, що ККД генераторних секційних гіротропних термоелементів залежить від кількості секцій. Бібл. 14, рис. 4.
Ключові слова: термомагнітна добротність, коефіцієнт Нернста-Еттінгсгаузена, секційний гіротропний термоелемент, гіротропний матеріал, термомагнітна добротність, ККД.

References

1. Anatychuk. L.I. (2003). *Termoelektrichestvo. T.2. Termoelektricheskiie preobrazovatelu energii [Thermoelectricity. Vol.2. Thermoelectric energy converters].* Kyiv, Chernivtsi: Naukova Dumka.
2. Harman T.G., Honig J.M. (1967). *Thermoelectric and thermomagnetic effects and applications*. New York, Mc. Graw - Hill.
3. Samoilovich A.G. (2006). *Termoelektricheskiie i termomagnitnyie metody preobrazovaniia energii [Thermoelectric and thermomagnetic methods of energy conversion].* Chernivtsi: Ruta.
4. Anatychuk L.I., Vikhor L.N. (1997). Low-temperature thermoelectric cooling under optimal legs inhomogeneity in the optimal nonuniform magnetic field. In: *Proc.of the 16 International Conference on Thermoelectrics* (Dresden, August 26 – 29, 1997).
5. Anatychuk L.I., Luste O.J., Fedoruk Ya.G., Shinkaruk S.M. (2004). Eddy thermoelectric currents in a gyrotropic medium with radial temperature distribution. *J. Thermoelectricity*, 1, 19 - 24.
6. Luste O.Ya., Fedoruk Ya.G. Gyrotropic thermocouple in an non-uniform magnetic field // Thermoelectricity. – 2006. – №1. – P. 16 – 22.
7. Константинович І.А., Рендигевич О.В. Про ефективність гіротропних термоелементів в режимі генерації // Термоелектрика. − № 1. – 2016. – С. 69-74.
8. Константинович І.А. Про ефективність гіротропних термоелементів в режимі охолодження // Термоелектрика. − № 3. – 2016. – С. 49-54.

9. Захарчук Т.В., Константинович І.А, Константинович А.В., Форбатюк А.В. Про ефективність спіральних гіротропних термоелементів у режимі охолодження// Термоелектрика №1. 2019. – С. 63-68.
10. Годованець Н.А., Константинович І.А., Константинович А.В., Шугані С.Д. Гіротропні термоелементи в однорідному та неоднорідному магнітних полях // Термоелектрика №2. 2020. – С. 35-42.
11. Nakamura H., Ikeda K. and Yamaguchi S. (1998). Transport coefficients of *InSb* in a strong magnetic field. Research report. *NIFS series (Nagoya, Japan).*
12. Hiroaki Nakamura, Kazuaki Ikeda, Satarou Yamaguchi. Transport coefficients of *InSb* in a strong magnetic field. (1997). *Proc. of XVI International conference on Thermoelectrics*. (Dresden, Germany, August 26 – 29, 1997).
13. Luste O.J., Fedoruk Ya.G. (2008). Optimization of materials for gyrotropic thermoelements. *J. Thermoelectricity*, 4, 21 –26.
14. Baransky P.I., Gaidar G.P. (2014). Anisotropy of thermoelectric properties of multi-valley semiconductors of cubic symmetry under the influence of external directional effects. *J.Thermoelectricity*, 1, 13.

Submitted: 24.02.2023

L. I. Anatychuk, *acad. National Academy of Sciences of Ukraine*[1,2]
V. G., Rifert, *doc. techn sciences* [3]
P. O., Barabash, *cand. techn sciences* [3]
R. V., Desiateryk, *cand. techn sciences* [3]
A. S., Solomakha, *cand. techn sciences* [3]
Yu. Yu., Rozver [1]
V. G., Petrenko, *cand. techn sciences* [3]

[1]Institute of Thermoelectricity of the NAS and MES of Ukraine,
1, Nauky str., Chernivtsi, 58029, Ukraine,
e–mail: anatych@gmail.com
[2]Yu.Fedkovych Chernivtsi National University,
2, Kotsiubynskyi str., Chernivtsi, 58012, Ukraine
[3] National Technical University of Ukraine
"Igor Sikorsky Kyiv Polytechnic Institute", 6 Polytechnichna str.,
Kyiv, 03056, Ukraine,
e-mail: vgrifert@ukr.net, barabash_tef@ukr.net, drv_td@ukr.net, as_solomaha@ukr.net, petrko@ukr.net

PERFORMANCE TESTING OF A THERMOELECTRIC HEAT PUMP FOR CENTRIFUGAL DISTILLATION OF WASTEWATER OF A SPACE LIFE SUPPORT SYSTEM

The paper describes the test results of a multistage centrifugal vacuum distillation (CMED) system with a thermoelectric heat pump (THP). The paper presents the results of research on the study of the main characteristics of the process of concentrating water and urine when using three- and five-stage distillers. Particular attention is paid to studying the influence of process parameters on the change in the efficiency of a thermoelectric heat pump. Bibl. 26, Fig. 4, Tabl. 3.
Key words: heat pump, distiller.

Introduction

For future long-term human missions to the Moon and Mars, water recovery systems from life support system wastewater are critical. NASA materials note that such a system should ensure maximum recovery of water from urine, moisture condensation and hygienic water.

Features of many technologies - reverse osmosis (RO), electrodialysis (ED), airborne evaporation (AES), mixed technologies (RO, AES, bioreactors), thermoelectric membrane evaporation (TIMES), vacuum compression distillation (VCD) and centrifugal multi-stage distillation (CMED) are considered in [1 – 3]. In doing so, only three technologies (TIMES, VCD, CMED) use the principle (method) of energy reduction, i.e. heat pumps. This paper describes the main characteristics of a thermoelectric heat pump (THP) in a CMED system.

Characteristics of TIMES and VCD

The TIMES system was developed in NASA back in 1975 and is described in reports and papers [4 – 8]. TIMES is a simple and effective system (*Gd* =1.0-1.5l/h, SPC=150 W*h/kg) with urine concentration up to 20 – 25 %. With increasing concentration, temperature depression increases and productivity sharply decreases (*Gd* < 1.0 l/h), and specific energy consumption increases to 150 - 250 Wh/kg. These results are explained by the fact that in TIMES the heat transfer coefficients (evaporation and condensation) have low values (according to our calculations, less than 1000 - 2000 W/m^2*^{o}C). Increasing the surface where the processes take place gives insignificant results. Moreover, low liquid flow rates (mainly urine) contribute to an increase in deposits on evaporation surfaces. This also leads to an increase in the total salt content in the distillate (up to 100 μS/cm) and increased ammonia concentrations (up to 100 mg/l or more) [4 – 6].

As with all technologies using membranes in areas of liquid evaporation, the main drawback is contamination of the membranes, which requires their frequent replacement.

Another option for thermal distillation is the vacuum compression distiller (VCD), analyzed in reports [9 – 11]. VCD uses the most efficient heat pump method – a mechanical compressor.

The transformation coefficient of a real vapor-compression heat pump is determined by the formula

$$\varphi = \frac{q_k}{l} = \frac{h_2 - h_3}{h_2 - h_1}$$

where

q_k is heat flow removed from the THP condenser, kJ/kg;

l is energy consumed by the comp ressor, kJ/kg;

h_1 is enthalpy of water vapor at the compressor inlet, kJ/kg;

h_2 is enthalpy of water vapor at the compressor outlet, kJ/kg;

h_3 is enthalpy of water vapour at the condenser outlet, kJ/kg;

Theoretically, at low ΔP on the compressor at the beginning of the concentration, energy consumption is < 10 - 20 W*h/kg. When the vapor pressure in the compressor increases, the density of the vapor increases under vacuum, which leads to a decrease in system productivity. This is also facilitated by the increase in temperature depression with increasing liquid concentration. Therefore, in all VCD tests [9 – 11], during the concentration process, productivity decreases by 2 times and energy consumption increases [12] to 200 Wh/l.

In [13, 14], the reasons for the high salt content of the distillate (up to 50-250 mg/l) are noted. VCD technology consumes only for the evaporation - condensation process (costs for compressor drive and concentration process) about 150-200 Wh/kg).

CMED system with a heat pump

The CMED system, developed by engineers and specialists from the Kiev Polytechnic Institute, the Thermodistillation company and the Institute of Thermoelectricity of the National Academy of Sciences of Ukraine, showed the best results: productivity - from 2 to 7 l/h, specific energy consumption - less than 100 - 200 Wh/kg, recovery – up to 98 %. These main characteristics have been published in many reports and articles [15 – 22].

CMED technology uses two scientifically and practically proven methods for reducing energy when concentrating heat-sensitive liquids such as urine - a thermoelectric heat pump (THP) and multi-stage liquid evaporation on a rotating surface.

High heat transfer coefficients during condensation and evaporation on a rotating surface with n = 500-1500 rpm amounted to $\alpha_u = (1 \div 2) \cdot 10^4 \frac{W}{m^2 * ℃}$ [23 – 26]. These characteristics ensure high film speed, which prevents salt deposits.

During the period 2000-2016, 2018-2022 a large number of tests were performed on 3 and 5 stage distillers. The identity of three distillers made in Ukraine and two THPs was noted. The purpose of these tests was to ensure the reliability of the CMED technology, study the influence of n, NTHP, type of liquid, improve characteristics (increase *Gd*, reduce SPC, improve distillate quality). Stable operation of the distiller and THP was noted without any shortcomings in the operation of the system. On the example of a study of a 3-stage distiller manufactured and tested back in 1986, it was indicated that long-term idleness of a centrifugal distiller does not affect its start-up and operation after a major shutdown.

Special attention in this paper is directed to the study of the characteristics of a thermoelectric heat pump. The results of tests on water and urine of 3-stage and 5-stage distillers with a thermoelectric heat pump were considered. The effect on Gd and SPC of the number of revolutions n = 800, 900, 1000, 1200, 1500 rpm, with NTHP = 100, 150, 200, 300, 400 and 600 Watts was studied. Cycles of each test were performed at t = 60, 90, 120 min.

We measured: N_{eng}, N_{THP}, G_d , $G_г$ and G_x, hot circuit temperatures t_1 and t_2, cold circuit temperatures t_3 and t_4. Based on these experimental data, the following characteristics were calculated:
1. amount of heat in the hot circuit

$$Q_{\text{г}} = \text{C}_{\text{p}} \cdot G_{in} \cdot \rho \cdot (t_2 - t_1)$$

where C_P is mass heat capacity of liquid, cm^3/sec;
G_{in} is flow rate of circulating liquid, J/^{o}C*g;
ρ is liquid density, g/cm^3
2. temperature difference in thermoelectric heat pump

$$\Delta T_{in} = t_1 - t_3$$

3. THP efficiency

$$\eta_{THP} = Q_г / N_{THP}$$

4. specific energy consumption in the distiller

$$SPC = (N_{дв} + N_{THP}) / G_d$$

where N_{mot} is electric power consumed by distiller motor, W;
$N_{THP}$is electric power consumed by the heat pump, W;
G_d is distiller productivity, l/h.

Unpublished data of testing a centrifugal distillation system with a thermoelectric heat pump, performed at the test benches the Thermodistillation company, jointly with the Institute of Thermoelectricity of the National Academy of Sciences of Ukraine and KPI specialists during 2000-2002 and 2022-2023, are presented.

Table 1 shows the results of testing a 3-stage distiller when concentrating water, Table 2 shows the results of testing a 5-stage distiller.

Table 1

№	n_{mot}, rpm, N_{mot}, W	N_{THP}, W	ΔT_{in}, °C	G_d, lph	η_{THP}	SPC, W*h/l	№	n_{mot}, rpm, N_{mot}, W	N_{THP}, W	ΔT_{in}, °C	G_d, lph	η_{THP}	SPC, W*h/l
1	1333 59	145	3.2	0.6	5	340	10	1200 41	214	2.9	2.01	2.45	127
2	1350 86	102	3.2	1.35	3.23	140	11	1200 42	309	7.4	2.48	2.2	141
3	1400 64	155	3.5	2.09	3.35	105	12	1200 42	196	3.5	1.76	2.76	135
4	1400 64	241	3.8	2.54	2.73	120	13	1040 29	392	9.5 9.2	1.91 2.9	2.76 1.98	220 145
5	1400 62	392	6.3	3.68	2.6	123	14	1200 42	196	3.5	1.91	2.6	125
6	1400 63	63	2.5	1.42	3.55	89	15	1380 57	217	5.7	2.18	2.83	126
7	1750 107	65	1.5	1.35	5.4	127	16	1580 75	414	4.9	3.5	2.24	140
8	1400 62	226	4.0	2.16	3.7	133	17	1200 48	235	5.5	1.92	2.56	147
9	1500 74	61.4	6.2	0.8	4.28	168							

Table 2

№	n_{mot}, rpm, $N_{дв}$, W	N_{THP}, W	ΔT_{in}, °C	G_d, lph	η_{THP}	SPC, W*h/l	№	n_{mot}, rpm, $N_{дв}$, W	N_{THP}, W	ΔT_{in}, °C	G_d, lph	η_{THP}	SPC, W*h/l
1	1500 74	90.7	6.1	1.13	3.65	146	9	1000 51	101	3.8	2.4	3.8	63
2	1500 74	244	4.6	2.37	2.9	134	10	1000 90	200	4.9	3.6	3.5	80
3	1570 90	414	5.1	3.47	2.24	145	11	1200 100	200	5.3	3.84	2.97	78
4	1200 90	408	8	5.6	2.1	89	12	1000 90	400	6.4	5.6	2.24	88
5	1000 96	212	5.7	3.66	2.87	84	13	1200 100	400	7	6.0	2.34	83
6	1200 96	236	5.9	3.8	2.7	87	14	1000 92	184	5.0	1.7	2.0	162
7	1200 100	420	7.4	6.0	2.1	87	15	1000 90	313	5.3	2.3	1.8	175
8	1200 100	415	7.4	6.0	2.0	86							

Table 3 shows the results of testing a 5-stage distiller when concentrating urine.

Table 3

№	n_{mot}, rpm, $N_{об}$, W	N_{THP}, W	ΔT_{in}, °C	G_d, lph	η_{THP}	SPC, W*h/l	№	n_{mot}, rpm, $N_{об}$, W	N_{THP}, W	ΔT_{in}, °C	G_d, lph	η_{THP}	SPC, W*h/l
1	800 39	400	6.9 7.9	3.5	1.97 2.02	125	9	1100 90	150	5.9 7.9	2.9 2.6	3.5 3.0	83 92
2	800 39	300	6.0 6.7	4.08 3.35	2.27 2.27	83 101	10	900 55	150	5.9 7.0	2.9	2.7	71
3	800 39	150	4.7 6.9	2.6	2.45 2.75	73	11	1000 66	600	8.7 10.1	5.0 4.0	1.91 1.89	133 166
4	800 39	200	6,4 8.8	2.82 2.90	2.41 2.45	85 82	12	1200 96	200	9.1 13.4	3.5	2.5	84
5	900 55	300	9.4 11.8	4.1	2.22	86	13	1100 93	400	9.9 11.4	5.34 5.23	2.16 2.04	92 94
6	1000 73	150	6.4 8.8	3.00 2.52	2.86 2.71	74 89	14	1100 93	200	7.0 7.6	3.25 3.5	3.1 2.73	90 84
7	1100 90	600	11.8 13.1	6.6 5.4	1.89 1.76	104 128	15	1200 114	400	12.5 13.5	5.06	2.74 2.0	102
8	1000 73	200	6.4 7.7	3.4 3.4	2.82 2.62	80 80	16	1060 80	300	7.4 9.0	4.3	2.4	88

In tables 1 and 2 with testing on water, one figure ΔT_{in} is written in all tests, since the temperature at the inlet to the THP does not change after turning on the system for no more than 5-10 minutes after turning on the engine. In table 3 on urine in the hot circuit, the temperature changes during the entire concentration period due to the appearance of temperature depression. Therefore, in these tables, ΔT_{in} increases during the entire concentration cycle. We have written this ΔT_{in}, its values at the beginning of the cycle and at the end of the system work.

Fig. 1 shows data on water evaporation in 3- and 5-stage distillers.

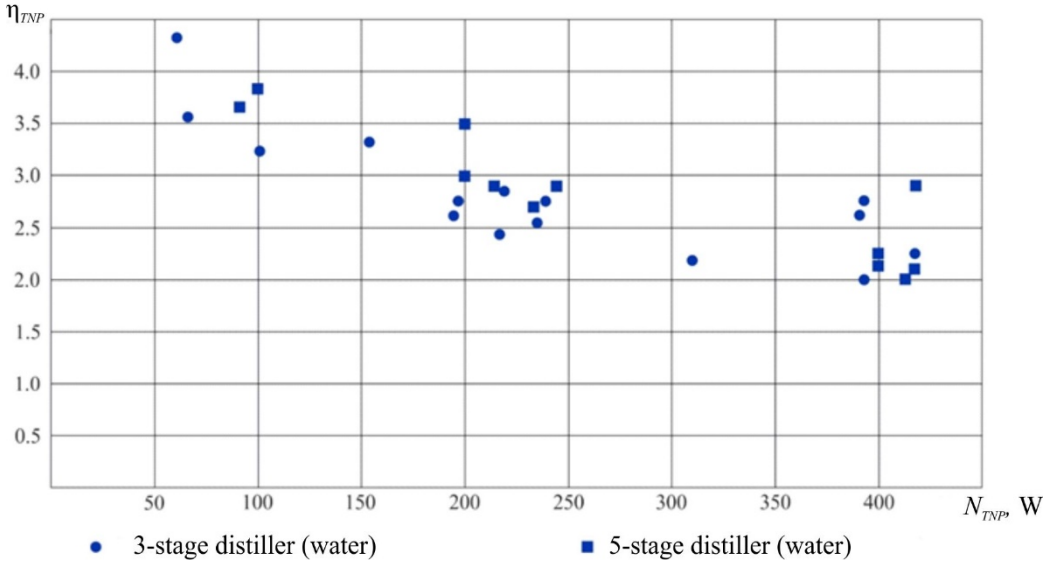

Fig.1. Dependence $\eta_{THP} = f(N_{THP})$ at n = 1000...1500 rpm

Fig. 2 shows data on the operation of a 5-stage distiller using urine.

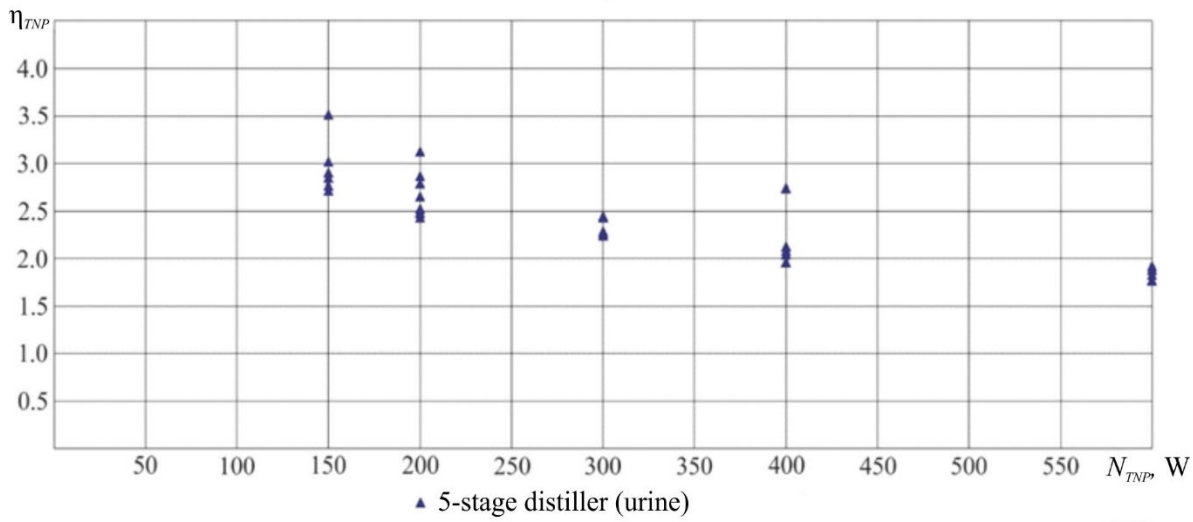

Fig.2. Dependence $\eta_{THP}= f(N_{THP})$ at n=800...1200 rpm

Figures 3 and 4 present a comparison of theoretical and experimental data on the dependence of the efficiency of a thermoelectric heat pump η_{THP} on power consumption for various coolant temperature differences at the inputs of the cold and hot circuits. Pump efficiency increases significantly as electrical consumption decreases and coolant temperatures become closer. Taking these dependencies into account makes it possible to optimize the energy parameters of the space distillation complex as a whole.

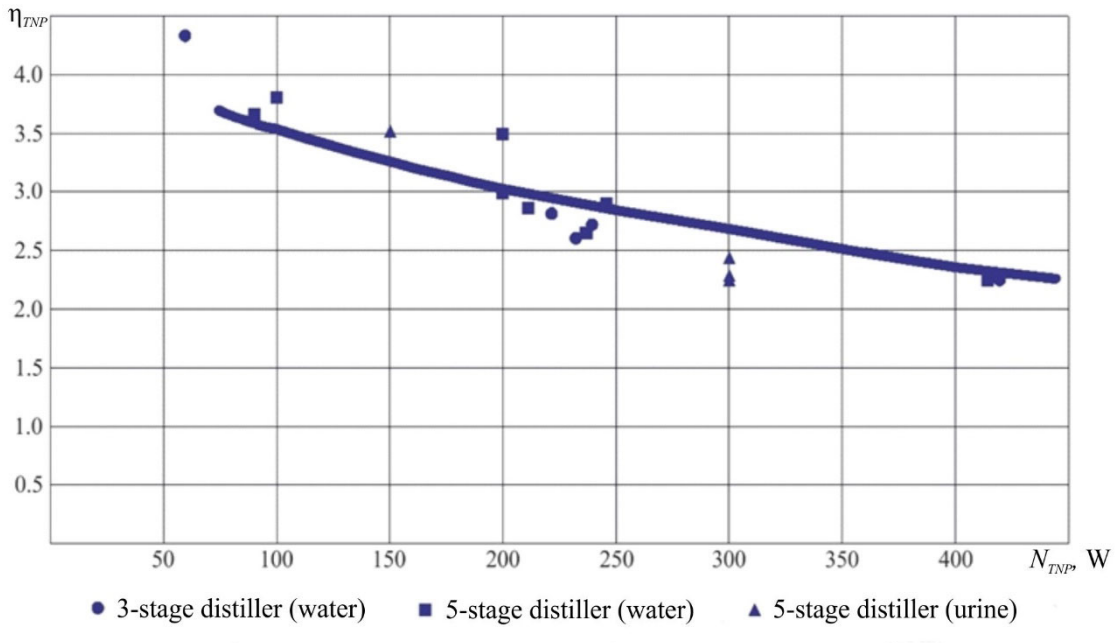

Fig.3. Comparison of experimental data with the results of theoretical calculations at $\Delta T_{in} = 5$℃

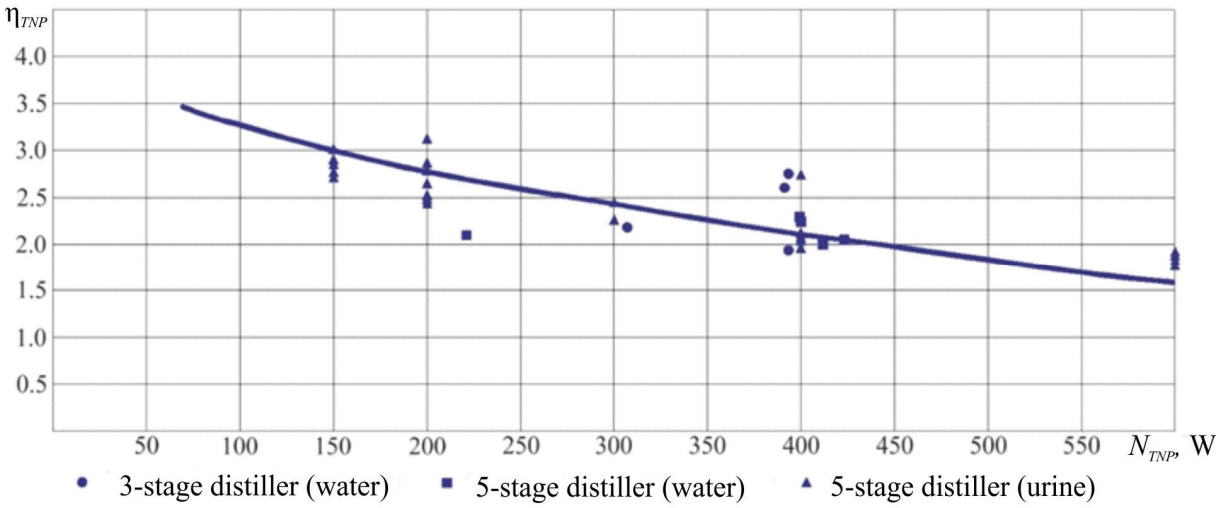

Fig.4. Comparison of experimental data with the results of theoretical calculations at $\Delta T_{in} = 10°C$

Summary

This paper presents a study of the efficiency factor of a thermoelectric heat pump based on the power it consumes. During the research, the power consumption of the heat pump varied from 60 to 600 Watts, and the distiller engine speed varied from 800 to 2000 rpm. When the heat pump power consumption changes from 400 to 600 Watts, the value of the η_{THP} coefficient changes slightly, while in the range of 200 - 400 Watts the η_{THP} value almost doubles. The maximum value of η_{THP} on the heat pump under study reaches 5 with a power consumption of 145 Watts. The specific energy consumption of SPC to produce one litre of distillate has minimum values precisely at low heat pump powers, which makes it possible to use this fact for the further development of energy-efficient distillation units.

References

1. Rifert, V. G., Anatychuk, L. I., Barabash, P. O., Solomakha A. S., Strykun A. P., Sereda, V. V., Prybyla,A. V. (2019). Evolution of centrifugal distillation system with a thermoelectric heat pump for space missions. *J. Thermoelectricity*, 3, 5 – 19.
2. Rifert V. G., Anatychuk L. I., Barabash P. O., Usenko V. I., Solomakha A. S., Petrenko V. G., Prybyla A. V., Sereda V. V. (2019). Comparative analysis of thermal distillation methods with heat pumps for long space flights. *J. Thermoelectricity*, 4, 5 – 18.
3. Rifert, V., Solomakha, A., Barabash, P. et al. (2022). Centrifugal multiple effect distiller for water recovery for space applications. *CEAS Space Journal*. https://doi.org/10.1007/s12567-022-00480-x
4. Roebelen, G., Jr., Dehner, G., Winkler, H. (1984). Thermoelectric integrated membrane evaporation water recovery technology. *SAE 93,559–570*. https:// doi.org/ 10. 4271/ 820849
5. Dehner, G. F., Reysa, R. P. (1985). Thermoelectric integration membrane evaporation subsystem water recovery technology update. In: *15 Intersociety Conference on environmental systems. Paper 851348*. https:// doi.org/ 10. 4271/ 851348
6. Dehner, G. F., Price, D. F. (1987). Thermoelectric integration membrane evaporation subsystem testing. *SAE Paper 871446*. https://doi.org/10.4271/871446
7. Thibaud-Erkey C., Fort J., Scull T., Edeen M. (2002). Performance testing of a new membrane evaporator for the thermoelectric integrated membrane evaporator system (TIMES) water

processor. In: *32nd International Conference on Environmental Systems. SAE 2002-01-2525.* https:// doi.org/ 10. 4271/ 2002- 01- 2525

8. Development of a prototype TIMES wastewater recovery subsystem. Roerelen G. J., Denher G. F. PREPARED UNDER CONTRACT NO. NAS 9-15471, 1982 and 1984
9. Rifert Vladimir G., Barabash Petr A., Usenko Vladimir, Solomakha Andrii S., Anatychuk Lukyan I., Prybyla A.V. Improvement the cascade distillation system for long-term space flights. *68th International Astronautical Congress (IAC), Adelaide, Australia, 25-29 September 2017*. IAC-17-A1.IP.25.
10. *Vapor compression distillation module* (Contracts NAS9-13714 & NAS9-14234), Prepared by P. P.Nuccio, 1975
11. Noble Larry D., Schubert Franz H., Pudoka Rick J., Miernik Janie H. (1990). Phase change water recovery for the space station free domand future exploration missions. *20th lntersociety Conference on Environmental Systems. Williamsburg, Virginia, July 9-12, 1990. SAE Technical Paper 901294.*
12. Wieland P., Hutchens C. and Long D., B. Salyer Final Report on Life Testing of the Vapor Compression Distillation / *Urine Processing Assembly (VCD/UPA) at the Marshall Space Flight Center (1993 to 1997) NASA/TM —1998–208539*
13. Carter L., Williamson J., Brown C.A., Bazley J., Gazda D., Schaezler R., Thomas Frank. (2018). Status of ISS water management and recovery. *48th International Conference on Environmental Systems. 8 - 12 July 2018, Albuquerque, NewMexico*. ICES-2018-088.
14. Carter L., Williamson J., Brown C.A., Bazley J., Gazda D., Schaezler R., Thomas Frank (2017). Status of ISS water management and recovery. *47th International Conference on Environmental Systems, 17 – 20 July 2017, Charleston, South Carolina*. ICES-2016-036
15. Rifert V. G., Anatychuk L. I., Barabash P. O., Solomakha A. S., Usenko V. I., Petrenko V. G. (2021). Justification of thermal distillation method with a thermoelectric heat pump for long-term space missions. *J. Thermoelectricity*, 1, 5 – 22. http://jt.inst.cv.ua/jt/jt_2021_01_en.pdf
16. Rifert V. G., Anatychuk L. I., Solomakha A. S., Barabash P. O., Petrenko V. G., Snegovskoy O. P. (2021). Influence of thermodynamic characteristics of a thermoelectric heat pump on the performance and energy consumption of a centrifugal distiller. *J. Thermoelectricity*, 2, 5 – http://jt.inst.cv.ua/jt/jt_2021_02_en.pdf
17. Rifert Vladimir G., Anatychuk Lukyan I., Solomakha Andrii S., Barabash Petr A., Usenko Vladimir, Prybyla A.V., Naymark Milena, Petrenko Valerii (20190. Upgrade the centrifugal multiple-effect distiller for deep space missions. *70th International Astronautical Congress (IAC), Washington D.C., United States, 21-25 October 2019.* IAC-19-A1,IP,11,x54316.
18. Solomakha A.S., Anatychuk L.I., Rifert V.G., Barabash P.A., Usenko V., Petrenko V. (2020). Thermal distillation system for deep space missions: rationale for the choice. *71st International Astronautical Congress (IAC) – The Cyber Space Edition, 12-14 October 2020*. IAC-20- A1,VP,15,x61344. 7 pages. https://www.iafastro.org/assets/files/publications/iac-publications/IAC2020-Virtual-FinalProgramme-2020-10-07-FINAL-online-Lowres.pdf
19. Rifert V., Barabash P., Goliad N. (1990). Methods and processes of thermal distillation of water solutions for closed water supply systems. *The 20th Intersociety Conference on Environmental Systems, Williamsburg, July 1990. SAE Paper 901249.*
20. Rifert V., Usenko V., Zolotukhin I., MacKnight A., Lubman A. (1999). Comparison of secondary water processors using distillation for space applications. *SAE Paper 99-70466, 29th International Conferenceon Environmental Systems, Denver, July 1999.*

21. Rifert V., Stricun A., Usenko V. (2000). Study of dynamic and extreme performances of multistage centrifugal distiller with the thermoelectric heat pump. *SAE Technical Papers 2000. 30th International Conferenceon Environmental Systems; Toulouse; France; 10-13 July 2000.*
22. Rifert V. G., Usenko V. I., Zolotukhin I. V., MacKnight A. and Lubman A. (2003). Cascaded distillation technology for water processing in space. SAE Paper 2003-01-2625. *34st International Conferenceon Environmental Systems. Orlando, July 2003.*
23. Rifert V. G., Barabash P. A., Solomakha A. S., Usenko V., Sereda V. V., Petrenko V. G. (2018). Hydrodynamics and heat transfer in centrifugal film evaporator. *Bulgarian Chemical Communications, 50, Special Issue K, 49 - 57.*
24. Rifert V. G., Solomakha A. S., Barabash P. A., Usenko V., Sereda V. V. (2020). Justification of the method for calculating heat transfer in film evaporators with a rotating surface. *Bulgarian Chemical Communications, 52, Special Issue F, 95-102. DOI: 10.34049/bcc.52.F.0016*
25. Solomakha A. S., Rifert V. G., Barabash P. A., Petrenko V., Yaroshevych M. (2021). Centrifugal flash distiller for life support system. *72 International Astronautical Congress (IAC), Dubai, United Arab Emirates, 25-29 October 2021.* IAC-21- A1, IP,6, x 66795. 7 pages.
26. Butuzov A. I. and Rifert V. G. (1973). Heat transfer in evaporation of liquid from a film on a rotating disc. *Heat Transfer Soviet Research*, 5, 1.

Submitted 18.01.2023

Анатичук Л. І., *акад. НАН України* [1,2]
Ріферт В. Г., *док. техн. наук* [3]
Барабаш П. О., *канд. техн. наук* [3]
Десятерик Р. В., *канд. техн. наук* [3]
Соломаха А. С., *канд. техн. наук* [3]
Розвер Ю. Ю., *науковий співробітник*[1]
Петренко В. Г., *канд. техн. наук* [3]

[1] Інститут термоелектрики НАН та МОН України,
вул. Науки, 1, Чернівці, 58029, Україна,
e-mail: anatych@gmail.com, y.rozver@chnu.edu.ua
[2] Чернівецький національний університет імені Юрія Федьковича,
вул. Коцюбинського 2, Чернівці, 58012, Україна, *e-mail: anatych@gmail.com*
[3] НТУ «КПІ» ім. І.Сікорського, вул. Політехнічна, 6, Київ, 03056, Україна,
e-mail: vgrifert@ukr.net, barabash_tef@ukr.net, drv_td@ukr.net, as_solomaha@ukr.net, petrko@ukr.net

ЕКСПЛУАТАЦІЙНІ ВИПРОБУВАННЯ ТЕРМОЕЛЕКТРИЧНОГО ТЕПЛОВОГО НАСОСУ ДЛЯ ВІДЦЕНТРОВОЇ ДИСТИЛЯЦІЇ СТІЧНИХ ВОД КОСМІЧНОЇ СИСТЕМИ ЖИТТЄЗАБЕЗПЕЧЕННЯ

У статті описано результати випробувань системи багатоступінчастої відцентрової вакуумної дистиляції (CMED) з термоелектричним тепловим насосом (THP). В роботі

наведено результати досліджень з вивчення основних характеристик процесу при концентруванні води та урини в разі використання дистиляторів трьох- і п'ятиступінчасної конструкції. Особливу увагу приділено вивченню впливу параметрів процесу на зміну коефіцієнта ефективності термоелектричного теплового насосу. Бібл. 26, рис. 4, табл.3.

Ключові слова: тепловий насос, дистилятор.

References

1. Rifert, V. G., Anatychuk, L. I., Barabash, P. O., Solomakha A. S., Strykun A. P., Sereda, V. V., Prybyla,A. V. (2019). Evolution of centrifugal distillation system with a thermoelectric heat pump for space missions. *J. Thermoelectricity*, 3, 5 – 19.
2. Rifert V. G., Anatychuk L. I., Barabash P. O., Usenko V. I., Solomakha A. S., Petrenko V. G., Prybyla A. V., Sereda V. V. (2019). Comparative analysis of thermal distillation methods with heat pumps for long space flights. *J. Thermoelectricity*, 4, 5 – 18.
3. Rifert, V., Solomakha, A., Barabash, P. et al. (2022). Centrifugal multiple effect distiller for water recovery for space applications. *CEAS Space Journal*. https://doi.org/10.1007/s12567-022-00480-x
4. Roebelen, G., Jr., Dehner, G., Winkler, H. (1984). Thermoelectric integrated membrane evaporation water recovery technology. *SAE 93,559–570*. https:// doi.org/ 10. 4271/ 820849
5. Dehner, G. F., Reysa, R. P. (1985). Thermoelectric integration membrane evaporation subsystem water recovery technology update. In: *15 Intersociety Conference on environmental systems. Paper 851348.* https:// doi.org/ 10. 4271/ 851348
6. Dehner, G. F., Price, D. F. (1987). Thermoelectric integration membrane evaporation subsystem testing. *SAE Paper 871446*. https://doi.org/10.4271/871446
7. Thibaud-Erkey C., Fort J., Scull T., Edeen M. (2002). Performance testing of a new membrane evaporator for the thermoelectric integrated membrane evaporator system (TIMES) water processor. In:*32nd International Conference on Environmental Systems. SAE 2002-01-2525.* https:// doi.org/ 10. 4271/ 2002- 01- 2525
8. Development of a prototype TIMES wastewater recovery subsystem. Roerelen G. J., Denher G. F. PREPARED UNDER CONTRACT NO. NAS 9-15471, 1982 and 1984
9. Rifert Vladimir G., Barabash Petr A., Usenko Vladimir, Solomakha Andrii S., Anatychuk Lukyan I., Prybyla A.V. Improvement the cascade distillation system for long-term space flights. *68th International Astronautical Congress (IAC), Adelaide, Australia, 25-29 September 2017*. IAC-17-A1.IP.25.
10. *Vapor compression distillation module* (Contracts NAS9-13714 & NAS9-14234), Prepared by P. P.Nuccio, 1975
11. Noble Larry D., Schubert Franz H., Pudoka Rick J., Miernik Janie H. (1990). Phase change water recovery for the space station free domand future exploration missions. *20th lntersociety Conference on Environmental Systems. Williamsburg, Virginia, July 9-12, 1990. SAE Technical Paper 901294.*
12. Wieland P., Hutchens C. and Long D., B. Salyer Final Report on Life Testing of the Vapor Compression Distillation / *Urine Processing Assembly (VCD/UPA) at the Marshall Space Flight Center (1993 to 1997) NASA/TM —1998–208539*
13. Carter L., Williamson J., Brown C.A., Bazley J., Gazda D., Schaezler R., Thomas Frank. (2018). Status of ISS water management and recovery. *48th International Conference on Environmental*

Systems. 8 - 12 July 2018, Albuquerque, NewMexico. ICES-2018-088.

14. Carter L., Williamson J., Brown C.A., Bazley J., Gazda D., Schaezler R., Thomas Frank (2017). Status of ISS water management and recovery. *47th International Conference on Environmental Systems, 17 – 20 July 2017, Charleston, South Carolina*. ICES-2016-036
15. Rifert V. G., Anatychuk L. I., Barabash P. O., Solomakha A. S., Usenko V. I., Petrenko V. G. (2021). Justification of thermal distillation method with a thermoelectric heat pump for long-term space missions. *J. Thermoelectricity*, 1, 5 – 22. http://jt.inst.cv.ua/jt/jt_2021_01_en.pdf
16. Rifert V. G., Anatychuk L. I., Solomakha A. S., Barabash P. O., Petrenko V. G., Snegovskoy O. P. (2021). Influence of thermodynamic characteristics of a thermoelectric heat pump on the performance and energy consumption of a centrifugal distiller. *J. Thermoelectricity*, 2, 5 – http://jt.inst.cv.ua/jt/jt_2021_02_en.pdf
17. Rifert Vladimir G., Anatychuk Lukyan I., Solomakha Andrii S., Barabash Petr A., Usenko Vladimir, Prybyla A.V., Naymark Milena, Petrenko Valerii (20190. Upgrade the centrifugal multiple-effect distiller for deep space missions. *70th International Astronautical Congress (IAC), Washington D.C., United States, 21-25 October 2019.* IAC-19-A1,IP,11,x54316.
18. Solomakha A.S., Anatychuk L.I., Rifert V.G., Barabash P.A., Usenko V., Petrenko V. (2020). Thermal distillation system for deep space missions: rationale for the choice. *71st International Astronautical Congress (IAC) – The Cyber Space Edition, 12-14 October 2020*. IAC-20-A1,VP,15,x61344. 7 pages. https://www.iafastro.org/assets/files/publications/iac-publications/IAC2020-Virtual-FinalProgramme-2020-10-07-FINAL-online-Lowres.pdf
19. Rifert V., Barabash P., Goliad N. (1990). Methods and processes of thermal distillation of water solutions for closed water supply systems. *The 20th Intersociety Conference on Environmental Systems, Williamsburg, July 1990. SAE Paper 901249.*
20. Rifert V., Usenko V., Zolotukhin I., MacKnight A., Lubman A. (1999). Comparison of secondary water processors using distillation for space applications. *SAE Paper 99-70466, 29th International Conferenceon Environmental Systems, Denver, July 1999.*
21. Rifert V., Stricun A., Usenko V. (2000). Study of dynamic and extreme performances of multistage centrifugal distiller with the thermoelectric heat pump. *SAE Technical Papers 2000. 30th International Conferenceon Environmental Systems; Toulouse; France; 10-13 July 2000.*
22. Rifert V. G., Usenko V. I., Zolotukhin I. V., MacKnight A. and Lubman A. (2003). Cascaded distillation technology for water processing in space. SAE Paper 2003-01-2625. *34st International Conferenceon Environmental Systems. Orlando, July 2003.*
23. Rifert V. G., Barabash P. A., Solomakha A. S., Usenko V., Sereda V. V., Petrenko V. G. (2018). Hydrodynamics and heat transfer in centrifugal film evaporator. *Bulgarian Chemical Communications, 50, Special Issue K, 49 - 57.*
24. Rifert V. G., Solomakha A. S., Barabash P. A., Usenko V., Sereda V. V. (2020). Justification of the method for calculating heat transfer in film evaporators with a rotating surface. *Bulgarian Chemical Communications, 52, Special Issue F, 95-102. DOI: 10.34049/bcc.52.F.0016*
25. Solomakha A. S., Rifert V. G., Barabash P. A., Petrenko V., Yaroshevych M. (2021). Centrifugal flash distiller for life support system. *72 International Astronautical Congress (IAC), Dubai, United Arab Emirates, 25-29 October 2021.* IAC-21- A1, IP,6, x 66795. 7 pages.
26. Butuzov A. I. and Rifert V. G. (1973). Heat transfer in evaporation of liquid from a film on a rotating disc. *Heat Transfer Soviet Research*, 5, 1.

Submitted: 18.01.2023


L. I .Anatychuk

L. I. Anatychuk, *acad. National Academy of Sciences of Ukraine*[1,2]
V. V. Lysko, *cand. phys. - math. Sciences*[2]

Institute of Thermoelectricity of the NAS
and MES of Ukraine,
1, Nauky str., Chernivtsi, 58029, Ukraine,
e-mail: anatych@gmail.com
[2]Yu.FedkovychChernivtsiNationalUniversity,
2, Kotsiubynskyistr., Chernivtsi, 58012, Ukraine


V. V. Lysko

ON THE DESIGN OF A TRENCH THERMOELECTRIC SOURCE OF HEAT AND ELECTRICITY

The article presents physical and mathematical models of a trench thermoelectric source of heat and electricity intended for heating the military and powering low-power military equipment, mobile and special communications systems, charging batteries and lighting, providing heat and minimal electrical energy to the civilian population in places where the energy infrastructure has been destroyed, as well as in non-electrified areas outside the combat zone.A computer model has been created for designing the structure of such a heat and electricity source, as well as optimizing the thermoelectric material it is made of for various operating modes.Bibl. 15, Fig.1.
Keywords: thermoelectric source of heat and electricity, physical model, efficiency, cyclic mode.

Introduction

At present, the use of chemical current sources as autonomous low-power sources of electricity remains traditional for powering military equipment. However, their significant disadvantages are self-discharge and low reliability, especially at low ambient temperatures and under conditions of increased mechanical loads. Mobile mini-power plants are practically unsuitable for use in combat areas due to unacceptable mass and dimensional characteristics, the need for fuel, which may not always be available in combat conditions, and most importantly - due to the noise accompanying their operation, they become a significant unmasking factor. In this regard, it is important to search for and create fundamentally new designs of autonomous heat and electricity sources that are as close as possible to military equipment and at the same time suitable for use in combat areas.

In this regard, autonomous thermoelectric power sources operating from the heat of combustion of any fuel are especially promising. They can offer a long service life, have increased reliability and resistance to climatic and shock loads, are universal, silent in operation and easy to use.Scientists and engineers from many countries are actively working on the creation of such sources. Thermoelectric generators with an electric power of 2 - 20 W, intended for charging mobile phones, MP3 players, navigators during travel and hiking trips, have been developed by a number of foreign companies (TES, Power Pot, Biolite) [1 – 5]. Thermoelectric generators have also been developed, the operation of which is based on the use of heat from solid fuel furnaces [6 – 9]. They are mass-produced by a

number of foreign enterprises [8 – 10]. However, all of these thermoelectric generators are expensive, have an exclusively domestic purpose and are not suitable for military needs.

At the same time, the main obstacle for their widespread practical use is a relatively high cost, primarily due to the high cost of the thermoelectric material from which they are made. Therefore, it is important to carry out research aimed at significantly reducing the cost of materials for autonomous thermoelectric sources of electricity and heat, as well as finding optimal designs of such sources, specialized according to the conditions of their use.

Therefore, *the purpose of the work* is to create tools (physical and mathematical models, computer programs) necessary for the design of autonomous thermoelectric generators and optimization of the thermoelectric material they are made of, as close as possible to the reality of their operating conditions.

Physical model

The physical model of the thermoelectric generator (Fig. 1) comprises: heat sources 1 (heated surface), heat exchangers for supply 3 and discharge 8 of the heat flow to/from the thermopile 6, thermal insulation 5, water tank 10, electronic device for stabilizing the output voltage with electric energy accumulator 11. The model also takes into account thermal contact resistances 2, 4, 7 and 9: between the heat source (heated surface) and the hot heat exchanger – K_1; between the hot heat exchanger and the thermopile - K_2; between the thermopile and the cold heat exchanger - K_3; between the cold heat exchanger and the water container - K_4.

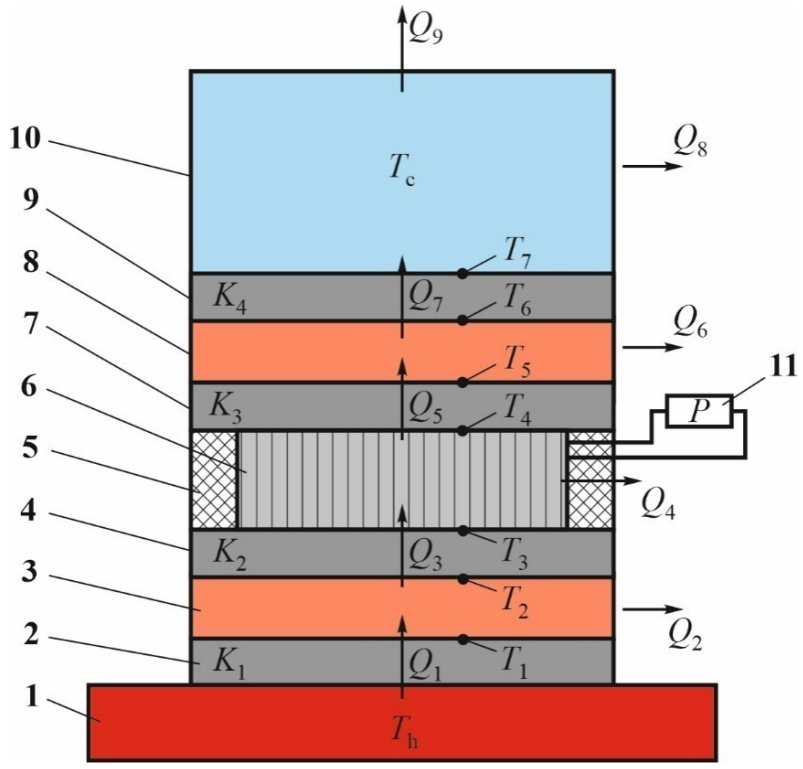

Fig. 1 Physical model of a trench thermoelectric generator:
1 – heat source (heated surface); 2, 4, 7, 9 – thermal contact resistances; 3 – hot heat exchanger;
5 – thermal insulation; 6 – thermopile;8 – cold heat exchanger; 10 –container with water:
11 – electronic device for stabilizing output voltage with an electric energy accumulator

In Fig. 1: Q_1 – is heat entering the hot heat exchanger from the heat source; Q_2 – is heat loss from the lateral surface of the hot heat exchanger to the environment due to radiation and convection; Q_3 – is heat entering the hot side of the thermopile from the hot heat exchanger; Q_4 – is heat loss from the lateral surface of the thermopile; Q_5 – is heat coming from the cold side of the thermopile to the cold heat exchanger; Q_6 – is heat transferred from the lateral surface of the cold heat exchanger to the environment due to radiation and convection; Q_7 – is heat transferred from the cold heat exchanger to the container with water; Q_8 – is heat transferred from the lateral surface of the container with water to the environment due to radiation and convection; Q_9 – is heat transferred from the container with water to the environment due to evaporation; P is electric power of the thermopile.

The thermoelectric generator can have two modes of operation:

1) heating water in the container to boiling temperature and gradually reducing the amount of water due to evaporation;
2) heating water in the container to boiling temperature and replacing it with water at room temperature.

Since it is assumed that the generator is mounted on a heated surface with a constant temperature T_h, heat exchange processes between the real source of fuel combustion and this surface are not considered.

Mathematical and computer descriptions of the model

To calculate the thermoelectric generator according to its physical model (Fig. 1), a system of heat balance equations was used:

$$\begin{cases} Q_1 = Q_2 + Q_3, \\ Q_3 = P + Q_4 + Q_6 + Q_8 + Q_9. \end{cases} \tag{1}$$

The supply of heat from the heated surface to the hot side of the thermopile and the removal of heat from its cold junctions to the cold heat exchanger is carried out due to thermal conductivity and is described by the equations:

$$Q_3 = \frac{\kappa_h S_h}{l_h}\left(T_2 - T_3\right), \tag{2}$$

$$Q_7 = \frac{\kappa_c S_c}{l_c}\left(T_6 - T_7\right), \tag{3}$$

where: κ_h, κ_c – is the thermal conductivity of the material of the hot and cold heat exchangers; l_h, l_c, S_h, S_c – are the thickness and area of the hot and cold heat exchanger.

The thermal power of Q_5 is removed from the cold side of the thermopile by a cold heat exchanger, which is a container with water.

In doing so, different approximate formulae can be used to calculate the heat transfer coefficient during boiling, which are in good agreement with the experimental data [11]. In particular, the following approach to calculating the heat transfer coefficient during boiling is presented in [12]

$$h_{boil} = \frac{q}{\Delta T}, \tag{4}$$

where q is the heat flow density at the solid-liquid interface; ΔT is the temperature head between the surface and the liquid,

$$\Delta T = T_{cm} - T_{нас}\,. \tag{5}$$

It is considered that the heat flow density on the wall:

$$q_c = q_{conv} + q_{vapor}, \tag{6}$$

where q_{conv} takes into account the transfer of heat by convection of a single-phase liquid; q_{vapor} takes into account the transfer of heat by vapour bubbles breaking away from the wall.

The heat flow density corresponding to heat transfer by vapour bubbles is equal to:

$$q_{vapor} = V\rho_n r \frac{N_z}{\Delta F} f\,, \tag{7}$$

where: V is the average volume of the bubble at the moment of separation from the heating surface; ρ_n is vapour density on the saturation line; N_Z is the number of active vaporization centres on the area ΔF; f is the average frequency of separation of vapour bubbles; r is the heat of vaporization.

Assuming that the main amount of heat is transferred due to boiling, and the effect of convection is taken into account by introducing a correction, we can write:

$$q_c = q_{conv} + q_{vapor} = q_{vapor}\varepsilon = V\rho_n r \frac{N_z}{\Delta F} f\varepsilon\,, \tag{8}$$

where ε is the correction for q_{conv}, which takes into account the proportion of heat transferred by convection.

Substituting the value $V = \frac{\pi}{6} d_0^3$ and making some permutations we get:

$$\frac{q_c}{r\rho_n f d_0} = \frac{\pi}{6}\frac{N_z}{\Delta F} d_0^2 \varepsilon \tag{9}$$

Here, the left side of the equation is the ratio of the average rate of vaporization $\frac{q_c}{r\rho_n}$ (this value has the dimension *m/s*) to the average rate of growth of vapour bubbles $d_0 f = w''$.

In general, the dependence for calculating the heat exchange coefficient will have the form [12]:

$$\frac{h_{boil}\delta}{\lambda_p} = 75\left(\frac{q_c}{r\rho_n f d_0}\right)^{0.7}\left(\frac{v_p}{a_p}\right)^{-0.2}, \tag{10}$$

where δ is the characteristic size, in this case the Laplace capillary constant

$$\delta=\sqrt{\frac{\sigma}{g\left(\rho'-\rho''\right)}}\,. \tag{11}$$

The average growth rate of vapour bubbles is determined by the relationship:

$$w^{"}=w_n=d_0 f=0.36\cdot 10^{-3}\,\Pi^{1.4}, \tag{12}$$

Where $\Pi=\frac{P_{cr}}{P}$; defining temperature $t_{def}=t_p=t_{sat}$.

The electric power generated by the thermopile is proportional to Q_3 and the thermopile efficiency η.

The main heat loss:

- from the lateral surface of the hot heat exchanger due to convection and radiation

$$Q_2=h_h A_h\left(\frac{T_2+T_3}{2}-T_0\right)+\varepsilon_h\sigma_{C.-B.}A_h\left(\left(\frac{T_2+T_3}{2}\right)^4-T_0{}^4\right), \tag{13}$$

where: h_h is the coefficient of convection heat exchange between the lateral surface of the hot heat exchanger and the environment; A_h is the area of the lateral surface of the hot heat exchanger; ε_h is the radiation coefficient of the lateral surface of the hot heat exchanger; $\sigma_{S.-B.}$ is the Stefan-Boltzmann constant.

- from the lateral surface of the thermopile due to thermal insulation

$$Q_4=\frac{\kappa_{iз}S_{iз}}{l_{iз}}\left(T_4-T_5\right), \tag{14}$$

where: $\kappa_{iз}$ is the thermal conductivity of the insulating material; $S_{iз}$ is the surface area of the hot heat exchanger not occupied by the thermopile; $l_{iз}$ is the thickness of the thermal insulation layer.

The electric power P generated by a thermopile is proportional to Q_3 and the efficiency of the thermopile η and is determined primarily by the operating temperatures of the thermopile T_4 and T_5, as well as the properties of the thermoelectric material it is made of.

The solution of the system of equations (1) with regard to formulae (2) - (15) allows one to determine the main energy and design parameters of a thermoelectric generator for various properties of the thermoelectric material, generator designs and its operating modes.

In this case, the Comsol Multiphysics software package [13] was used for the computer representation of the mathematical model of the thermopile. To do this, it is necessary to present the equation in the following form.

To describe the flows of heat and electricity, we will use the laws of conservation of energy

$$div\vec{E}=0 \tag{15}$$

and electric charge

$$div\vec{j} = 0, \tag{16}$$

where

$$\vec{E} = \vec{q} + U\vec{j}, \tag{17}$$

$$\vec{q} = \kappa\nabla T + \alpha T\vec{j}, \tag{18}$$

$$\vec{j} = -\sigma\nabla U - \sigma\alpha\nabla T. \tag{19}$$

Here $\vec{E}$ – is energy flow density, $\vec{q}$ – is heat flow density, $\vec{j}$ – is electric current density, U – is electric potential, T – is temperature, α, σ, κ – are the Seebeck coefficient, electric conductivity and thermal conductivity.

From equations (17) – (19), one can obtain

$$\vec{E} = -(\kappa + \alpha^2\sigma T + \alpha U\sigma)\nabla T - (\alpha\sigma T + U\sigma)\nabla U. \tag{20}$$

Then the laws of conservation (15), (16) will acquire the form:

$$-\nabla\left[(\kappa + \alpha^2\sigma T + \alpha U\sigma)\nabla T\right] - \nabla\left[(\alpha\sigma T + U\sigma)\nabla U\right] = 0, \tag{21}$$

$$-\nabla(\sigma\alpha\nabla T) - \nabla(\sigma\nabla U) = 0. \tag{22}$$

By solving equations (21) - (22), it is possible to obtain the distribution of physical fields, as well as the value of the efficiency and power of a thermopile, depending on the thermoelectric properties of the thermopile material and the temperature conditions of its operation, obtained by solving the thermal part of the model.

This information is the basis for the creation of specialized thermoelectric modules based on thermoelectric materials optimized for different modes of their operation. The significant change in the cost of thermoelectric generators can be achieved, especially due to the development and use of optimized functional thermoelectric materials, use of flat extruded thermoelectric materials, etc. Indoingso, material optimization is usually done experimentally. For this purpose, samples of different chemical composition and with different impurity concentrations in the expected range of its values are prepared using different methods. The set of thermoelectric materials obtained in this way is subjected to measurements of σ, α, κ in the required temperature ranges.The measurement results provide information used to adjust the initial chemical composition and concentration of impurities and, accordingly, to find their optimal values. The decisive role in this will be played by the accuracy of the measurements and their speed [14, 15].

Conclusions

1. A physical model of a trench thermoelectric generator designed to power low-power military and civilian equipment is presented, as well as a mathematical and computer description of this model.
2. The created computer model allows determining the dynamic and average power of a thermoelectric generator, and designing a generator with specialized thermoelectric modules based on thermoelectric materials optimized for various operating modes.

References

1. Pat. CN216524233U. Thermoelectric water kettle water level detection circuit. Published 13.05.2022.
2. Pat. CN105167597B. A kind of thermo-electric generation hot-water bottle. Published 02.01.2018.
3. Pat. CN209391675U. A kind of heating vessel. Published. 17.09.2019.
4. Pat. CN208806757U. Thermo-electric generation wild cooker. Published. 30.04.2019.
5. Pat. GB2605345A. Cooking vessel. Published 28.09.2022.
6. Montecucco A. & Siviter J. & Knox A. R. (2017). Combined heat and power system for stoves with thermoelectric generators.*Applied Energy*, Elsevier, 185(P2), 1336-1342. DOI: 10.1016/j.apenergy.2015.10.132.
7. Żołądek Maciej, Papis Karolina, Kuś Jakub, Zając Michal, Figaj Rafal and Rudykh Kyrylo (2020). The use of thermoelectric generators with home stoves. *E3S Web Conf*., 173 (2020) 03005. DOI: https://doi.org/10.1051/e3sconf/202017303005.
8. Wood stove thermoelectric generator rabbit ears. *Retrieved from:* https://thermoelectric-generator.com/product/wood-stove-thermoelectric-generator-rabbit-ears/.
9. 45-watt teg generator for wood stoves with air-cooling. *Retrieved from:*https://www.tegmart.com/thermoelectric-generators/wood-stove-air-cooled-45w-teg.
10. Thermoelectric power generator for fireplace heater. *Retrieved from:*http://www.thermonamic.com/pro_view.asp?id=828.
11. Shevel E. V., Vorobyov M. V. (2021). *Teploobmin pry kypinni: navchalnyi posibnyk [Heat transfer during boiling: a tutorial]*.Kyiv: Igor Sikorsky KPI.
12. Tolubinskii V. I. (1980). *Teploobmen pri kipenii[Heattransferduringboiling]*. Kyiv: Naukova dumka [in Russian]
13. COMSOL Multiphysics User's Guide. COMSOLAB, 2010. – 804 p.
14. Anatychuk L. I., Lysko V. V. (2019). *Thermoelectricity: Vol. 5. Metrology of Thermoelectric Materials.* Chernivtsi: Bukrek.
15. Anatychuk L. I., Lysko V. V. (2014). On improvement of the accuracy and speed in the process of measuring characteristics of thermoelectric materials. *Journal of Electronic Materials*, 43(10), 3863-3869.

Submitted: 13.02.2023

Анатичук Л. І., *акад. НАН України* [1,2]
Лисько В. В., *канд. фіз.-мат. наук* [1,2]

[1] Інститут термоелектрики НАН та МОН України,
вул. Науки, 1, Чернівці, 58029, Україна;
[2] Чернівецький національний університет імені Юрія Федьковича,
вул. Коцюбинського 2, Чернівці, 58012, Україна, *e-mail: anatych@gmail.com*

ПРО ПРОЄКТУВАННЯ ОКОПНОГО ТЕРМОЕЛЕКТРИЧНОГО ДЖЕРЕЛА ТЕПЛА ТА ЕЛЕКТРИКИ

Наведено фізичну та математичну моделі окопного термоелектричного джерела тепла та електрики, призначеного для обігріву військових та живлення малопотужної військової апаратури, систем мобільного та спеціального зв'язку, зарядки акумуляторів та освітлення, забезпечення теплом та мінімальною електричною енергією цивільного населення в місцях, де зруйнована енергетична інфраструктура, а також у неелектрифікованих районах поза зоною бойових дій. Створено комп'ютерну модель для проєктування конструкції такого джерела тепла та електрики, а також оптимізації термоелектричного матеріалу, з якого його виготовлено, для різних режимів експлуатації. Бібл. 15, рис. 1.

Ключові слова: термоелектричне джерело тепла та електрики, фізична модель, ефективність, циклічний режим.

References

1. Pat. CN216524233U. Thermoelectric water kettle water level detection circuit. Published 13.05.2022.
2. Pat. CN105167597B. A kind of thermo-electric generation hot-water bottle. Published 02.01.2018.
3. Pat. CN209391675U. A kind of heating vessel. Published. 17.09.2019.
4. Pat. CN208806757U. Thermo-electric generation wild cooker. Published. 30.04.2019.
5. Pat. GB2605345A. Cooking vessel. Published 28.09.2022.
6. Montecucco A. & Siviter J. & Knox A.R. (2017). Combined heat and power system for stoves with thermoelectric generators. *Applied Energy*, Elsevier, 185(P2), 1336-1342. DOI: 10.1016/j.apenergy.2015.10.132.
7. Żołądek Maciej, Papis Karolina, Kuś Jakub, Zając Michal, Figaj Rafal and Rudykh Kyrylo (2020). The use of thermoelectric generators with home stoves. *E3S Web Conf*., 173 (2020) 03005. DOI: https://doi.org/10.1051/e3sconf/202017303005.
8. Wood stove thermoelectric generator rabbit ears. *Retrieved from:* https://thermoelectric-generator.com/product/wood-stove-thermoelectric-generator-rabbit-ears/.
9. 45-watt teg generator for wood stoves with air-cooling. *Retrieved from:* https://www.tegmart.com/thermoelectric-generators/wood-stove-air-cooled-45w-teg.
10. Thermoelectric power generator for fireplace heater. *Retrieved from:* http://www.thermonamic.com/pro_view.asp?id=828.
11. Shevel E. V., Vorobyov M. V. (2021). *Teploobmin pry kypinni: navchalnyi posibnyk [Heat transfer during boiling: a tutorial]*. Kyiv: Igor Sikorsky KPI.
12. Tolubinskii V. I. (1980). *Teploobmen pri kipenii[Heat transfer during boiling]*. Kyiv: Naukova dumka
13. COMSOL Multiphysics User's Guide. COMSOLAB, 2010. – 804 p.
14. Anatychuk L. I., Lysko V. V. (2019). *Thermoelectricity: Vol. 5. Metrology of Thermoelectric Materials.* Chernivtsi: Bukrek.
15. Anatychuk L. I., Lysko V. V. (2014). On improvement of the accuracy and speed in the process of measuring characteristics of thermoelectric materials. *Journal of Electronic Materials*, 43(10), 3863-3869.

Subminitted: 13.02.2023.

ARTICLE SUBMISSION GUIDELINES

For publication in a specialized journal, scientific works are accepted that have never been printed before. The article should be written on an actual topic, contain the results of an in-depth scientific study, the novelty and justification of scientific conclusions for the purpose of the article (the task in view).

The materials published in the journal are subject to internal and external review which is carried out by members of the editorial board and international editorial board of the journal or experts of the relevant field. Reviewing is done on the basis of confidentiality. In the event of a negative review or substantial remarks, the article may be rejected or returned to the author(s) for revision. In the case when the author(s) disagrees with the opinion of the reviewer, an additional independent review may be done by the editorial board. After the author makes changes in accordance with the comments of the reviewer, the article is signed to print.

The editorial board has the right to refuse to publish manuscripts containing previously published data, as well as materials that do not fit the profile of the journal or materials of research pursued in violation of ethical norms (for instance, conflicts between authors or between authors and organization, plagiarism, etc.). The editorial board of the journal reserves the right to edit and reduce the manuscripts without violating the author's content. Rejected manuscripts are not returned to the authors.

Submission of manuscript to the journal

The manuscript is submitted to the editorial office of the journal in paper form in duplicate and in electronic form on an electronic medium (disc, memory stick). The electronic version of the article shall fully correspond to the paper version. The manuscript must be signed by all co-authors or a responsible representative.

In some cases it is allowed to send an article by e-mail instead of an electronic medium (disc, memory stick).

English-speaking authors submit their manuscripts in English. Russian-speaking and Ukrainian-speaking authors submit their manuscripts in English and in Russian or Ukrainian, respectively. Page format is A4. The number of pages shall not exceed 15 (together with References and extended abstracts). By agreement with the editorial board, the number of pages can be increased.

To the manuscript is added:

1. Official recommendation letter, signed by the head of the institution where the work was carried out.

2. License agreement on the transfer of copyright (the form of the agreement can be obtained from the editorial office of the journal or downloaded from the journal website – Dohovir.pdf). The license agreement comes into force after the acceptance of the article for publication. Signing of the license agreement by the author(s) means that they are acquainted and agree with the terms of the agreement.

3. Information about each of the authors – full name, position, place of work, academic title, academic degree, contact information (phone number, e-mail address), ORCID code (if available). Information about the authors is submitted as follows:

authors from Ukraine - in three languages, namely Ukrainian, Russian and English;

authors from the CIS countries - in two languages, namely Russian and English;

authors from foreign countries – in English.

4. Medium with the text of the article, figures, tables, information about the authors in electronic form.

5. Colored photo of the author(s). Black-and-white photos are not accepted by the editorial staff. With the number of authors more than two, their photos are not shown.

Requirements for article design

The article should be structured according to the following sections:

- *Introduction*. Contains the problem statement, relevance of the chosen topic, analysis of recent research and publications, purpose and objectives.
- *Presentation of the main research material* and the results obtained.
- *Conclusions* summing up the work and the prospects for further research in this direction.
- *References*.

The first page of the article contains information:

1) in the upper left corner – UDC identifier (for authors from Ukraine and the CIS countries);

2) surname(s) and initials, academic degree and scientific title of the author(s);

3) the name of the institution where the author(s) work, the postal address, telephone number, e-mail address of the author(s);

4) article title;

5) abstract to the article – not more than 1 800 characters. The abstract should reflect the consistent logic of describing the results and describe the main objectives of the study, summarize the most significant results;

6) key words – not more than 8 words.

The text of the article is printed in Times New Roman, font size 11 pt, line spacing 1.2 on A4 size paper, justified alignment. There should be no hyphenation in the article.

Page setup: "mirror margins" – top margin – 2.5 cm, bottom margin – 2.0 cm, inside – 2.0 cm, outside – 3.0 cm, from the edge to page header and page footer – 1.27 cm.

Graphic materials, pictures shall be submitted in color or, as an exception, black and white, in .opj or .cdr formats, .jpg or .tif formats being also permissible. According to author's choice, the tables and partially the text can be also in color.

Figures are printed on separate pages. The text in the figures must be in the font size 10 pt. On the charts, the units of measure are separated by commas. Figures are numbered in the order of their arrangement in the text, parts of the figures are numbered with letters – a, b, .. On the back of the figure, the title of the article, the author (authors) and the figure number are written in pencil. Scanned images and graphs are not allowed to be inserted.

Tables are provided on separate pages and must be executed using the MSWord table editor. Using pseudo-graph characters to design tables is inadmissible.

Formulae shall be typed in Equation or MatType formula editors. Articles with formulae written by hand are not accepted for printing. It is necessary to give definitions of quantities that are first used in the text, and then use the appropriate term.

Captions to figures and tables are printed in the manuscript after the references.

Reference list shall appear at the end of the article. References are numbered consecutively in the order in which they are quoted in the text of the article. References to unpublished and unfinished works are inadmissible.

Attention! In connection with the inclusion of the journal in the international bibliographic abstract database, the reference list should consist of two blocks: CITED LITERATURE and

REFERENCES (this requirement also applies to English articles):

CITED LITERATURE – sources in the original language, executed in accordance with the Ukrainian standard of bibliographic description DSTU 8302:2015. With the aid of VAK.in.ua (http://vak.in.ua) you can automatically, quickly and easily execute your "Cited literature" list in conformity with the requirements of State Certification Commission of Ukraine and prepare references to scientific sources in Ukraine in understandable and unified manner. This portal facilitates the processing of scientific sources when writing your publications, dissertations and other scientific papers.

REFERENCES – the same cited literature list transliterated in Roman alphabet (recommendations according to international bibliographic standard APA-2010, guidelines for drawing up a transliterated reference list "References" are on the site http//www.dse.org.ua, section for authors).

To speed up the publication of the article, please adhere to the following rules:

- in the upper left corner of the first page of the article – the UDC identifier;
- family name and initials of the author(s);
- academic degree, scientific title;

begin a new line, Times New Roman font, size 12 pt, line spacing 1.2, center alignment;

- name of organization, address (street, city, zip code, country), e-mail of the author(s);

begin a new line 1 cm below the name and initials of the author(s), Times New Roman font, size 11 pt, line spacing 1.2, center alignment;

- the title of the article is arranged 1 cm below the name of organization, in capital letters, semi-bold, font Times New Roman, size 12 pt, line spacing 1.2, center alignment. The title of the article shall be concrete and possibly concise;
- the abstract is arranged 1 cm below the title of the article, font Times New Roman, size 10 pt, in italics, line spacing 1.2, justified alignment in Ukrainian or Russian (for Ukrainian-speaking and Russian-speaking authors, respectively);
- key words are arranged below the abstract, font Times New Roman, size 10 pt, line spacing 1.2, justified alignment. The language of the key words corresponds to that of the abstract. Heading "Key words" - font Times New Roman, size 10 pt, semi-bold;
- the main text of the article is arranged 1 cm below the abstract, indent 1 cm, font Times New Roman, size 11 pt, line space spacing 1.2, justified alignment;
- formulae are typed in formula editor, fonts Symbol, Times New Roman. Font size is "normal" – 12 pt, "large index" – 7 pt, "small index" – 5 pt, "large symbol" – 18 pt, "small symbol" – 12 pt. The formula is arranged in the text, center aligned and shall not occupy more than 5/6 of the line width, formulae are numbered in parentheses on the right;
- dimensions of all quantities used in the article are represented in the International System of Units (SI) with the explication of the symbols employed;
- figures are arranged in the text. The figures and pictures shall be clear and contrast; the plot axes – parallel to sheet edges, thus eliminating possible displacement of angles in scaling; figures are submitted in color, black-and-white figures are not accepted by the editorial staff of the journal;
- tables are arranged in the text. The width of the table shall be 1 cm less than the line width.

Above the table its ordinary number is indicated, right alignment. Continuous table numbering throughout the text. The title of the table is arranged below its number, center alignment;

- references should appear at the end of the article. References within the text should be enclosed in square brackets behind the text. References should be numbered in order of first appearance in the text. Examples of various reference types are given below.

Examples of LITERATURE CITED

Journal articles

Anatychuk L.I., Mykhailovsky V.Ya., Maksymuk M.V., Andrusiak I.S. Experimental research on thermoelectric automobile starting pre-heater operated with diesel fuel. *J.Thermoelectricity*. 2016. №4. P.84–94.

Books

Anatychuk L.I. *Thermoelements and thermoelectric devices. Handbook.* Kyiv, Naukova dumka, 1979. 768 p.

Patents

Patent of Ukraine № 85293. Anatychuk L.I., Luste O.J., Nitsovych O.V. Thermoelement.

Conference proceedings

Lysko V.V. *State of the art and expected progress in metrology of thermoelectric materials.* Proceedings of the XVII International Forum on Thermoelectricity (May 14-18, 2017, Belfast). Chernivtsi, 2017. 64 p.

Authors' abstracts

Kobylianskyi R.R. *Thermoelectric devices for treatment of skin diseases*: extended abstract of candidate's thesis. Chernivtsi, 2011. 20 p.

Examples of REFERENCES

Journal articles

Gorskiy P.V. (2015). Ob usloviakh vysokoi dobrotnosti i metodikakh poiska perspektivnykh sverhreshetochnykh termoelektricheskikh materialov [On the conditions of high figure of merit and methods of search for promising superlattice thermoelectric materials]. *Termoelektrichestvo - J.Thermoelectricity,* 3, 5 – 14 [in Russian].

Books

Anatychuk L.I. (2003). *Thermoelectricity. Vol.2. Thermoelectric power converters*. Kyiv, Chernivtsi: Institute of Thermoelectricity.

Patents

Patent of Ukraine № 85293. Anatychuk L. I., Luste O.Ya., Nitsovych O.V. Thermoelements [In Ukrainian].

Conference proceedings

Rifert V.G. Intensification of heat exchange at condensation and evaporation of liquid in 5 flowing-down films. In: *Proc. of the 9th International Conference Heat Transfer.* May 20-25, 1990, Israel.

Authors'abstracts

Mashukov A.O. *Efficiency hospital state of rehabilitation of patients with color carcer.* PhD (Med.) Odesa, 2011 [In Ukrainian].